

# Advanced Healthcare Materials

## Mechanoresponse of curved epithelial monolayers lining bowl-shaped 3D microwells

--Manuscript Draft--

<b>Manuscript Number:</b>	adh.m.202203377
<b>Article Type:</b>	Research Article
<b>Corresponding Author:</b>	Sylvain Gabriele Universite de Mons Mons, BELGIUM
<b>Corresponding Author E-Mail:</b>	sylvain.gabriele@umons.ac.be
<b>Order of Authors (with Contributor Roles):</b>	Sylvain Gabriele (Conceptualization: Lead; Data curation: Equal; Formal analysis: Equal; Funding acquisition: Lead; Methodology: Equal; Supervision: Lead; Writing – original draft: Lead; Writing – review & editing: Lead) Marine Luciano (Data curation: Equal; Formal analysis: Equal; Methodology: Equal; Writing – original draft: Equal; Writing – review & editing: Equal) Marie Versaevel (Data curation: Equal; Formal analysis: Equal; Methodology: Equal; Writing – original draft: Equal; Writing – review & editing: Equal) Yohalie Kalukula (Data curation: Supporting; Formal analysis: Supporting; Methodology: Supporting; Writing – original draft: Supporting; Writing – review & editing: Supporting)
<b>Keywords:</b>	hydrogels, microwells, lobular structures, curved geometry, tissue engineering
<b>Section/Category:</b>	
<b>Abstract:</b>	<p>The optimal functioning of many organs relies on the curved architecture of their epithelial tissues. However, the mechanoresponse of epithelia to changes in curvature remains misunderstood. Here, we designed bowl-shaped microwells in hydrogels via photopolymerization to faithfully replicate the shape and dimensions of lobular structures. Leveraging these hydrogel-based microwells, we engineered curved epithelial monolayers and investigated how in-plane and Gaussian curvatures at the microwell entrance influence epithelial behavior. Cells and nuclei around the microwell edge displayed a more pronounced centripetal orientation as the in-plane curvature decreases, and enhanced cell straightness and speed. Moreover, cells reorganized their actin cytoskeleton by forming a supracellular actin cable at the microwell edge, with its size becoming more pronounced as the in-plane curvature decreased. The Gaussian curvature at the microwell entrance enhanced the maturation of the supracellular actin cable architecture and led to a vertical orientation of nuclei towards the bottom of the microwell. Increasing Gaussian curvature resulted in flattened and elongated nuclear morphologies characterized by highly compacted chromatin states. Our approach provides a better understanding of the mechanoresponse of curved epithelial monolayers curvatures lining lobular structures. Additionally, bowl-shaped microwells offer a powerful platform to study curvature-dependent mechanotransduction pathways in anatomically relevant 3D structures.</p>
<b>Suggested Reviewers:</b>	Paul Janmey University of Pennsylvania School of Engineering and Applied Science janmey@mail.med.upenn.edu Kevin Kit Parker Harvard University DEAS: Harvard University John A Paulson School of Engineering and Applied Sciences kkparker@g.harvard.edu Aurélien Roux University of Geneva: Universite de Geneve Aurelien.Roux@unige.ch Caterina Tomba Lyon 1 University: Universite Claude Bernard Lyon 1 caterina.tomba@univ-lyon1.fr

	<p>Olivier Théodoly Aix-Marseille I University: Aix-Marseille Université olivier.theodoly@inserm.fr</p>
	<p>Martial Balland Grenoble I University: Université Grenoble Alpes martial.balland@univ-grenoble-alpes.fr</p>
<b>Opposed Reviewers:</b>	<p>Denis Wirtz, PhD Professor, Johns Hopkins University</p> <p>competitive interests</p>
<b>Author Comments:</b>	<p>This manuscript is a direct transfer from Advanced Science (Research Article, No. advs.202205697) handled by Alanna Gannon</p>
<b>Additional Information:</b>	
<b>Question</b>	<b>Response</b>
<p>Please submit a plain text version of your cover letter here.</p>	<p>Dear Alanna,</p> <p>We thank you for sending us the reviewers' comments on our manuscript advs.202205697 and to consider it further for publication in Advanced Healthcare Materials. We are pleased to submit our revised manuscript "Mechanoresponse of curved epithelial monolayers lining bowl-shaped 3D microwells" for consideration as a Research Article in Advanced Healthcare Materials.</p> <p>As you suggested in your editorial decision, we have thoroughly revised our manuscript that presents now a deeper investigation of how changes of in-plane and Gaussian curvatures can influence the cytoskeletal architecture of epithelial monolayers, and their subsequent effects on nuclear morphology and chromatin compaction. We carefully addressed all technical concerns of the Reviewers and our revision provides an extensive improvement of our manuscript by addressing all last reviewer's comments with additional experiments.</p> <p>All referee comments are addressed in our point-by-point response and we have summarized herein in a non-exhaustive list the main modifications in the revised manuscript:</p> <ul style="list-style-type: none"> <li>- Title, abstract and structure of the manuscript: The title has been changed to "Mechanoresponse of curved epithelial monolayers lining bowl-shaped 3D microwells" and the abstract has been rewritten to better highlight the novelty of our work. We now better introduce the concept of curvature and the paper has been focused on two main zones (flat and Gaussian curvature zones) around the entrance of bowl-shaped 3D microwells. We hope that these changes will improve the fluidity and readability of our manuscript for a wide audience.</li> <li>- Clinical relevance: We provide detailed examples of the different curvatures found in anatomic lobular structures to support the clinical relevance of our new platform. We quantified the Gaussian curvatures at the entrance of bowl-shaped microwells of with radii of 25 <math>\mu\text{m}</math>, 30 <math>\mu\text{m}</math>, 65 <math>\mu\text{m}</math> and 100 <math>\mu\text{m}</math>. Importantly, we demonstrated a strong correspondence between this range of Gaussian curvatures and the typical values of Gaussian curvature observed in anatomic lobular structures within the lung, kidney, breast, and pancreas. Our findings underscore therefore the clinical relevance of utilizing bowl-shaped microwells to investigate the mechanoresponse of curved epithelial monolayers that line lobular structures.</li> </ul>

- Cellular density and division rate: We performed new experiments to determine the cellular density and the division rate at the flat zone around and at the Gaussian curvature zones of microwells. We now provide more details about the methodology.

- Targeted approaches: We followed the reviewer's advice to strengthen our manuscript by providing new experiments that change one variable (e.g. in plane curvature) without affecting all other variables. To this aim, we developed two-dimensional (2D) adhesive micropatterns of similar diameters and consequently in-plane curvature. By using 2D circular adhesive and non-adhesive micropatterns, we imposed similar in-plane curvatures to epithelial monolayers than those observed in 3D microwells. By using this strategy, we aimed to decouple the individual role of in-plane and Gaussian curvatures in the formation of supracellular actin cables by quantifying the amount of actin signal in a supracellular actin cables and their normalized length.

- Chromatin accessibility: In the previous version of our manuscript, we investigated whether nuclear elongations observed at the Gaussian zone of the microwell entrance could lead to differences in chromatin state by using quantitative procedures based on DAPI staining and 3D confocal imaging at high magnifications. We determined the average spatial density of chromatin, which is a reliable indicator of chromatin condensation, and showed that elongated nuclei localized at the maximal Gaussian curvature zone exhibited higher levels of fluorescence intensity. To go one step further in assessing chromatin accessibility, we performed new experiments to characterize the histone H3 acetylation at lysine 9 (H3K9ac) and determine the level of euchromatin histone marks, which correspond to the loosely packed chromatin domain that is transcriptionally accessible.

- Technical comments: We realized that our methodology was not sufficiently detailed in the previous version of the manuscript, giving rise to legitimate concerns on the part of the reviewers. For instance, imaging cytoskeletal components and nuclei in curved epithelial monolayers with conventional confocal microscopy may introduce certain artifacts that can affect the interpretation of our results. This aspect is now better considered in our work by providing clarifications on the method and more details about our methodology in the revised manuscript.

This revised version of our paper makes significant conceptual advances compared to previous works on the role of curvature changes on epithelial tissues. By designing bowl-shaped microwells in hydrogels via photopolymerization, we faithfully replicated the shape and dimensions of lobular structures. Leveraging these hydrogel-based microwells, we engineered curved epithelial monolayers and investigated how in-plane and Gaussian curvatures at the microwell entrance influence epithelial behavior. We show for the first time in confluent epithelial monolayers that local curvature changes can lead to a significant reorganization of the actin cytoskeleton by forming a supracellular actin cable at the microwell edge. We show that the size of the actin ring becomes more pronounced as the in-plane curvature decreased. In addition, we demonstrate that the Gaussian curvature at the microwell entrance can enhance the maturation of the supracellular actin cable architecture and led to a vertical orientation of nuclei towards the bottom of the microwell. Interestingly, our findings show that increasing Gaussian curvature resulted in flattened and elongated nuclear morphologies characterized by highly compacted chromatin states.

We provide a better understanding of the mechanoresponse of curved epithelial monolayers curvatures lining lobular structures. Additionally, bowl-shaped microwells

	<p>offer a powerful platform to study curvature-dependent mechanotransduction pathways in anatomically relevant 3D structures. We believe therefore that this work represents the kind of scientific advancement and novelty in healthcare, biomaterials and cell mechanobiology that typify the research published in Advanced Healthcare Materials and should therefore interest its diverse readership. Furthermore, we believe that Advanced Healthcare Materials is the most appropriate journal to inspire the community of cell mechanobiologists, cell biologists and soft matter physico-chemists.</p> <p>Sincerely yours, Sylvain GABRIELE, PhD On behalf of the authors</p>
Does the research described in this manuscript include animal experiments?	No
Does the research described in this manuscript include human research participants (including for experiments with sensors or wearable technologies) or tissue samples from human subjects (including blood or sweat)?	No
Do you or any of your co-authors have a conflict of interest to declare?	No. The authors declare no conflict of interest.

Mechanobiology & Biomaterials group  
Research Institute for Biosciences  
University of Mons

Sylvain Gabriele, Ph.D.  
Associate Professor

Campus of Sciences and Medicine  
Mendeleiev Building - Office 1-059, 1st floor  
Avenue Maistriau, 15  
B-7000 Mons, Belgium  
Phone: +32/65.37.38.24

sylvain.gabriele@umons.ac.be  
[www.umons.ac.be/cellmechanobiology](http://www.umons.ac.be/cellmechanobiology)

*Advanced Healthcare Materials*  
To the attention of Alanna Gannon, Ph.D.  
Editor at Advanced Healthcare Materials

August 11th, 2023.

Dear Alanna,

We thank you for sending us the reviewers' comments on our manuscript advs.202205697 and to consider it further for publication in *Advanced Healthcare Materials*. We are pleased to submit our revised manuscript "Mechanoresponse of curved epithelial monolayers lining bowl-shaped 3D microwells" for consideration as a Research Article in *Advanced Healthcare Materials*.

As you suggested in your editorial decision, we have thoroughly revised our manuscript that presents now a deeper investigation of how changes of in-plane and Gaussian curvatures can influence the cytoskeletal architecture of epithelial monolayers, and their subsequent effects on nuclear morphology and chromatin compaction. We carefully addressed all technical concerns of the Reviewers and our revision provides an extensive improvement of our manuscript by addressing all last reviewer's comments with additional experiments.

All referee comments are addressed in our point-by-point response and we have summarized herein in a non-exhaustive list the main modifications in the revised manuscript :

- *Title, abstract and structure of the manuscript* : The title has been changed to "Mechanoresponse of curved epithelial monolayers lining bowl-shaped 3D microwells" and the abstract has been rewritten to better highlight the novelty of our work. We now better introduce the concept of curvature and the paper has been focused on two main zones (flat and Gaussian curvature zones) around the entrance of bowl-shaped 3D microwells. We hope that these changes will improve the fluidity and readability of our manuscript for a wide audience.
- *Clinical relevance* : We provide detailed examples of the different curvatures found in anatomic lobular structures to support the clinical relevance of our new platform. We quantified the Gaussian curvatures at the entrance of bowl-shaped microwells of with radii of 25  $\mu\text{m}$ , 30  $\mu\text{m}$ , 65  $\mu\text{m}$  and 100  $\mu\text{m}$ . Importantly, we demonstrated a strong correspondence between this range of Gaussian curvatures and the typical values of Gaussian curvature observed in anatomic lobular structures within the lung, kidney, breast, and pancreas. Our findings underscore therefore the clinical relevance of utilizing bowl-shaped microwells to investigate the mechanoresponse of curved epithelial monolayers that line lobular structures.
- *Cellular density and division rate* : We performed new experiments to determine the cellular density and the division rate at the flat zone around and at the Gaussian curvature zones of microwells. We now provide more details about the methodology.
- *Targeted approaches* : We followed the reviewer's advice to strengthen our manuscript by providing new experiments that change one variable (e.g. in plane curvature) without affecting all other variables. To this aim, we developed two-dimensional (2D) adhesive micropatterns of similar diameters and consequently in-plane curvature. By using 2D circular adhesive and non-adhesive micropatterns, we imposed similar in-plane curvatures to epithelial monolayers than those observed in 3D microwells. By using this strategy, we aimed to decouple the individual role of in-plane and Gaussian curvatures in the formation of supracellular actin cables by quantifying the amount of actin signal in a supracellular actin cables and their normalized length.
- *Chromatin accessibility* : In the previous version of our manuscript, we investigated whether nuclear elongations observed at the Gaussian zone of the microwell entrance could lead to differences in chromatin state by using quantitative procedures based on DAPI staining and 3D confocal imaging at high magnifications. We determined the average spatial density of chromatin, which is a reliable indicator of chromatin condensation, and showed that elongated nuclei localized at the maximal Gaussian curvature zone exhibited higher levels of fluorescence intensity. To go one step further in assessing chromatin accessibility, we performed new experiments to characterize the histone H3 acetylation at lysine 9 (H3K9ac) and determine

the level of euchromatin histone marks, which correspond to the loosely packed chromatin domain that is transcriptionally accessible.

- *Technical comments* : We realized that our methodology was not sufficiently detailed in the previous version of the manuscript, giving rise to legitimate concerns on the part of the reviewers. For instance, imaging cytoskeletal components and nuclei in curved epithelial monolayers with conventional confocal microscopy may introduce certain artifacts that can affect the interpretation of our results. This aspect is now better considered in our work by providing clarifications on the method and more details about our methodology in the revised manuscript.

This revised version of our paper makes significant conceptual advances compared to previous works on the role of curvature changes on epithelial tissues. By designing bowl-shaped microwells in hydrogels via photopolymerization, we faithfully replicated the shape and dimensions of lobular structures. Leveraging these hydrogel-based microwells, we engineered curved epithelial monolayers and investigated how in-plane and Gaussian curvatures at the microwell entrance influence epithelial behavior. We show for the first time in confluent epithelial monolayers that local curvature changes can lead to a significant reorganization of the actin cytoskeleton by forming a supracellular actin cable at the microwell edge. We show that the size of the actin ring becomes more pronounced as the in-plane curvature decreased. In addition, we demonstrate that the Gaussian curvature at the microwell entrance can enhance the maturation of the supracellular actin cable architecture and led to a vertical orientation of nuclei towards the bottom of the microwell. Interestingly, our findings show that increasing Gaussian curvature resulted in flattened and elongated nuclear morphologies characterized by highly compacted chromatin states.

We provide a better understanding of the mechanoresponse of curved epithelial monolayers curvatures lining lobular structures. Additionally, bowl-shaped microwells offer a powerful platform to study curvature-dependent mechanotransduction pathways in anatomically relevant 3D structures. We believe therefore that this work represents the kind of scientific advancement and novelty in healthcare, biomaterials and cell mechanobiology that typify the research published in *NAdvanced Healthcare Materials* and should therefore interest its diverse readership. Furthermore, we believe that *Advanced Healthcare Materials* is the most appropriate journal to inspire the community of cell mechanobiologists, cell biologists and soft matter physico-chemists.

Sincerely yours,  
Sylvain Gabriele, PhD



**Response to the Reviewer's comments for manuscript advs.202205697**

**Mechanoresponse of epithelial monolayers to in-plane and out-of-plane curvatures  
imposed by 3D microwells**

Marine Luciano<sup>#1</sup>, Marie Versaevel<sup>#1</sup>, Yohalie Kalukula<sup>1</sup> and Sylvain Gabriele<sup>1\*</sup>

<sup>1</sup> Mechanobiology & Biomaterials group, Interfaces and Complex Fluids Laboratory, Research Institute for Biosciences, CIRMAP, University of Mons, Place du Parc, 20 B-7000 Mons, Belgium

<sup>#</sup>Contributed equally to this work

<sup>\*</sup>To whom correspondence should be addressed: [sylvain.gabriele@umons.ac.be](mailto:sylvain.gabriele@umons.ac.be)

We thank the reviewers and the editor for their thoughtful comments, overall positive assessment, and constructive suggestions to further improve the manuscript, which we have incorporated into the revised manuscript.

Referees have highlighted that “*the effect of substrate curvature on the organization and structure of epithelial cell layers is an interesting and important topic*” and that “*the current study makes a relevant contribution to the progress in this field*”.

In the following, we individually address each of the Reviewers’ comments/suggestions (in italic). The numbering of the comments (A1, A2, ...) was added by us to aid in cross-referencing our responses. [Modifications of the text in the revised manuscript are in light blue.](#)

---

## Response to Reviewer #1

---

The manuscript by Gabriele and colleagues investigates the influence of in-plane and out-of-plane curvatures on the organization and dynamics of epithelial cells. Authors engineered synthetic 3D micropatterns that geometrically reproduce common organ morphologies using the photopolymerization of hydrogels in an effort to mimic the physical conditions cells encounter in their environment, with the broader goal of establishing an in vitro model for studying the mechanical response of cells to the changes of curvature. The study does contain some interesting observations using a potentially valuable system for the field. However, many such observations are not followed up on, while others are reproducing published findings, leaving the overall scope of the work somewhat superficial and correlative. There are also a handful of deeper concerns with technical aspects of the work and interpretation of results. These are detailed below.

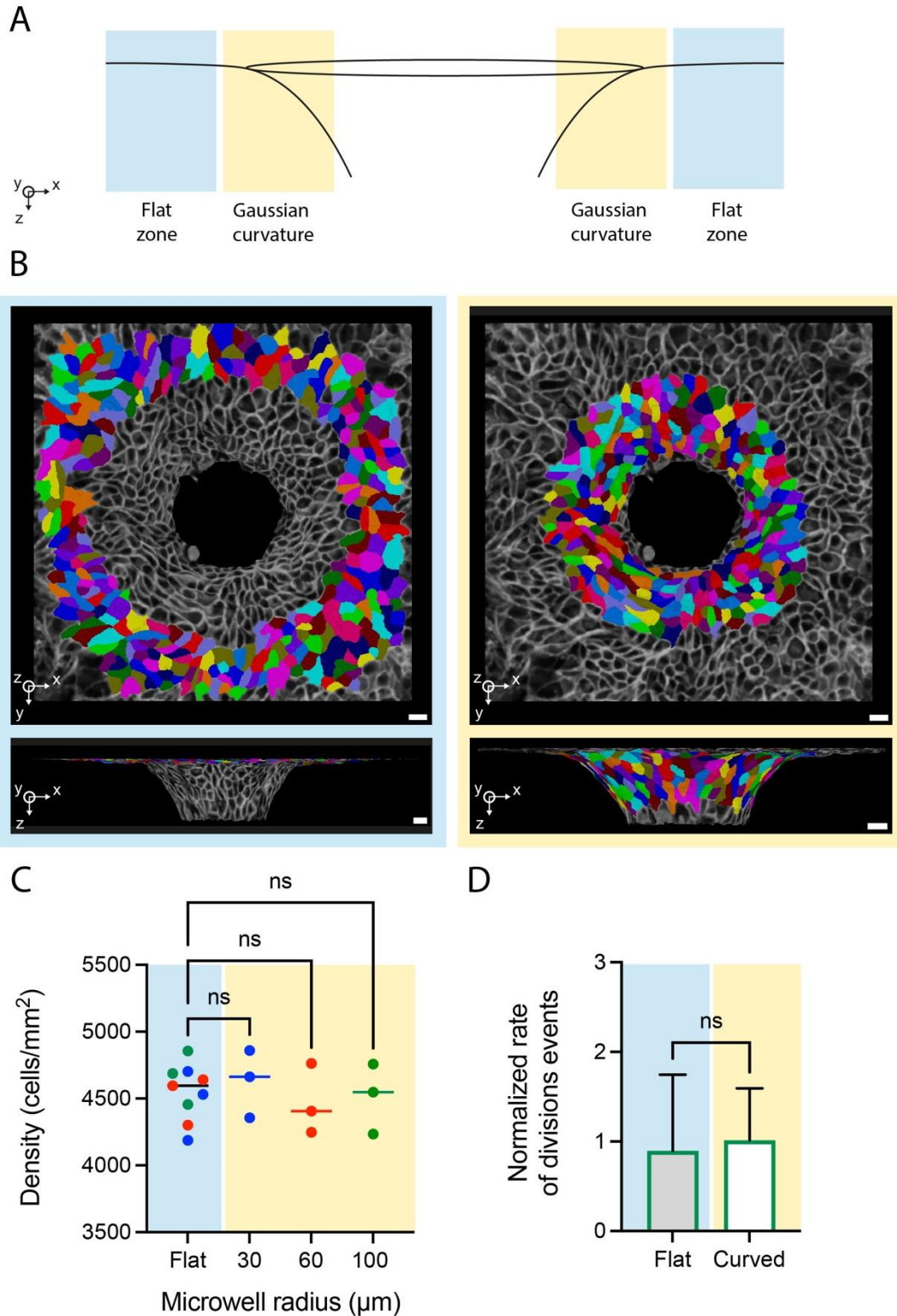
**A1.** Owing to the correlative nature of many key findings (e.g. cell alignment, persistence of movement, out of plane nuclear shape etc), it is not possible to identify the specific geometric or biomechanical cue that cells are responding to. While correlations are observed with varying in plane curvatures, it appears as though in plane and out of plane curvature cannot be orthogonally controlled in this system, making it impossible to determine whether it is in-plane curvature itself, or secondary effects of cell reorganization and pulling forces induced by varied out of plane curvatures that dictate cell behaviors. Similarly, variations in curvature produce variations in surface area of wells, yet the cell seeding density on these materials does not take this into account, such that one could posit an alternate hypothesis that it is not curvature at all, but cell density, that drives observed changes. The only step toward functional investigation comes from blebbistatin experiments that block cell contractility. However, because these drugs are applied broadly to the system, including cells that are not in the wells but on the flat surface surrounding wells, it is not possible to interpret the results as an indication of how curvature influences cell behaviors. More targeted approaches are necessary, such as changing truly one variable (e.g. in plane curvature) while holding all other variables (e.g. cell seeding density, out of plane curvature, well spacing, etc.). Including controls and appropriate characterizations to illustrate this would greatly strengthen the manuscript.



We appreciate the comments by the reviewer, as we do agree this is an important point. Cellular density is a key regulator parameter in epithelial tissues and even if we have taken attention to this point, it was not sufficiently addressed in the previous version of our manuscript.

**1 - Cellular density and division rate:** They were determined on high resolution confocal images of m-cherry cadherin MDCK cells that were acquired at x40 (silicon objective) with an inverted confocal microscope (Nikon TI2 A1R HD25, Japan). We determined area and contour of each individual cell within two different regions of interest (ROI), progressing from the outer edge to the inner regions (**Rebuttal Fig. 1a**). The first zone (in light blue) corresponds to a flat area surrounding the curved edge of the microwells, where the in-plane curvature is determined by the diameter of the well. The second region corresponds to the maximal Gaussian curvature zone (in light yellow) at the microwell entrance. As shown in **Rebuttal Fig. 1b**, individual cells located at either the flat zone (blue box on the left) or the Gaussian curvature zone (yellow box on the right) were segmented on m-cherry cadherin confocal images using the image analysis software package MorphGraphX (<https://doi.org/10.7554/eLife.05864>). The total number of cells in each ROI was normalized by the ROI surface area to obtain a cellular density. To determine the surface area of ROI at the Gaussian curvature zones, we converted 3D  $z$  stack images of MDCK into 2D projections by using a method previously used for tubes (W. Xi et al Nat. Commun. 8, 1517 2017 and A. Glentis et al. Science Advances, 8 2022). Background subtraction was performed to reduce signal-to-noise ratio and  $z$  stack images were then resliced to project the  $xz$  plane for the circular cross section of MDCK tissues. Afterward, a circle was fit to the Gaussian curvature zone and the perimeter obtained was mapped into a line, which was straightened and resliced again to obtain a 2D projection of virtually flattened ROI. Our results indicated that both zones exhibited similar cell density (**Rebuttal Fig. 1c**) and comparable rates of division events (**Rebuttal Fig. 1d**). The **Rebuttal Fig. 1** has been now added as **Supplementary Figure 2** in the revised manuscript. The legend and the method section have been modified accordingly.

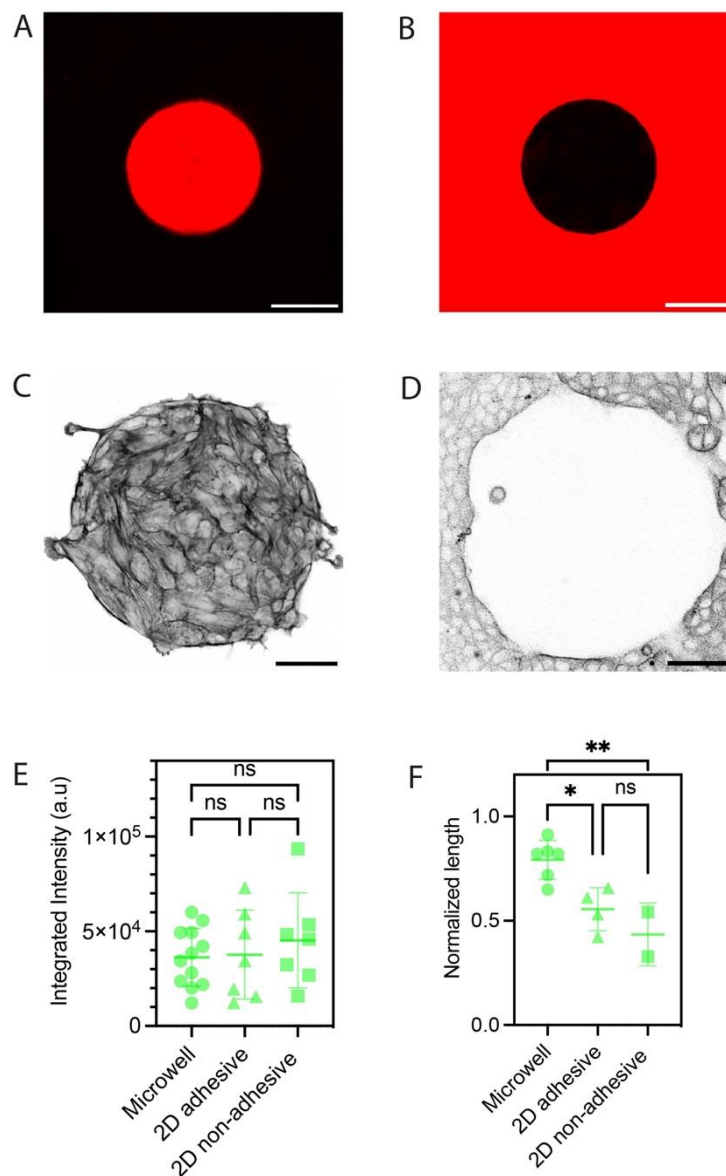
**2 - Targeted approaches:** We appreciate the reviewer's advice to strengthen our manuscript and we now provide new experiments to change one variable (e.g. in plane curvature) without affecting all other variables to determine the role of the Gaussian curvature on the formation of supracellular actin rings. To this aim, we developed two-dimensional (2D) adhesive micropatterns of similar diameters and consequently in-plane curvature. We used 2D circular adhesive (**Rebuttal Fig. 2a**) and non-adhesive (**Rebuttal Fig. 2b**) micropatterns of 100  $\mu\text{m}$  in radius to impose similar in-plane curvatures to epithelial monolayers than those observed in 3D microwells. By using this strategy, we aimed to decouple the individual role of in-plane and Gaussian curvatures in the formation of supracellular actin cables by quantifying the amount of actin signal in a supracellular actin cables and their normalized length. As shown in **Rebuttal Fig. 2c-d**, we observed the formation of a supracellular actin cable on both conditions, which contain a similar amount of actin than observed in 3D microwells (**Rebuttal Fig. 2e**).



**Rebuttal Figure 1 – Cell density and proliferation rate.** (A) Schematic representation of two distinct regions around the entrance of bowl-shaped 3D microwells, progressing from the outer edge to the inner regions. The first zone (in light blue) corresponds to a flat area surrounding the curved edge of the microwells, where the in-plane curvature is determined by the diameter of the well. The second region corresponds to the maximal Gaussian curvature zone (in light yellow) at the microwell entrance. (B) Individual cells located at either the flat zone (blue box

on the left) or the Gaussian curvature zone (yellow box on the right) were segmented on m-cherry cadherin confocal images. Top and bottom rows show normal and side confocal views of both zones in a microwell of 100  $\mu\text{m}$  in radius, respectively. (C) Cellular density in flat (light blue box) and Gaussian curvature (light yellow box) zones for microwell radius of 30  $\mu\text{m}$  (in blue), 65  $\mu\text{m}$  (in red) and 100  $\mu\text{m}$  (in green). (D) Normalized rate of division events in flat (light blue box) and Gaussian curvature (light yellow box) zones of a microwell of 100  $\mu\text{m}$  in radius. n.s. is not significant.

Surprisingly, our findings showed that the length of supracellular actin cables normalized by the total perimeter was significantly larger in 3D microwells than on adhesive and non-adhesive circular patterns (**Rebuttal Fig. 2f**). Altogether, our findings showed that the Gaussian curvature imposed at the microwell entrance by its 3D morphology promotes the maturation of the supracellular actin cable architecture. The **Rebuttal Fig. 2** has been now added as **Supplementary Figure 4 in the revised manuscript**. The legend and the method section have been modified accordingly.



## **Rebuttal Figure 2 – Supracellular actin ring in 2D micropatterned epithelial monolayers.**

2D circular (A) adhesive and (B) non-adhesive fibronectin (in red) micropatterns of 100  $\mu\text{m}$  radius. The scale bars are 100  $\mu\text{m}$ . Representative image of the actin cytoskeleton of MDCK cells grown for 24 hours on 2D circular (C) adhesive and (D) non-adhesive fibronectin micropatterns. The scale bars are 50  $\mu\text{m}$ . (E) Integrated intensity and (F) normalized length of the actin ring in 3D microwell of 100  $\mu\text{m}$  in radius (circles), 2D adhesive circular patterns of 100  $\mu\text{m}$  in radius (triangles) and 2D non-adhesive circular patterns of 100  $\mu\text{m}$  in radius (squares).

**A2.** From the technical standpoint, there are significant concerns that the imaging approach is not sufficient for capturing precise 3-D cell and nuclear morphologies. Out of plane curvature is known to introduce some often dramatic artifacts in imaging via conventional confocal microscopy (Herbert et al BMC Biology 2021, for example). This is not considered here, limiting the strength of several conclusions relating to the role of out of plane curvature. It is of particular concern in the interpretation of F-actin staining, where a supracellular actin ring is proposed to exist within the well, but this may simply be that the imaging axis is no longer aligned with the apicobasal axis, giving the appearance of an enriched actin stain. To address this, authors should validate their imaging by performing similarly spaced z-stack scans on wells that have been rotated relative to the z-axis of the confocal. In addition, authors should implement correction algorithms such as the one introduced (open source) by Herbert and colleagues, to examine the extent to which curvature influences their interpretation. Validation and curvature correction would significantly strengthen the manuscript by addressing this technical concern.

We agree with the Reviewer that imaging cytoskeletal components and nuclei in curved epithelial monolayers with conventional confocal microscopy may introduce certain artifacts that can affect the interpretation of our results. This aspect has been considered in our work and several precautions have already been taken, but we realized that our methodology was not sufficiently detailed in the previous version of the manuscript, giving rise to legitimate concerns on the part of the reviewer. We present below a more detailed description of our approach and new experiments which have been carried out based on the Reviewer's suggestions.

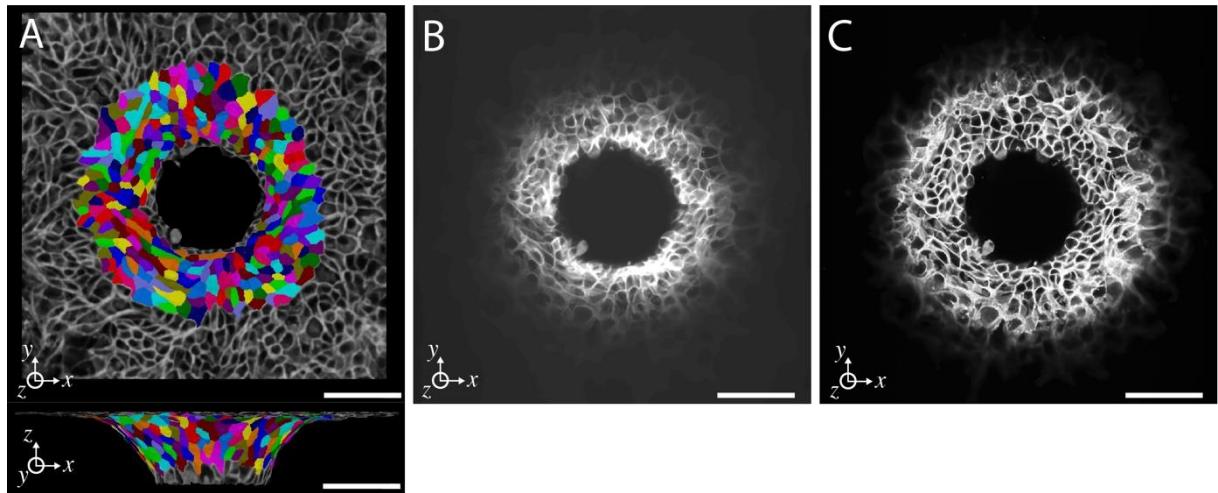
**- The optical set-up:** Most of the 3D images were acquired on an inverted Nikon Ti2 A1R HD25 confocal microscope using high resolution silicon immersion lenses (Nikon). We used lenses of the Plan Apochromat objective lens series from Nikon that provides the one of the world's highest levels of numerical aperture (N.A.) and Working Distance (W.D.). Images were acquired with:  $\times 25$  (N.A.=1.05, W.D.=0.55 mm),  $\times 40$  (N.A.=1.25, W.D.=0.30 mm) and  $\times 100$  (N.A.=1.35, W.D.=0.30 mm) objectives. These lenses have excellent optical performance over the entire field of view, and chromatic aberration correction across a wide wavelength range. Images were acquired using small Z-depth increments of 0.125  $\mu\text{m}$  and the NIS Elements imaging software (NIS Elements Advanced Research v5.2).

**- The confocal mode:** The confocal microscope used in this work is a confocal microscope scanning unit equipped with a high-resolution galvanometer-based scanner (4,096 x 4,096 pixels; non-resonant) and a high-speed resonant scanner, a continuously variable hexagonal pinhole. The hybrid scan head incorporates both the high-resolution galvano (non-resonant)

scanner and an ultrahigh-speed resonant scanner. Although image distortion induced by non-linear resonant galvanometer scanning is now fortunately predictable and can be corrected using either software or hardware solutions, confocal scanning were acquired in galvano (non-resonant) scanner mode. Regardless of the correction scheme involved to produce images, we used the most effective scanning strategy that involves collecting data during both the forward and backward scans of the galvanometer mirror.

- **Flat-field correction (FFC):** We used the FFC technique to improve image quality and to cancel the effects of image artifacts caused by variations in the pixel-to-pixel sensitivity of the detector and by distortions in the optical path. Standardization in fluorescence microscopy involves calibration of intensity in reproducible units and correction for spatial nonuniformity of illumination (flat-field or shading correction). Both goals can be achieved using concentrated solutions of fluorescent dyes. When a drop of a highly concentrated fluorescent dye is placed between a slide and a coverslip it produces a spatially uniform field, resistant to photobleaching and with reproducible quantum yield. In this work, we used the Fiji plugin BaSiC, an image correction method based on low-rank and sparse decomposition (Tingying Peng et al. Nature Communications 2017, [10.1038/ncomms14836](https://doi.org/10.1038/ncomms14836)). In comparison to existing shading correction tools, BaSiC achieves high accuracy with significantly fewer input images, works for diverse imaging conditions and is robust against artefacts. Moreover, it can correct temporal drift in time-lapse microscopy data and thus improve continuous single-cell quantification. This correction improved the quantification of our confocal images, which are less confounded by uneven illumination (shading) in space and background variation in time.

- **2D projection of curved epithelial monolayers:** We thank the Reviewer for suggesting referring to the work of Herbert et al. BMC Biology 2021. The LocalZprojector toolbox plugin is very helpful to work on curved image and this correction algorithm has been implemented in previous analyses. We apologize for the lack of details in the previous version of the manuscript, giving rise to legitimate concerns about the method used to project 3D images of curved epithelial monolayers on 2D surfaces. This correction algorithm was used to project confocal images of m-cherry cadherin MDCK cells to determine the surface area of individual cells at the Gaussian curvature zone (**Rebuttal Fig. 3A**), which cannot be determined from a typical averaged Z-stack projection (**Rebuttal Fig. 3B**). As shown in the **Rebuttal Fig. 3C**, projection images of the Gaussian curvature zone were obtained using standard deviation (std) filter for height map and the MIP (maximum intensity projection) method for local projection. In addition to this method, the surface area of each individual cells was determined using the 3D analysis package of the NIS Elements imaging software (NIS Elements Advanced Research v5.2). We did not observe significant differences between both methods. The method section of the revised paper has been revised to details about this correction.

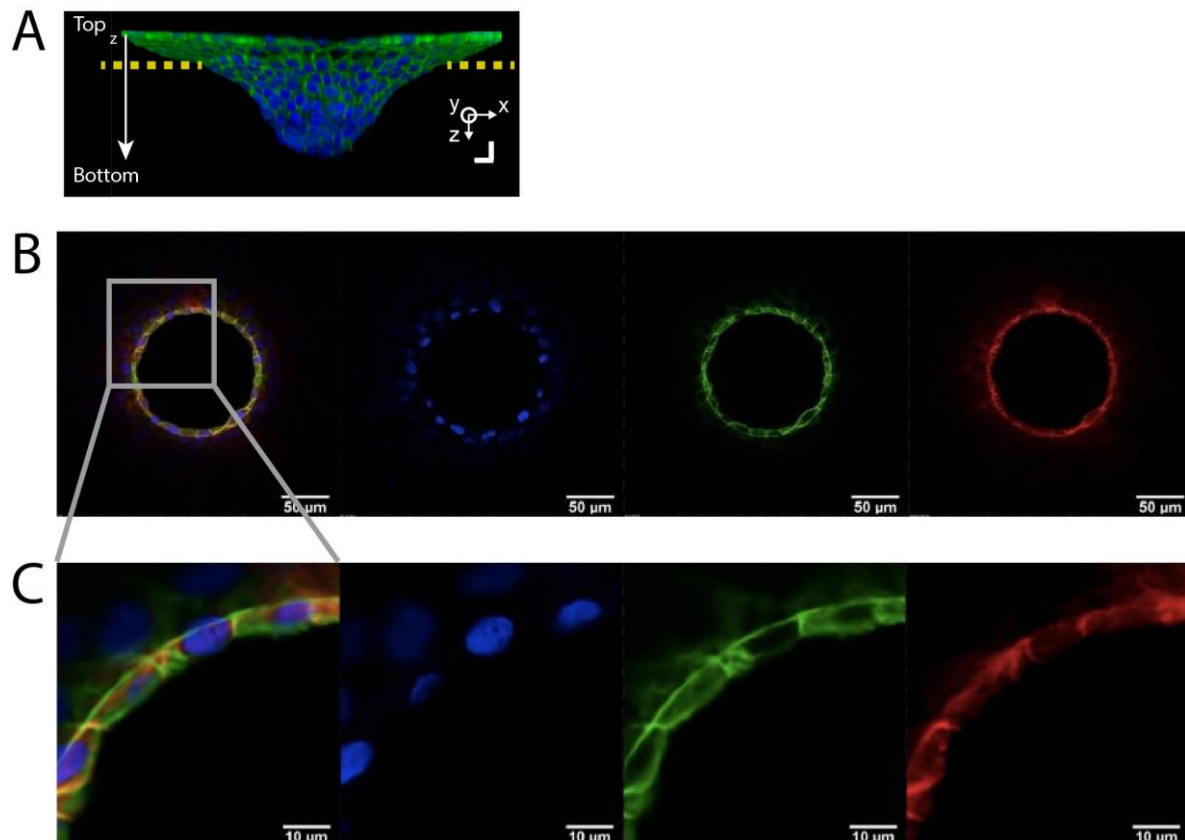


**Rebuttal Figure 3:** (A) Normal and side confocal views of individual cells located at the Gaussian curvature zone of a microwell of 100  $\mu\text{m}$  in radius. Cells were segmented on m-cherry cadherin confocal images using MorphoGraphX. (B) Typical averaged Z-stack projection of the Gaussian curvature zone ( $n=116$  Z-slices) obtained in Fiji. (C) Projection image of the Gaussian curvature zone ( $n=116$  Z-slices) obtained using the LocalZprojector toolbox plugin in Fiji using standard deviation (std) filter for height map and the MIP (maximum intensity projection) method for local projection.

**- Imaging axis and upright set-up:** The reviewer suggests checking that the appearance of an enriched actin spot is not an optical artifact induced by the imaging axis which may no longer be aligned with the apicobasal axis. In this situation, the circular actin ring would most likely be characterized by a variation in intensity along its perimeter, which has not been observed experimentally (revised **Fig. 3D**). To address the Reviewer's comment, we performed several additional experiments. First of all, microwells of 30, 65 and 100  $\mu\text{m}$  in radius were imaged upside down on the same inverted microscope (Nikon Ti2 A1R HD25) and we confirmed the results presented in **Fig. 3D**. Then these microwells were imaged on an upright LSM 710 microscope with a water immersion Plan-Apochromat 20x/1.0 N.A. DIC objective (Carl Zeiss, Oberkochen, Germany), as recently used to image curved epithelial monolayers obtained by rolling (Caterina Tomba et al. *Developmental Cell* 2022). We observed the presence of an actin ring, which was weaker and discontinuous at high in-plane curvatures, and thicker and continuous at low in-plane curvatures (100  $\mu\text{m}$  in radius), confirming the results obtained on our optical system and presented in **Fig. 3D of the revised manuscript**.

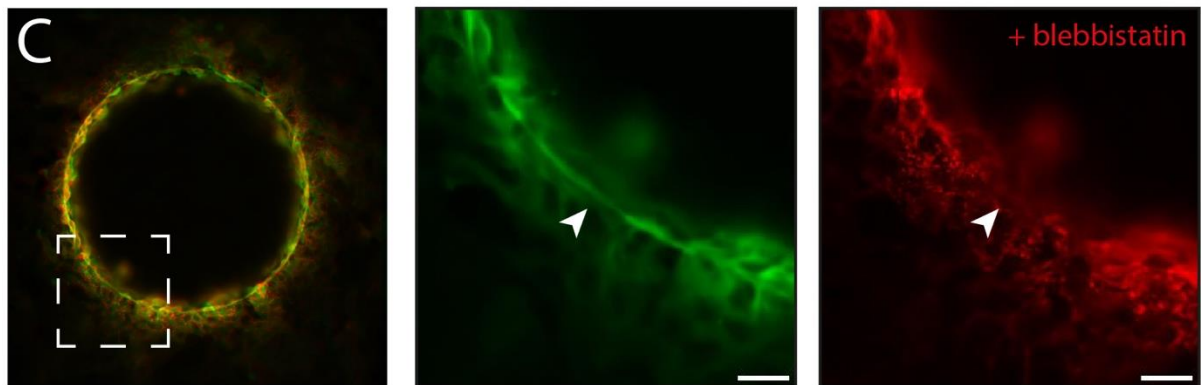
**- Live imaging at multiple wavelengths:** If some optical artifacts are induced by the imaging axis, it should also affect other wavelengths. To test this hypothesis, we performed live confocal imaging of m-cherry E-cadherin MDCK cells, phalloidin AlexaFluor 488 and Hoechst 33342 to observe simultaneously cadherin-based cell-cell junctions, actin filaments and nuclei, respectively. As shown in **Rebuttal Fig. 4**, a circular actin ring was clearly observed in FITC, while we did not observe an enriched TRITC-enriched cadherin signal in the same focal plane. In addition, we can observe an indentation of some nuclei by the actin stress fibers,

demonstrating a direct interaction between the actin ring and the nuclear lamina as reported previously on micropatterned endothelial cells (M. Versaevel et al. Scientific Reports 2014).



**Rebuttal Figure 4: Live observation of the actin ring and cadherin-based cell-cell interactions.** (A) The actin supracellular structure was observed by high resolution confocal microscopy using a  $\times 40$  silicone immersion objective (N.A.=1.25, W.D.=0.30 mm) and a Z step of 150 nm. 3D confocal side view of MDCK cells grown in a 100  $\mu\text{m}$ -radius microwell with a yellow dashed line corresponding to the confocal plane where the actin ring was observed. (B) Confocal images and (C) zooms showing the actin cytoskeleton in green (AlexaFluor488 Phalloidin), cell-cell junctions in red (m-cherry cadherins) and nuclei in blue (Hoechst 33342). Scale bars are 50  $\mu\text{m}$  (B) and 10  $\mu\text{m}$  (C).

**- Live imaging and actomyosin inhibition:** We then carried out perturbations experiments to disrupt actomyosin contractility in the actin ring by using blebbistatin, which inhibits myosin ATPase activity and suppresses actomyosin contraction. In addition to previous results obtained in immunostained cells, these new experiments were performed in live confocal imaging mode. The actin supracellular structure was observed by high resolution confocal microscopy using a  $\times 40$  silicone immersion objective (N.A.=1.25, W.D.=0.30 mm) and a Z step of 150 nm. Blebbistatin was added after 1 hour 30 minutes of confocal time-lapse imaging, and the total acquisition time was 10 hours. As shown on **Rebuttal Fig. 5**, the disruption of the actomyosin contractility with blebbistatin resulted in a severe collapse of the supracellular actin cable, demonstrating that the observation of an actin ring in confocal imaging is not related to an optical artefact.



**Rebuttal Figure 5** – Inhibition of the actomyosin contractility in live imaging conditions. Representative top-view live confocal images of the actin ring in a microwell of 100  $\mu\text{m}$  in radius with a zoomed section before the blebbistatin treatment (in green) and after the blebbistatin treatment (in red). White arrow shows the collapse of the actin cable in blebbistatin-treated cells. The actin supracellular structure was observed by high resolution confocal microscopy using a  $\times 40$  silicone immersion objective (N.A.=1.25, W.D.=0.30 mm) and a Z step of 150 nm. Blebbistatin was added after 1 hour 30 minutes of confocal time-lapse imaging, and the total acquisition time was 10 hours. The scale bar is 10  $\mu\text{m}$ .

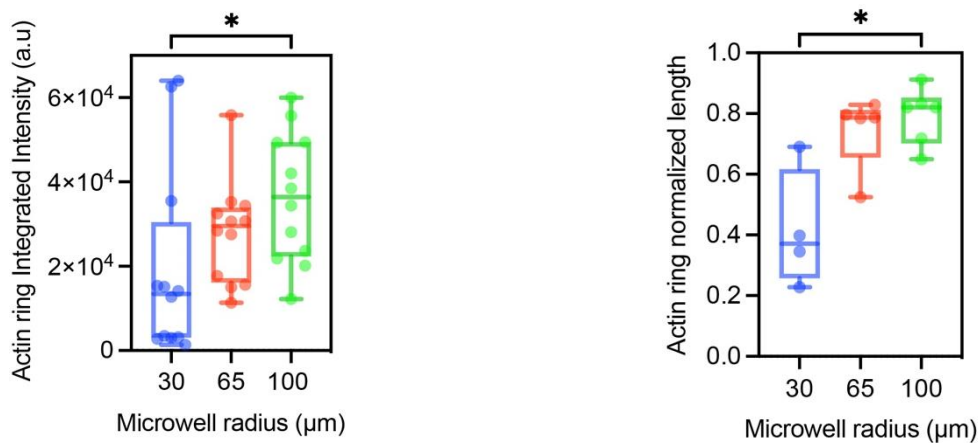
**A3.** There are many potentially interesting observations are not sufficiently followed up on, as well as potential advantages of this system that are not fully utilized in support of the goals of the work. For example, it is very interesting that no supracellular actin cable is observed in the smallest well size, and while one could exploit this to understand why or how the cable forms, authors simply state this observation and move on. Similarly, the presence of both convex curvatures proximally and concave curvature distally in the same system provides an exciting juxtaposition make use of to further understand how or why some of these behaviors are induced, but authors do not expand their investigation beyond the surface and the most superficial layers of the well. This speaks to a consistent issue throughout with focusing on characterization without digging into the underlying mechanisms at play, if even in a general sense.

We thank the Reviewer for pointing this and we agree with the reviewer that providing additional data on the individual role of in-plane and Gaussian curvatures on the formation of the supracellular actin cables could be very helpful to better understand the underlying mechanism. We examined in more depth the organization of the actin cytoskeleton around the microwell edge. To this aim, we performed confocal imaging within a short range of focal planes close to the microwell edge (yellow line) (**Fig. 3C of the revised manuscript**). Our results indicated that actin accumulated at the microwell edge to form a well-defined supracellular cable-like structure, resembling a purse string and extending along the edge perimeter (**Fig. 3C of the revised manuscript and Rebuttal Fig. 4**). Previous studies reported actin ring structures in various developmental and physiological processes [25] previous works using flat epithelial monolayers indicated that such supracellular actin cables sense and respond to the in-plane local curvature of the gap (SRK Vedula et al. Nat Mater 13, 87-96 2014 + T.



Chen et al. Nat Phys 15, 393-402 2019 + Q. Wei et al. PNAS 117, 33263-33271 2020), contracting and pulling the follower cells to heal the wound.

We now present in our revised manuscript a more robust analysis of the supracellular actin structures by quantifying their integrated intensity (**Rebuttal Fig. 6 left**) and length (**Rebuttal Fig. 6 right**) in 30  $\mu\text{m}$ , 65  $\mu\text{m}$  and 100  $\mu\text{m}$  radius microwells. Our new results indicated that supracellular cables were weaker and discontinuous at high in-plane curvatures, while low in-plane curvatures were characterized by thicker and continuous cable structures.



**Rebuttal Figure 6** –Integrated intensity (left) and normalized length (right) of the actin ring for microwell radii of 30  $\mu\text{m}$  (in blue), 65  $\mu\text{m}$  (in red) and 100  $\mu\text{m}$  (in green).

We then followed reviewer’s advice by using more targeted approaches to change one variable (e.g. in plane curvature) without affecting all other variables (see comment A1). To this aim, we developed two-dimensional (2D) adhesive micropatterns of similar diameters and consequently in-plane curvature. We used 2D circular adhesive (**Rebuttal Fig. 2a**) and non-adhesive (**Rebuttal Fig. 2b**) micropatterns of 100  $\mu\text{m}$  in radius to impose similar in-plane curvatures to epithelial monolayers than those observed in 3D microwells. By using this strategy, we aimed to decouple the individual role of in-plane and Gaussian curvatures in the formation of supracellular actin cables by quantifying the amount of actin signal in a supracellular actin cables and their normalized length. As shown in **Rebuttal Fig. 2c-d**, we observed the formation of a supracellular actin cable on both conditions, which contain a similar amount of actin than observed in 3D microwells (**Rebuttal Fig. 2e**). Surprisingly, our findings showed that the length of supracellular actin cables normalized by the total perimeter was significantly larger in 3D microwells than on adhesive and non-adhesive circular patterns (**Rebuttal Fig. 2f**). Altogether, our findings showed that the Gaussian curvature imposed at the microwell entrance by its 3D morphology promotes the maturation of the supracellular actin cable architecture. The **Rebuttal Fig. 2** has been now added as **Supplementary Figure 4** in the revised manuscript. The legend and the method section have been modified accordingly.

**A4.** Related to above concerns, the z-resolution of the imaging setup must be reported.

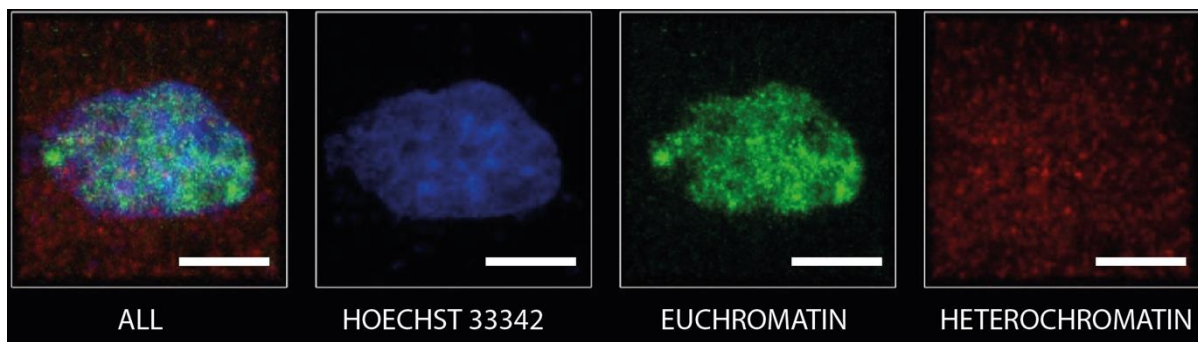
Confocal images of live and immunostained tissues in microwells were acquired with a motorized inverted confocal microscope (Nikon TI2 A1R HD25, Japan) equipped with  $\times 40$

CFI Plan Apochromat Lambda Silicon objectives, which closely matches the refractive index of cells. The numerical aperture of 1.25 combined with the large field of view of 25mm enables 3D data acquisition in confocal mode at high resolution. Confocal images were acquired in resonant mode using small Z-depth increments of 0.125  $\mu\text{m}$  and processed using the NIS-Elements software. The method section has been updated in the revised version of the manuscript.

**A5.** No references are provided for distinguishing between hetero and euchromatin simply from DAPI signal intensity. This must be validated using more conventional approaches for assessing chromatin accessibility, such as histone acetylation detection.

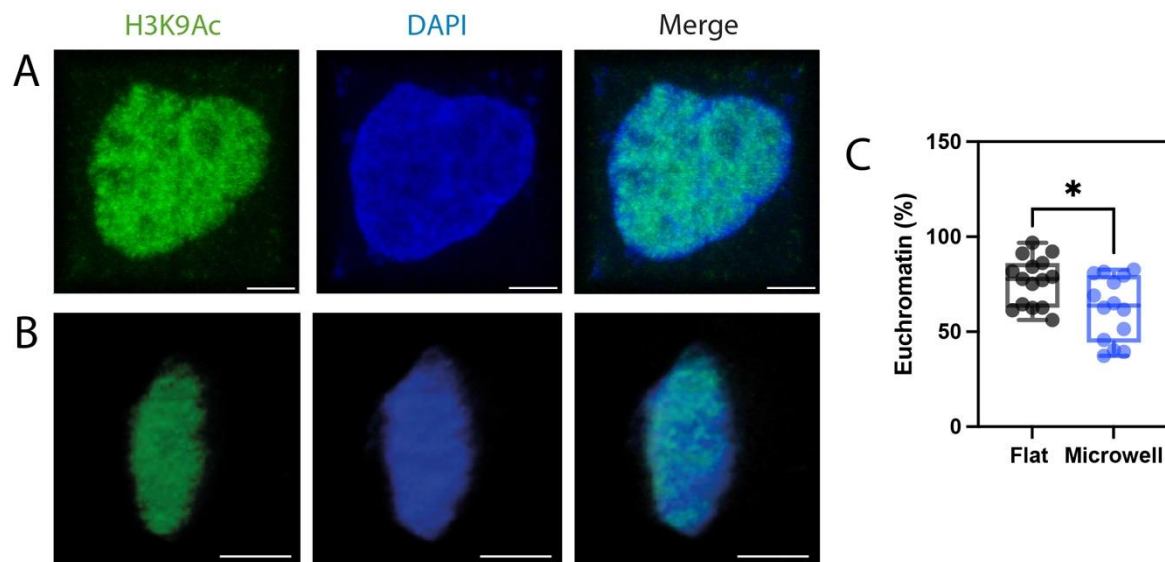
In the previous version of our manuscript, we investigated whether nuclear elongations observed at the Gaussian zone of the microwell entrance could lead to differences in chromatin state by using quantitative procedures based on DAPI staining and 3D confocal imaging at high magnifications. We determined the average spatial density of chromatin, which is a reliable indicator of chromatin condensation, and showed that elongated nuclei localized at the maximal Gaussian curvature zone exhibited higher levels of fluorescence intensity (**Fig. 6g, revised manuscript**) compared to rounded nuclei in flat zones (**Fig. 6h, revised manuscript**). Our findings revealed higher chromatin compaction values in Gaussian curvature zones ( $0.39\pm 0.11$ , **Fig. 6i, revised manuscript**) than in flat ones ( $0.17\pm 0.13$ ). These results suggest that the Gaussian curvature imposed at the microwell entrance leads to a nuclear elongation, which is accompanied by higher levels of chromatin condensation.

To go one step further in assessing chromatin accessibility, we tested specific antibodies for euchromatin (H3KP9ac antibody, #MA5-11195 ThermoScientific) and heterochromatin (Anti-Histone H3 trimethyl K27 antibody, mAbcam 6002) on control MDCK monolayers. MDCK cells in monolayers were fixed and permeabilized with a 10 min incubation in PAF 4% and Triton X-100 1:2000. Cells were blocked with a 30 min incubation in Tris-Tween 0,1% buffer with BSA 1% and stained for chromatin with a 1 hour incubation with DAPI, euchromatin with a 1 hour incubation with 1/200 H3KP9ac antibody (MA5-11195 ThermoScientific), 3 rinses in Tris-Tween 0,1% buffer, 30 min each rinse, then a 1 hour incubation with 1/200 anti-rabbit FITC, and heterochromatin with a 1 hour incubation with 1/200 Anti-Histone H3 (tri methyl K27) antibody [mAbcam 6002], 3 rinses in Tris-Tween 0,1% buffer, 30 min each rinse, then a 1 hour incubation with 1/200 anti-mouse TRITC antibody.

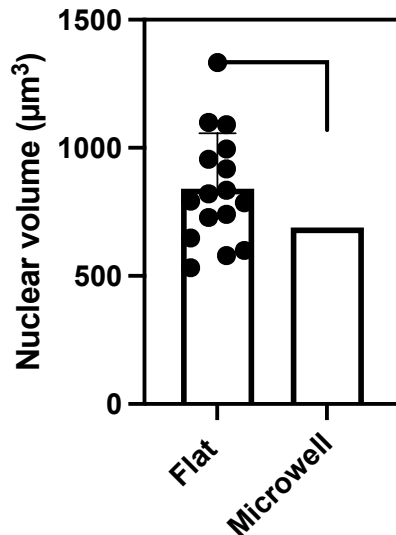


**Rebuttal Figure 7 – Immunostaining of euchromatin and heterochromatin in MDCK monolayers.** Representative confocal images of the staining of DNA (DAPI, in blue), euchromatin (H3K9ac antibody, in green) and heterochromatin (Anti-Histone H3 trimethyl K27 antibody, in red) in MDCK cells. Scale bars are 10  $\mu\text{m}$ .

As shown in **Rebuttal Fig. 7**, the heterochromatin signal-to-noise ratio was very weak despite changing many experimental parameters (incubation time, buffer, permeabilization, etc.). We therefore characterized in the revised manuscript the level of histone H3 acetylation at lysine 9 (H3K9ac) to determine the level of euchromatin histone marks, which correspond to the loosely packed chromatin domain that is transcriptionally accessible (Y. Kalukula et al. Nat Rev Mol cell Biol 2022). Interestingly, elongated nuclei located at Gaussian curvature zones exhibited a lower percentage of euchromatin (**Rebuttal Fig. 8**) and a lower volume (**Rebuttal Fig. 9**), further confirming a highly compacted chromatin state. The new results presented in **Rebuttal Figs. 8 and 9** were incorporated in the **Fig. 6 f-k** of the revised manuscript.



**Rebuttal Figure 8 – Quantification of chromatin accessibility.** Representative confocal images of the fluorescent signal of euchromatin (H3K9ac) and DNA (DAPI) in the nuclei of cells grown on a (A) flat region around the microwell and (B) at the Gaussian curvature zones of microwells of 30  $\mu\text{m}$  in radius. Scale bars are 10  $\mu\text{m}$ . (C) Volume percentage of euchromatin in MDCK cells grown in flat region around the microwell (in black) and (B) at the Gaussian curvature zones (in blue) of microwells of 30  $\mu\text{m}$  in radius.



**Rebuttal Figure 9** –Nuclear volume in MDCK cells grown in flat region around the microwell (in black) and (B) at the Gaussian curvature zones (in blue) of microwells of 30 µm in radius.

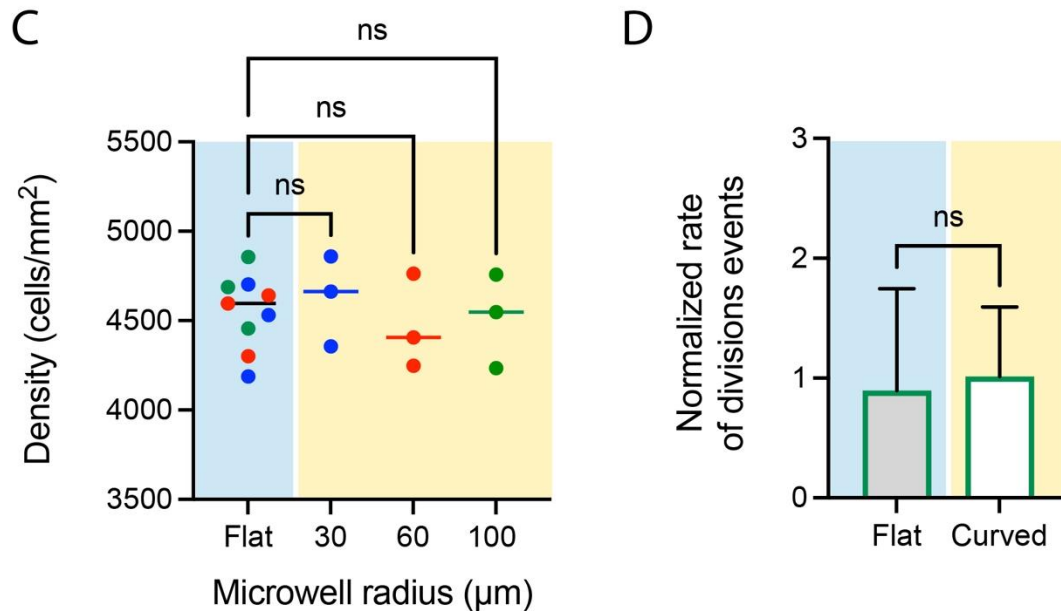
**A6.** The experiment performed to study the speed of the cells needs a few clarifications. How is the tracking of the nuclei performed on the curved surface? If the timelapse is done in 2D, validation is needed for the ability to faithfully track a nucleus over time, free from out of plane artifact. More details in the method used are needed here.

We apologize for the lack of details about the tracking procedure in the method section previous version of the manuscript, giving rise to legitimate concerns about the method used to track nuclei of curved surfaces. The cell tracking was performed in confocal microscopy using a resonant scanner mode (Nikon A1R HD25, Japan) and by limiting the range of Z-stacks around the Gaussian curvature zone. The motion of each individual cells was determined across time in Z-stacks using the 3D tracking plugin package of the NIS Elements imaging software (NIS Elements Advanced Research v5.2).

**A7.** Similarly, clarifications on the method used are needed for the time lapse experiments investigating collective cell migration at the entrance of the well. Are they initiated when cells are confluent? How long does it take between plating the cells and reaching confluence? Is the cell density isotropic (same in plane and out of plane) ?

Briefly, hydrogels were sterilized by a germicide UV treatment of 15 min and incubated with 75 µg/ml solution of fibronectin for 1 hour and then rehydrated before cell seeding in sterile medium at 37°C for 4 hours. MDCK cells were seeded on microstructured hydrogels at 100,000 cells/cm<sup>2</sup> and incubated for 24 hours at 37°C with 5% of CO<sub>2</sub> in a humidity-saturated environment. Time-lapse experiments at 10-minute time intervals for a total duration of 10 hours were carried out after 24 hours of incubation using a cage incubator (Okolab) to maintain the temperature at 37°C, 5% CO<sub>2</sub> level and a high level of humidity. We have shown that cells reached confluence after 24 hours in culture (see Fig. 1H-J), meaning that time-lapse experiments were started at confluency. The cellular density was statistically similar on flat zones around the microwell and at the Gaussian curvature zones, regardless the microwell

diameter (**Rebuttal Fig. 10C**). In addition, we did not observe any significant difference of division rate between flat and Gaussian curvature zones (**Rebuttal Fig. 10D**). These new results are now presented in the **Supplementary Fig. 2** of the revised manuscript and the method section on time-lapse acquisition has been rewritten to clarify the method used.



**Rebuttal Fig. 10** – (C) Cellular density in flat (light blue box) and Gaussian curvature (yellow box) zones for microwell radius of 30 μm (in blue), 65 μm (in red) and 100 μm (in green). (D) Normalized rate of division events in flat (light blue box) and Gaussian curvature (light yellow box) zones of a microwell of 100 μm in radius. n.s. is not significant.

**A8.** Some mitotic cells are visible in the time lapses. It may be interesting to track/quantify these in relation to well geometry to assess whether direction and quantity of cell divisions are under macroscopic influence of tissue geometry.

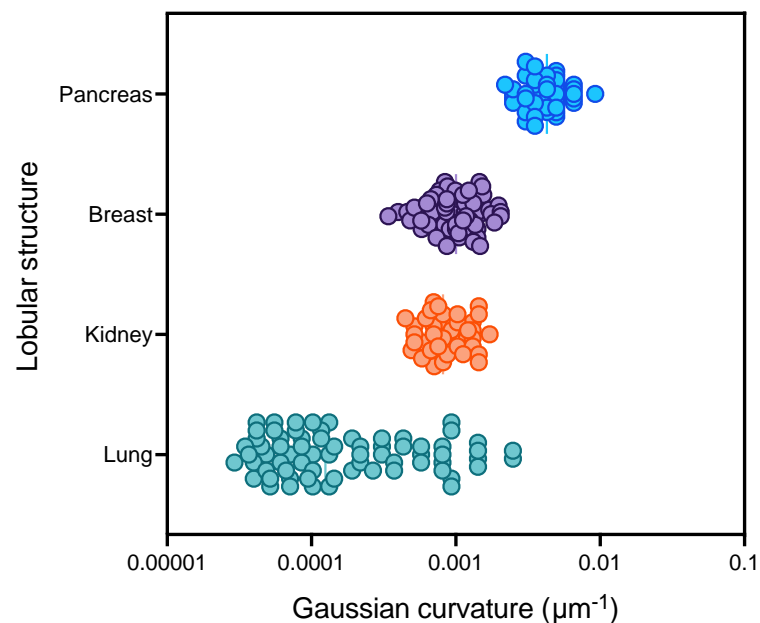
We agree with Reviewer, some mitotic cells can be observed in time-lapse movies, which can be therefore used to quantify the division rate at specific location of the microwells. We thank the Reviewer for this interesting suggestion.

As already described in comment #A1 and **Rebuttal Fig. 1D**, the proliferation rate was determined from time-lapse experiments (n=3) of 10 hours at two distinct zones of the microwells of similar surface areas. The first zone (in light blue) corresponds to the flat area surrounding the curved edge of the microwells, where the in-plane curvature is determined by the diameter of the well. The second region corresponds to the maximal Gaussian curvature zone (in light yellow) at the microwell entrance. The number of division events for both zones was then normalized by the number of division events observed on flat zone of the sample but far away from the microwell. After normalization, our results both zones exhibited rates of division events very close to 1 (**Rebuttal Fig. 1D**), demonstrating that the division rate in different zones of 3D microwells was very similar to flat surfaces. The **Rebuttal Fig. 1** has

been now added as **Supplementary Figure 2** in the revised manuscript. The legend and the method section have been modified accordingly.

**A11.** Justification should be provided for the particular matrix modulus, well diameters, well spacing, and other parameters that have been selected. If these are chosen to mimic particular in vivo settings, references should be provided to highlight this.

We appreciate the comments by the reviewer, as we do agree this is an important point. Increasing evidence suggests that three-dimensional (3D) substrate curvature plays a critical role in cellular organization. Indeed, epithelial tissues, such as lung alveoli, kidney glomerulus, intestinal villi, and breast acini, exhibit complex morphologies dominated by curved surfaces. To address the Reviewer comment, we quantified the curvatures in lobular structures in four different human organs: the lung (Conrad, L. et al. The biomechanical basis of biased epithelial tube elongation in lung and kidney development. *Development* 148, dev194209 2021), kidney (Mederacke, M., Conrad, L., Vetter, R. & Iber, D. Geometric Effects Position Renal Vesicles During Kidney Development. <http://biorxiv.org/lookup/doi/10.1101/2022.08.30.505859> 2022), breast (Peurla, M. et al. Morphometric analysis of the terminal ductal lobular unit architecture in human breast. <https://www.biorxiv.org/content/10.1101/2023.03.12.532249v1.full.pdf>), and pancreas (Messal, H. A. et al. Tissue curvature and apicobasal mechanical tension imbalance instruct cancer morphogenesis. *Nature* 566, 126–130 2019) (**Rebuttal Fig. 11**).

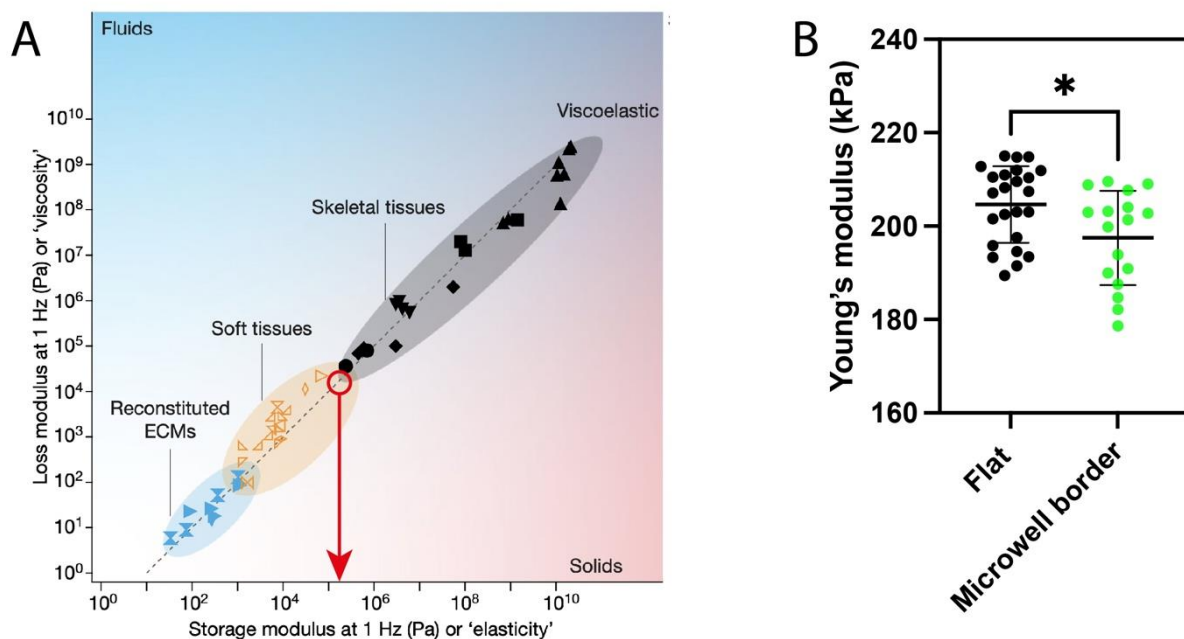


**Rebuttal Figure 11 – Curvature in lobular structures.** Typical Gaussian curvatures in lobular structures of four human organs: lung (in green), kidney (in orange), breast (in purple) and pancreas (in blue).

Interestingly, we showed that the Gaussian curvature zone at the entrance of the bowl-shaped microwells (see light yellow box in **Fig. 2b-c of the revised manuscript**) matched the range of Gaussian curvatures observed in anatomical lobular structures of the lung, kidney,

breast, and pancreas. These new results support therefore the clinical relevance of our platform to mimic the curvature found in complex lobular structures. The **Rebuttal Fig. 11** is now presented as **Fig. 2e in the revised manuscript** and the bibliography has been updated.

The bowl-shaped microwells used in this work must have a stiffness in agreement with the range of stiffnesses observed in soft tissues, such as breast, bladder, liver, lung, skin or kidney. Sneider et al. showed that the Young's modulus of breast tissues is dependent on its composition (Sneider A et al. Biomaterials 2022). Indeed, it exists a strong correlation between the amount of straight collagen and global breast stiffness, leading to cancer breast tissues with Young's moduli in the range of the hundreds of kPa. This range of stiffnesses were confirmed recently by Chaudhuri et al. (O. Chaudhuri et al. Nature 584, 535–546. 2020) by considering that soft tissues (bladder, liver, lung, skin, kidney for example) exhibit a mean stiffness around  $10^5$  Pa (**Rebuttal Fig. 12A**). We used nanoindentation measurements (Chiaro, Optics 11) on immersed microwell of 100  $\mu\text{m}$  in radius to determine the elastic modulus at the flat zone around the microwell and at its Gaussian curvature zone. We found a value of  $198 \pm 10$  kPa at the Gaussian curvature zone (**Rebuttal Fig. 12B**), which is in very good agreement with the stiffness range of soft tissues reported in the literature (see comment #B3 for details).



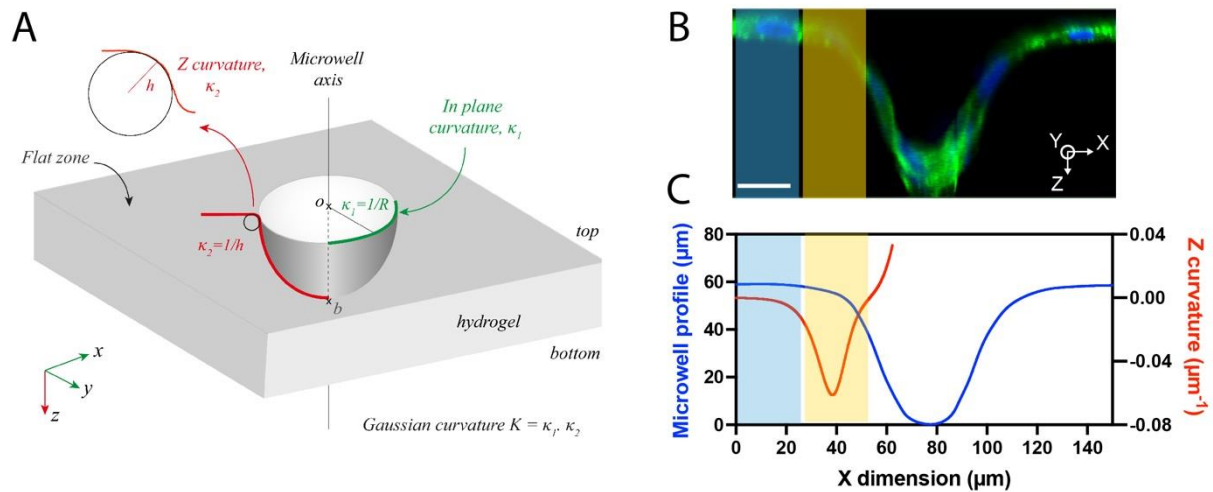
**Rebuttal Figure 12** – (A) Linear evolution of the loss modulus as a function of the storage modulus for reconstituted extracellular matrices (in light blue), soft tissues (in light orange) and skeletal tissues (in light grey), giving approximately a  $\tan(\sigma)=0.1$ . Source: O. Chaudhuri et al. Nature 584, 535–546 (2020). (B) Young's modulus values obtained by nanoindentation on flat zones (black points,  $n=24$ ) around the microwell and at its Gaussian curvature zone (green points,  $n=18$ ) of a microwell of 100  $\mu\text{m}$  in radius. A minimum of 3 replicates was used for each condition;  $*p < 0.05$ .

**A12.** The statement that "findings ..." is misleading, as in this experiment the force generating ability of edge cells themselves were also disrupted.

We assume that the Reviewer's comment is related to the perturbation of the actomyosin contractility using Blebbistatin. We agree with the Reviewer and this section of the manuscript has been rewritten to avoid overstatement.

**A13.** Data presentation in Fig 5b and 5c could be improved by combining onto a single plot with two y-axes

We thank the Reviewer for this suggestion of presentation, which has been adopted in the revised manuscript by plotting the microwell profile the Z curvature on different Y axis of the same plot. The resulted graph is presented in the **Rebuttal Fig. 13C** which has been incorporated in the **Fig. 2 of the revised manuscript**.



**Rebuttal Figure 13 – Gaussian curvatures at the entrance of 3D synthetic microwells.** (A) Bowl-shaped 3D microwells were characterized by a combination of an in-plane ( $xy$ , in green) curvature,  $\kappa_1$ , determined by the microwell radius,  $R$ , as  $\kappa_1=1/R$ , with a  $Z$  ( $xz$ , in red) curvature  $\kappa_2$  localized at the microwell entrance and determined as  $\kappa_2=1/h$ , with  $h$  the microwell depth. A flat hydrogel zone surrounds each 3D microwell. The Gaussian curvature  $K$  at the microwell entrance corresponds to  $K = \kappa_1 \times \kappa_2$ . (B) Representative confocal profile of a microwell of  $30 \mu\text{m}$  in radius covered with a monolayer of epithelial cells stained for actin (in green) and DNA (in blue). (C) Profile of a microwell of  $30 \mu\text{m}$  in radius (in blue) and the corresponding  $Z$  curvature (in red) calculated at each point of the microwell profile. The light blue box on (B) and (C) represents the flat zone around the microwell, while the light-yellow box delimits the Gaussian curvature zone at the microwell entrance.

---

## Response to Reviewer #2

---

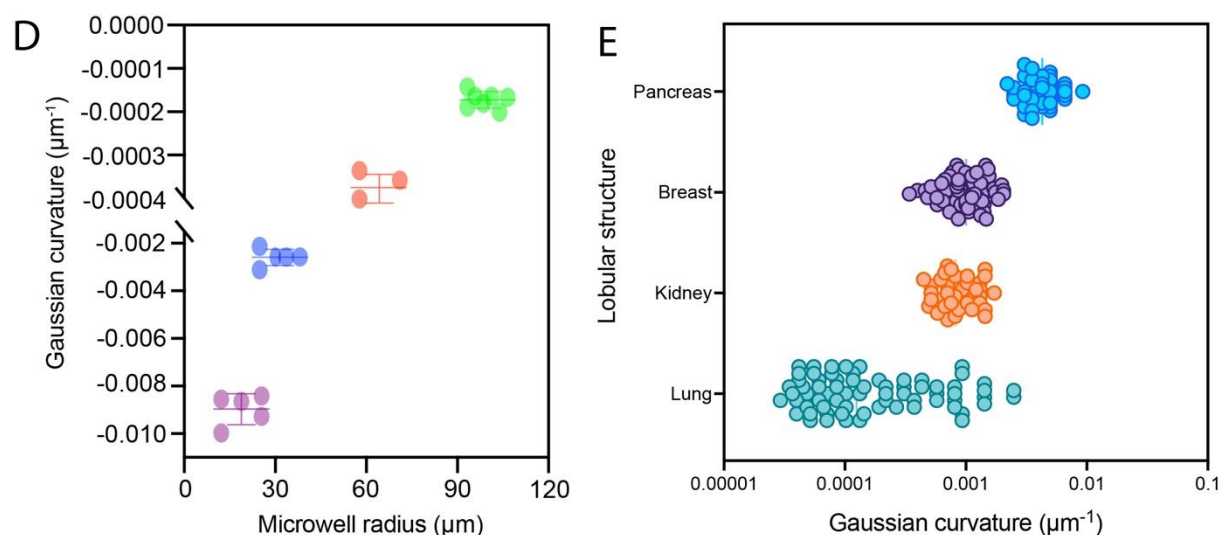
The authors provide striking imaging to support a new platform for interrogating curvature sensing in epithelia. Addressing the following issues in approach and presentation would enhance the product.



**B1.** The authors state that they "photopolymerize microwells of various diameters in hydrogels to form curved epithelial structures" that recapitulate "breast epithelial lobules" among other anatomic structures. A more detailed correlation of the dimensions, curvatures and aspect ratios chosen for this study with the target anatomic structures would lend clinical relevance to this rationale for the experimental approach.

We thank the Reviewer for pointing out that a more detailed description of the different curvatures found in anatomic lobular structures would support the clinical relevance of our new platform. To address this comment, we first quantified the Gaussian curvatures at the entrance of bowl-shaped microwells of with radii of 25  $\mu\text{m}$ , 30  $\mu\text{m}$ , 65  $\mu\text{m}$  and 100  $\mu\text{m}$  (**Rebuttal Figure 14D**). Our findings revealed that as the bowl-shaped microwell radius increased from 25 to 100  $\mu\text{m}$ , the Gaussian curvature at the microwell entrance decreased from approximately  $-10^{-2}$  to  $-10^{-3}$   $\mu\text{m}^{-1}$ . Importantly, we demonstrated a strong correspondence between this range of Gaussian curvatures and the typical values of Gaussian curvature observed in anatomic lobular structures within the lung (Conrad, L. et al. The biomechanical basis of biased epithelial tube elongation in lung and kidney development. *Development* 148, dev194209 2021), kidney (Mederacke, M., Conrad, L., Vetter, R. & Iber, D. Geometric Effects Position Renal Vesicles During Kidney Development. <http://biorxiv.org/lookup/doi/10.1101/2022.08.30.505859> 2022), breast (Peurla, M. et al. Morphometric analysis of the terminal ductal lobular unit architecture in human breast. <https://www.biorxiv.org/content/10.1101/2023.03.12.532249v1.full.pdf>), and pancreas (Messal, H. A. et al. Tissue curvature and apicobasal mechanical tension imbalance instruct cancer morphogenesis. *Nature* 566, 126–130 2019) (**Rebuttal Figure 14E**). Our results underscore therefore the clinical relevance of utilizing bowl-shaped microwells to investigate the mechanoresponse of curved epithelial monolayers that line lobular structures.

The main text of the manuscript has been revised, the **Rebuttal Fig. 14** is now presented as **Fig. 2e** in the revised manuscript and the bibliography has been updated accordingly.

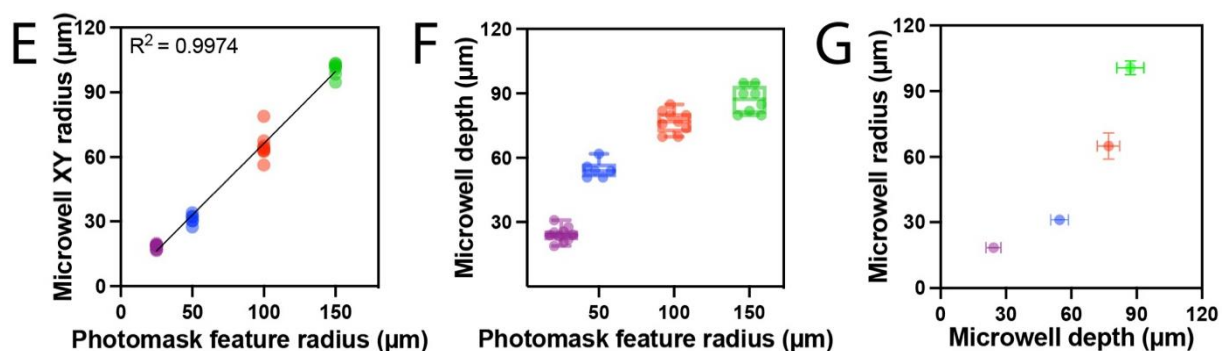


**Rebuttal Figure 14** – (D) Gaussian curvature at the entrance of microwells with radius of 25  $\mu\text{m}$  (in purple), 30  $\mu\text{m}$  (in blue), 65  $\mu\text{m}$  (in red) and 100  $\mu\text{m}$  (in green). Each point corresponds to one replicate with  $n \geq 5$  microwells per replicate. (E) Typical Gaussian curvatures in the

lobular structures of four human organs: lung (in green), kidney (in orange), breast (in purple) and pancreas (in blue).

**B2.** The separate handling of 'in-plane' and 'out-of-plane' curvatures is interesting but the interrogation of hierarchical interactions between them and/or the addition of varying aspect ratios would more completely address the state-of-the-art. The authors report that "microwell depth was determined by confocal microscopy (Fig. 1f), allowing us to establish the relationship between radius and depth of the microwells (Fig. 1g)". Graded manipulation of the aspect ratio of the microwells would provide an important additional data set.

We used a new photomask pattern of 25  $\mu\text{m}$  in radius to create smaller 3D microwells of  $18\pm 1$   $\mu\text{m}$  in radius (**Rebuttal Figure 15E**) and  $24\pm 3$   $\mu\text{m}$  in depth (**Rebuttal Figure 15F**). These new results showed that the photomask-based UV photoillumination technique described here can be used to form 3D structures in hydrogels at single-cell resolution. The linear relation ( $R^2=0.9974$ ) between microwell radius and photomask pattern radius presented in **Rebuttal Figure 15E** indicates that microwell radius can be easily predicted from this calibration curve.

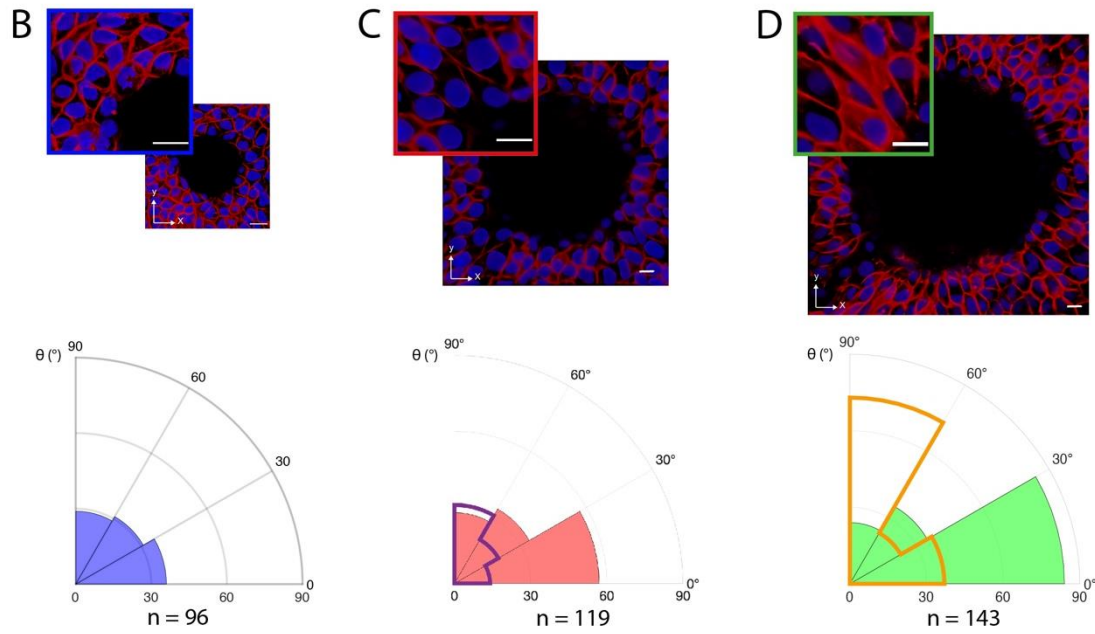


**Rebuttal Figure 15** – (E) The microwell radius ( $xy$ ) is linearly related to the radius of the circular patterns on the photomask ( $R^2=0.9974$ ). (F) Microwell depth ( $xz$ ) as a function of the photomask feature radius with radius of 25  $\mu\text{m}$  in purple, 50  $\mu\text{m}$  in blue, 100  $\mu\text{m}$  in red and 150  $\mu\text{m}$  in green. (G) Microwell radius as a function of the microwell depth.

In addition, these new results confirmed that the evolution of the microwell radius as a function of its depth is not linear (**Rebuttal Figure 15G**). These results were obtained by keeping constant the volume of the polyacrylamide droplet ( $V=50$   $\mu\text{L}$ ) which is squeezed between the chromium photomask and an activated glass coverslip. We have shown in our response to comment #A1 that the aspect ratio of the 3D microwells can be tuned by changing the volume of the polyacrylamide droplet and adjusting the photoillumination time for large droplet volumes. Our results showed that the larger the volume of the polyacrylamide drop, the deeper the 3D microwell.

Based on these findings, we modulated the aspect ratio of 3D microwells of 65  $\mu\text{m}$  and 100 to reduce their depth by  $\sim 55\%$ . As shown in **Rebuttal Figure 16C-D**, our results indicated that reducing the microwell depth led to a drastic reorientation of the nuclei around the microwell edge that lose their centripetal orientation. These findings demonstrated that the nuclear orientation around the microwell entrance is not only determined by the in-plane curvature but rely also on the Gaussian curvature. Interestingly, we have also shown that the

nuclear orientation around the microwell edge relies on contractile actomyosin forces (**Fig. 5 in the revised manuscript**) and that the Gaussian curvature at the microwell entrance promotes the maturation of the supracellular actin cable architecture (**Fig. 3 and Supplementary Fig. 4 in the revised manuscript**). Altogether, our findings support the hypothesis that the contractile actomyosin ring may be involved in generating contractile forces that promote centripetal orientation of cells and nuclei at the microwell edge.



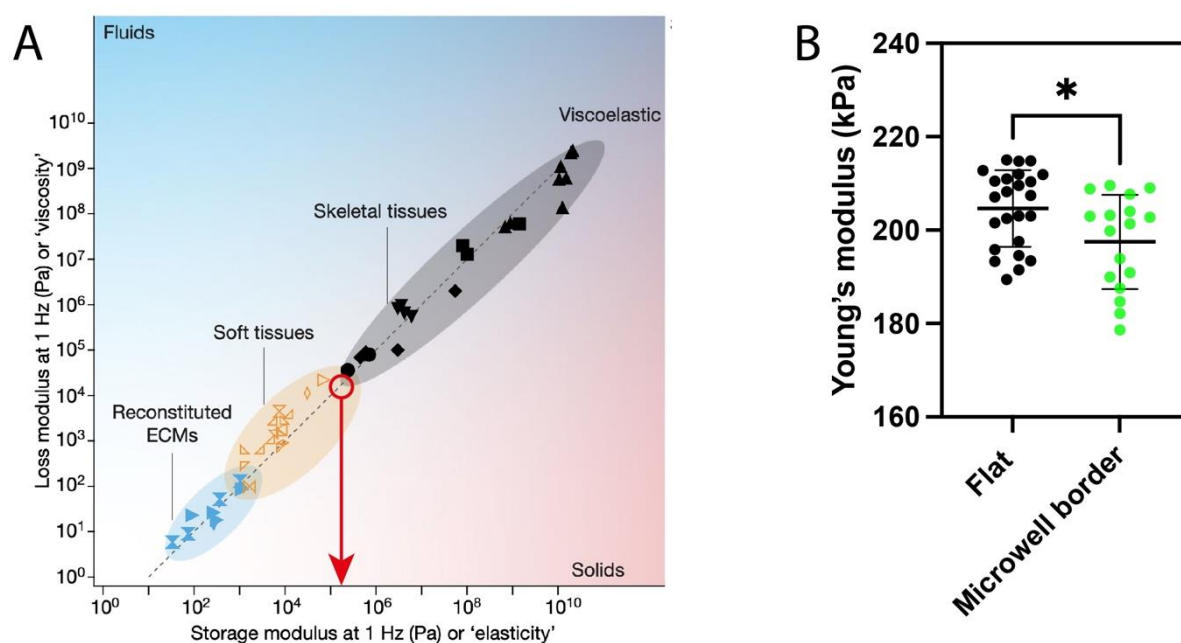
**Rebuttal Figure 16** – Top view ( $xy$ ) confocal images and corresponding nuclear orientations around the edge of microwells of (B) 30  $\mu\text{m}$  in radius ( $n=96$ , in blue), (C) 65  $\mu\text{m}$  in radius ( $n=119$ , in red) and (D) 100  $\mu\text{m}$  ( $n=143$ , in green) in radius. Cadherins are labeled in red and nuclei in blue. Scale bars are 20  $\mu\text{m}$ . Nuclear orientations superimposed in (C) with purple data and (D) with orange data correspond to microwells of (C) 65  $\mu\text{m}$  and (D) 100  $\mu\text{m}$  in radius with a lower depth, with (C)  $h=34\ \mu\text{m}$  (in orange) instead of 80  $\mu\text{m}$  (in red) and (D)  $h=42\ \mu\text{m}$  (in orange) instead of 91  $\mu\text{m}$  (in green).

**B3.** Additional data on the mechanics measurements are needed. How were these done in the microwells? Are the microwells mechanically uniform?

The bowl-shaped microwells used in this work must have a stiffness in agreement with the range of stiffnesses observed in soft tissues. Sneider et al. showed that the Young's modulus of breast tissues is dependent on its composition (Sneider A et al. Biomaterials 2022). Indeed, it exists a strong correlation between the amount of straight collagen and global breast stiffness, leading to cancer breast tissues with Young's moduli in the range of the hundreds of kPa. This range of stiffnesses were confirmed by Chaudhuri et al. by studying the viscoelastic properties of soft tissues (e.g. bladder, liver, lung, skin or kidney) that exhibit a stiffness between  $\sim 10^2$  and  $\sim 10^5$  Pa (see **Rebuttal Fig. 17A** and O. Chaudhuri et al. Nature 584, 535–546. 2020).

The stiffness of the microwells was determined with a nanoindentation technique (Chiaro, Optics 11) on immersed samples. We used a spherical probe with a radius of 9  $\mu\text{m}$  and

a stiffness of 0.49 N/m. The elastic modulus of flat and curved regions was determined by fitting force-indentation curves with the Hertz equation. As shown in the **Rebuttal Fig. 17B**, we obtained a mean elastic modulus of  $204.1 \pm 8.2$  kPa in flat zones ( $n=24$ ) around the microwell and  $197.5 \pm 10.1$  kPa at the Gaussian curvature zone ( $n=18$ ) of a microwell of 100  $\mu\text{m}$  in radius. The slightly lower stiffness values at the Gaussian curvature zone, which represent less than 3% of difference in terms of elasticity between both zones, could be attributed to the difficulty of maintaining good contact between the probe and the hydrogel in curved zones. It is very interesting to highlight that global stiffness of the 3D microwell is in good agreement with the range of elastic moduli observed in soft tissues (**Rebuttal Fig. 17A**).



**Rebuttal Figure 17** – (A) Linear evolution of the loss modulus as a function of the storage modulus for reconstituted extracellular matrices (in light blue), soft tissues (in light orange) and skeletal tissues (in light grey), giving approximately a  $\tan(\sigma)=0.1$ . Source: O. Chaudhuri et al. Nature 584, 535–546 (2020). (B) Young's modulus values obtained by nanoindentation on flat zones (black points,  $n=24$ ) and at the microwell entrance (green points,  $n=18$ ) of a microwell of 100  $\mu\text{m}$  in radius. A minimum of 3 replicates was used for each condition; \* $p < 0.05$ .

**B4.** Reliance of the current procedure for seeding the microwells with cells upon adsorbed fibronectin raises issues including uniformity of coating and wetting, and heterogeneous bioactivity and orientation that have been reported in previous adsorption of this matrix molecule to hydrogel surfaces. The images in S1B are not reassuring in this regard. An additional modality such as x-ray photoelectron spectroscopy would address this issue.

We used hydroxy-polyacrylamide (hydroxy-PAAm) hydrogels to form 3D microwells, enabling their surface to be functionalized with any ECM protein due to the presence of hydroxy groups. This hydrogel has been introduced by our group few years ago (T. Grevesse et al. Lab Chip 13, 777-780 2012, M. Versaevl et al. Methods in Cell Biology 121, 33-48 2014, T. Grevesse et al. JoVE 90, 51010 2014) and was patented (#WO2013174982 A1, 2012). Hydroxy-PAAm hydrogels were successfully used for studying different cell types such as

HUVECs (M. Versaevel et al Nature Communications 3, 1-11 2012), fish epithelial keratocytes (M. Riaz et al. Scientific Reports 6, 1-14 2016, E Vercruysse et al. bioRxiv 2022), cortical neurons (J. Lantoine et al. Biomaterials 89, 14-24 2016), C2C12 myoblasts (C. Bruyère et al. Scientific Reports 9, 1-14 2019) or recently MDCK epithelial cells (M. Versaevel et al. Scientific Reports 11, 1-11 2021) with various ECM proteins such as, laminin, collagen, fibronectin, vitronectin and poly-L-lysine.

The photoreticulation of hydroxy-PAAm hydrogels through an optical photomask was developed to create corrugated hydrogels with wavy profiles of different wavelengths and amplitudes (M. Luciano et al. Nature Physics 17, 1382-1390 2021). We demonstrated that these corrugated substrates were functionalized by a homogeneous layer of fibronectin, regardless the wavelengths (from 2 to 100  $\mu\text{m}$ ) and amplitudes (from  $\sim 0.2$  to  $\sim 20$   $\mu\text{m}$ ) of the sinusoidal profile. The surface of flat and microstructured hydroxy-PAAm hydrogels coated with ECM proteins such as fibronectin was characterized by spectroscopy techniques such as ATR-FTIR and we did not observe heterogeneous distribution of proteins. In addition, we observed a similar cellular density on flat and corrugated zones and no delamination of the epithelial tissue. In addition, we have shown that the epithelial monolayer remains very fluid and active, suggesting dynamic adhesive interactions with the microwell surface.

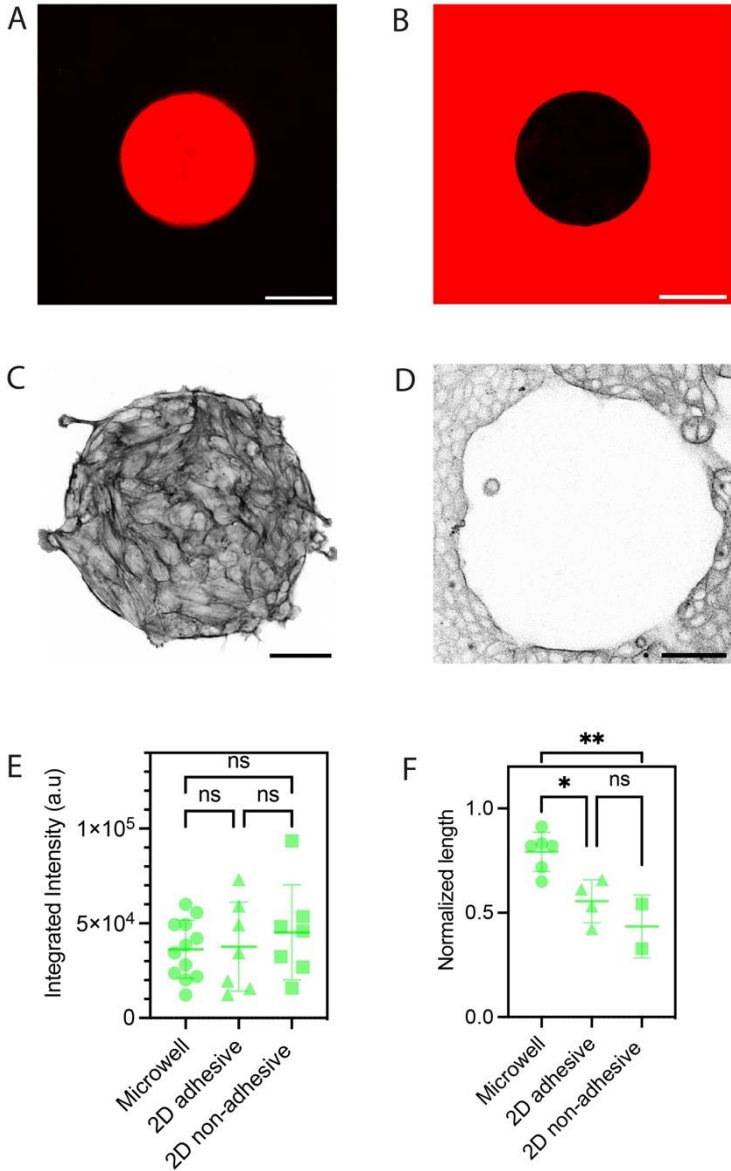
**B5.** Elucidation of molecular mechanisms that underlie the interesting differences between effects of 'in-plane' and 'out-of-plane' curvatures on the epithelial alignment and movement would be important additions to the presentation.

We appreciate the reviewer's advice to strengthen our manuscript. By using a MDCK cell line expressing red fluorescent E-cadherin at cell-cell contacts, we showed in **Fig. 3a of the revised manuscript** that epithelial cells around the microwell edge adopted a different orientation as a function of the microwell diameter. The cell angle ranged between  $0^\circ$ , corresponding to a long cell axis passing through the ( $xy$ ) center of the microwell, and  $90^\circ$  where the long cell axis was perpendicular to the line passing through the cell center of mass and ( $xy$ ) center of the microwell. Our results showed that the cell angle was larger for a small microwell radius ( $36.6 \pm 20.1^\circ$ ) than for a large microwell radius ( $12.7 \pm 8.9^\circ$ , **Fig. 3b of the revised manuscript**), indicating that the centripetal orientation of epithelial cells is enhanced at low in-plane curvature.

Our results indicated that actin accumulated at the microwell edge to form a well-defined supracellular cable-like structure, resembling a purse string and extending along the edge perimeter (**Fig. 3d and Supplementary Fig. 3 of the revised manuscript**). The quantification of the integrated intensity (**Fig. 3e**) and length (**Fig. 3f**) of this supracellular cable-like structure of actin in 30  $\mu\text{m}$ , 65  $\mu\text{m}$  and 100  $\mu\text{m}$  radius microwells indicated that supracellular cables were weaker and discontinuous at high in-plane curvatures, while low in-plane curvatures (100  $\mu\text{m}$  in radius) were characterized by thicker and continuous cable structures.

To decouple the role of in-plane and Gaussian curvatures in the formation of supracellular actin cables, we imposed similar in-plane curvatures to epithelial monolayers by using 2D circular adhesive (**Rebuttal Fig. 18a**) and non-adhesive (**Rebuttal Fig. 18b**)

micropatterns of 100  $\mu\text{m}$  in radius. As shown in **Rebuttal Fig. 18c-d**, we observed the formation of a supracellular actin cable on both conditions, which contain a similar amount of actin than observed in 3D microwells (**Rebuttal Fig. 4e**). Surprisingly, our findings showed that the normalized length of supracellular actin cables was significantly larger in 3D microwells than on adhesive and non-adhesive circular patterns (**Rebuttal Fig. 4f**). Altogether, our findings showed that the Gaussian curvature imposed at the microwell entrance by its 3D morphology promotes the maturation of the supracellular actin cable architecture.



**Rebuttal Figure 18 – Supracellular actin ring in 2D micropatterned epithelial monolayers.** 2D circular (A) adhesive and (B) non-adhesive fibronectin (in red) micropatterns of 100  $\mu\text{m}$  radius. The scale bars are 100  $\mu\text{m}$ . Representative image of the actin cytoskeleton of MDCK cells grown for 24 hours on 2D circular (C) adhesive and (D) non-adhesive fibronectin micropatterns. The scale bars are 50  $\mu\text{m}$ . (E) Integrated intensity and (F) normalized length of the actin ring in 3D microwell of 100  $\mu\text{m}$  in radius (circles), 2D adhesive circular patterns of

100  $\mu\text{m}$  in radius (triangles) and 2D non-adhesive circular patterns of 100  $\mu\text{m}$  in radius (squares).

In addition to these findings, we perturb the actomyosin contractility to determine its effect on nuclear organization by using Blebbistatin, which inhibits myosin ATPase activity and suppresses actomyosin contraction. The disruption of the actomyosin contractility with blebbistatin resulted in the collapse of the supracellular actin cable (**Fig. 5e-h** and **Supplementary Fig. 6 of the revised manuscript**) and in random nuclear orientations in both 65  $\mu\text{m}$  (**Fig. 5g**) and 100  $\mu\text{m}$  (**Fig. 5h**) microwells, which are similar to those observed in non-treated 30  $\mu\text{m}$  microwells (**Fig 5b**).

Altogether, our findings support the hypothesis that the contractile actomyosin ring may be involved in generating contractile forces that promote centripetal orientation of cells and nuclei at the microwell edge. Further experiments using laser ablation to dissect the actomyosin cytoskeleton with subcellular resolution will provide valuable insights into releasing the tension sustained by the supracellular actin cable and elucidating its specific role in cellular and nuclear orientation.

**B6.** The possible role of cell-matrix adhesion in determining cell behavior at the edges and interiors of the microwells should be considered.

As described in comment #B4, we observed a similar cellular density on flat and corrugated zones and no delamination of the epithelial tissue. In addition, we have shown that the epithelial monolayer remains very fluid and active, suggesting dynamic adhesive interactions with the microwell surface. However, we agree with the reviewer that it could be very interesting to further investigate the role of cell-matrix adhesions in the curve detection mechanism in future work, for example using different ECM protein coatings and specific integrin inhibitors. To this end, we already performed few preliminary experiments using CellLight Talin-GFP (BacMam 2.0) to label talin with green fluorescent proteins in live conditions. Indeed, it has been reported that talin is a key player of the molecular clutch process that can explain force transmission and transduction in response to matrix rigidity (Alberto Elosegui-Artola et al. Nature Cell Biology 2016 and Benjamin T. Goult et al. Journal of Cell Biology 2019). Our preliminary experiments are very promising but will require a great deal of efforts to establish a robust protocol and obtain a robust set of data. The potential role of cell-matrix adhesions in determining the curvresponse of epithelial cells is now discussed in the revised manuscript.

**B7.** Orientation of epithelia at the edges of contracting actomyosin rings is not altogether novel {Yang 2018; DOI: 10.1039/c7sm02521a}. The authors might consider a description of their work that points out the novelty of their findings more clearly. Additionally, an approach to ablating actomyosin contractility that is more spatially focused (eg. microinjection) would provide a more discerning way to measure the effects on the neighboring epithelial cells and nuclei.

We thank the Reviewer for highlighting the work of Yang and Levine in Soft Matter 2018 on the role of supracellular actin cables in epithelial tissues. This work was performed on

bidimensional epithelial tissues which were closing an open gap. Altogether these works demonstrated the pivotal role of supracellular actin cables in the wound healing process, with the generation of patterns of traction force pointing towards the wound and induced by the purse-string contraction (Yang and Levine Soft Matter 2018).

Our work shows the presence of a supracellular actin cable within a curved and confluent epithelial monolayer, which is totally new and has never been reported in the literature to our knowledge. Our work does not investigate the role of supracellular actin cables in flat epithelial monolayers that close a wound, but aims to understand how modulation of the matrix curvature in lobular structures can lead to the formation of a supracellular actin cable within a confluent epithelial monolayer.

By varying the microwell diameter and using 2D adhesive micropattern, we show that increasing the microwell diameter promotes the formation of a supracellular actin cable at the microwell edge. In addition, our findings indicate that the Gaussian curvature at the microwell entrance promotes the maturation of the supracellular actin cable architecture. The disruption of the actomyosin contractility with blebbistatin resulted in the collapse of the supracellular actin cable (**Fig. 5f-h and Supplementary Fig. 6**) and in random nuclear orientations in both 65  $\mu\text{m}$  (**Fig. 5f**) and 100  $\mu\text{m}$  (**Fig. 5h**) microwells, which are similar to those observed in non-treated 30  $\mu\text{m}$  microwells (**Fig 5b**).

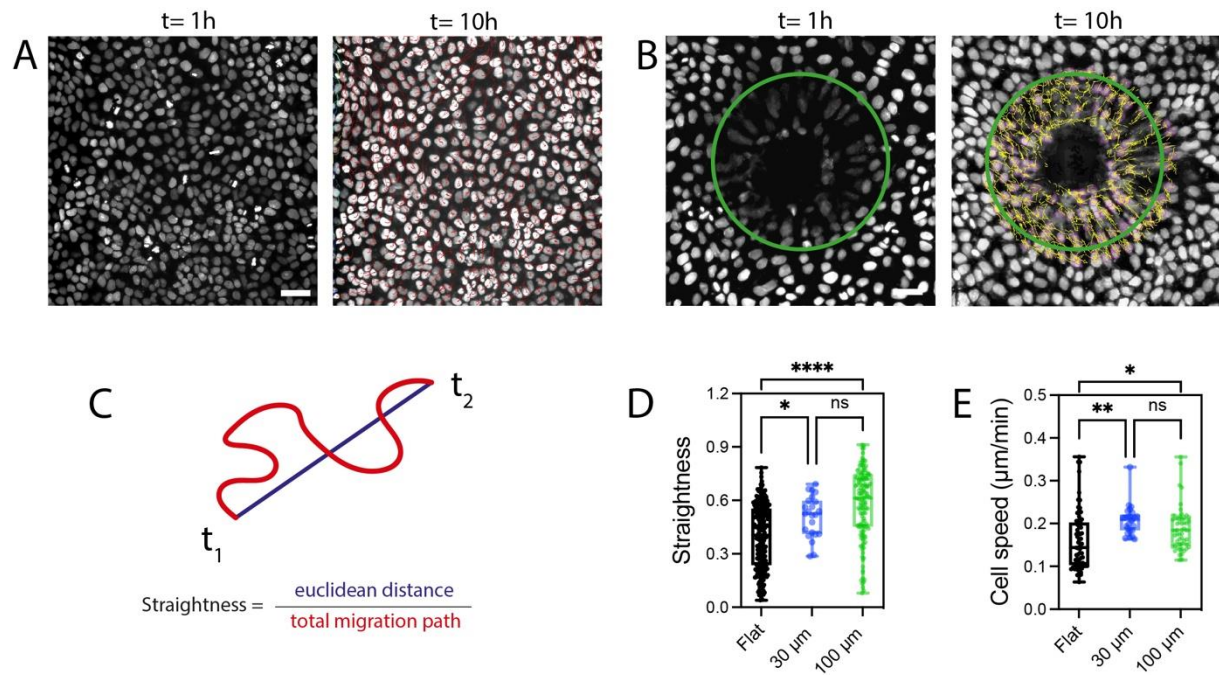
In addition to these results, we agree that ablating actomyosin contractility in a more spatially targeted manner provide a better understanding of the role of the supracellular actin cable. We carried out laser ablation experiments to disrupt supracellular actin cables, but our experiments were not successful due to the difficulty of targeting them without affecting neighbouring cells.

**B8.** Inclusion of a range of convex curvatures at the microwell entrances in the cell motility experiments would provide more insights into the nature of this relationship.

We have performed new time-lapse experiments on microwells of 30  $\mu\text{m}$  in diameter to provide additional results on the straightness and cell speed around microwell edges (**Rebuttal Figure 19**). Our results showed that cell straightness and speed were enhanced at the edge of microwells of 30  $\mu\text{m}$  (n=34) and 100  $\mu\text{m}$  (n=137) compared with controls (flat zones, n=253). We found a mean cell velocity of  $0.15\pm 0.07$   $\mu\text{m}/\text{min}$  for flat zones,  $0.19\pm 0.05$   $\mu\text{m}/\text{min}$  for microwells of 30  $\mu\text{m}$  and  $0.21\pm 0.03$   $\mu\text{m}/\text{min}$  for microwells of 100  $\mu\text{m}$  in radius (**Rebuttal Figure 19E**).

Interestingly, statistical analysis showed that differences in between cell speed between microwells of 30  $\mu\text{m}$  and 100  $\mu\text{m}$  with controls (flat zones) were statistically different. However, our findings showed no significant differences in straightness or migration speed between microwells of 30  $\mu\text{m}$  and 100  $\mu\text{m}$ . Altogether these results showed that cellular trafficking is enhanced at the microwell entrance but did not demonstrate a direct link between speed increase and curvature value.





**Rebuttal Figure 19 – Convex curvature at the microwell entrance enhances collective migration straightness and speed.** Time-lapse sequence in epifluorescent mode of the cumulative trajectories over 10 hours of individual cells within a confluent epithelial tissue on (A) a flat zone and (B) around the edge of a 3D microwell of 30 and 100  $\mu\text{m}$  in radius. Scale bars represent 50  $\mu\text{m}$ . The green circle delimits the zone around the microwell edge. (C) Schematic representation of the straightness parameter, defined by the ratio between the Euclidean distance and the total migration path. Cell (D) straightness and (E) speed within a confluent epithelial tissue on a flat zone (in black,  $n=253$ ) and around the edge of a 3D microwell of 30  $\mu\text{m}$  in radius (in blue) and 100  $\mu\text{m}$  in radius (in green,  $n=137$ ) with  $*p < 0.05$  and  $****p < 0.0001$ .

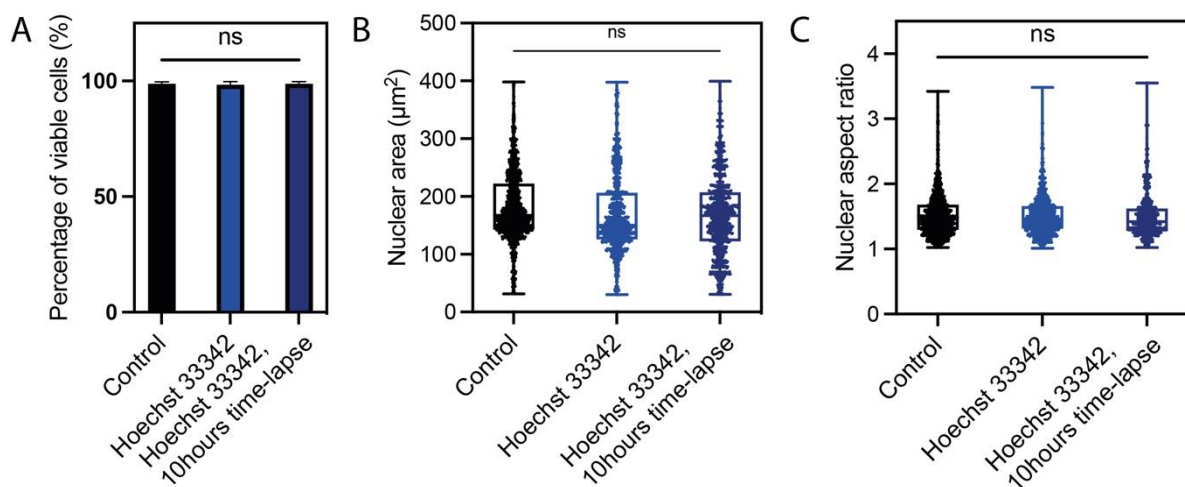
**B9.** Hoechst's 33342 has been shown to have concentration-dependent effects on nuclear and cell viability. Dose-response curves should be shown with regard to nuclear deformability in a separate assay. The concentration of this reagent that was used in the reported experiments needs to be provided.

The potential phototoxicity of Hoechst 33342 in time-lapse fluorescence microscopy is very important, especially for long time-lapse assays. Although toxicity of Hoechst 33342 is evident at long times in the absence of imaging at high dye concentrations, phototoxicity from repeated excitation of the dye in the imaging process is more complex to determine and relies on the cell type and the optical settings. Interestingly, it was shown that phototoxicity is a function of the product of light fluence and dye concentration but irrespective of irradiance, frequency and total number of scans (M. Pursche et al. Photochemical and Photobiological Sciences 2010). In addition, several works have reported that the cell type must be also considered as an important parameter.

We apologize for not having mentioned the concentration of Hoechst 33342 in our manuscript. MDCK cells were incubated with 0.1  $\mu\text{g/ml}$  of Hoechst 33342 at 37°C for 15 minutes and then cells were rinsed 3 times with sterile PBS at 37°C. We studied the phototoxicity of Hoechst 33342, by carrying out specific experiments to determine the

percentage of cell viability, the nuclear area and the nuclear aspect ratio (i) in control experiments, (ii) after 24 hours in culture with 0.1  $\mu\text{g/ml}$  of Hoechst 33342 and (iii) after 24 hours in culture with 0.1  $\mu\text{g/ml}$  of Hoechst 33342 followed by 10 hours of light exposure during a conventional time-lapse experiment. Control experiments correspond to MDCK cells with no Hoechst staining and no light exposure. The cell density was similar in all conditions and cell viability was assessed with a Sytox Green/ resazurin assay (Invitrogen).

Our results showed that incubating MDCK cells with 0.1  $\mu\text{g/ml}$  of Hoechst 33342 and performing 10 hours of time-lapse imaging does not affect their viability (**Rebuttal Fig. 20A**), nuclear area (**Rebuttal Fig. 20B**) and nuclear aspect ratio (**Rebuttal Fig. 20C**), suggesting that our experimental conditions prevent phototoxicity of Hoechst 33342 in time-lapse fluorescent assays of MDCK cells.

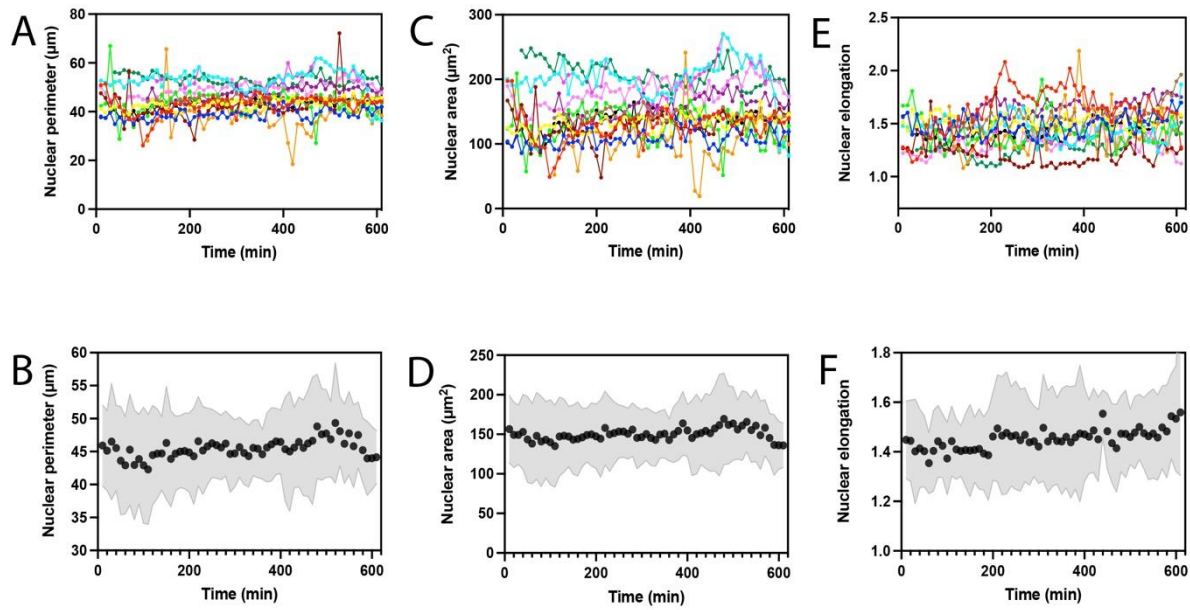


**Rebuttal Figure 20:** (A) Cell viability, (B) nuclear area and (C) nuclear aspect ratio in control experiments (in black), after 24 hours in culture with 0.1  $\mu\text{g/ml}$  of Hoechst 33342 (in blue) and after 24 hours in culture with 0.1  $\mu\text{g/ml}$  of Hoechst 33342 followed by 10 hours of light exposure during a conventional time-lapse experiment (in dark blue).

**B10.** Data on nuclear elongation would be more convincing in a dynamic format featuring live cell imaging.

We agree with the Reviewer that it would be more compelling to combine robust data from immunostained experiments with a dynamic visualization of nuclear elongations. To this end, we performed additional time-lapse experiments on Hoechst-stained cells stained to track the nucleus for 10 hours. We focused on cells migrating from the flat zone around the microwell edge to the Gaussian curvature zone, progressing therefore from the outer edge to the inner regions. We measured the perimeter (**Rebuttal Figure 21A**), surface area (**Rebuttal Figure 21C**) and elongation (**Rebuttal Figure 21E**) of each nucleus ( $n=13$ ) every 10 minutes for 600 minutes. By fitting an ellipse on each nucleus, we determined nuclear elongation as the ratio of the long to the short axis of the ellipse. Our results did not show significant changes of nuclear perimeter (**Rebuttal Figure 21B**) nor surface area (**Rebuttal Figure 21D**) over time, but we observed a slight increase of the mean aspect ratio from 1.41 to 1.57.

These results suggest that nuclei underwent deformation when cells migrated from the outer edge to the inner regions, which was then confirmed in **Fig. 6** by characterizing the 3D nuclear elongation at the Gaussian curvature zone on confocal images of immunostained cells. Indeed, we showed that higher Gaussian curvatures resulted in more flattened and elongated nuclei (**Fig. 6D-E**). The **Rebuttal Figure 21E-F** is now presented as **Supplementary Fig. 5** in the revised manuscript.

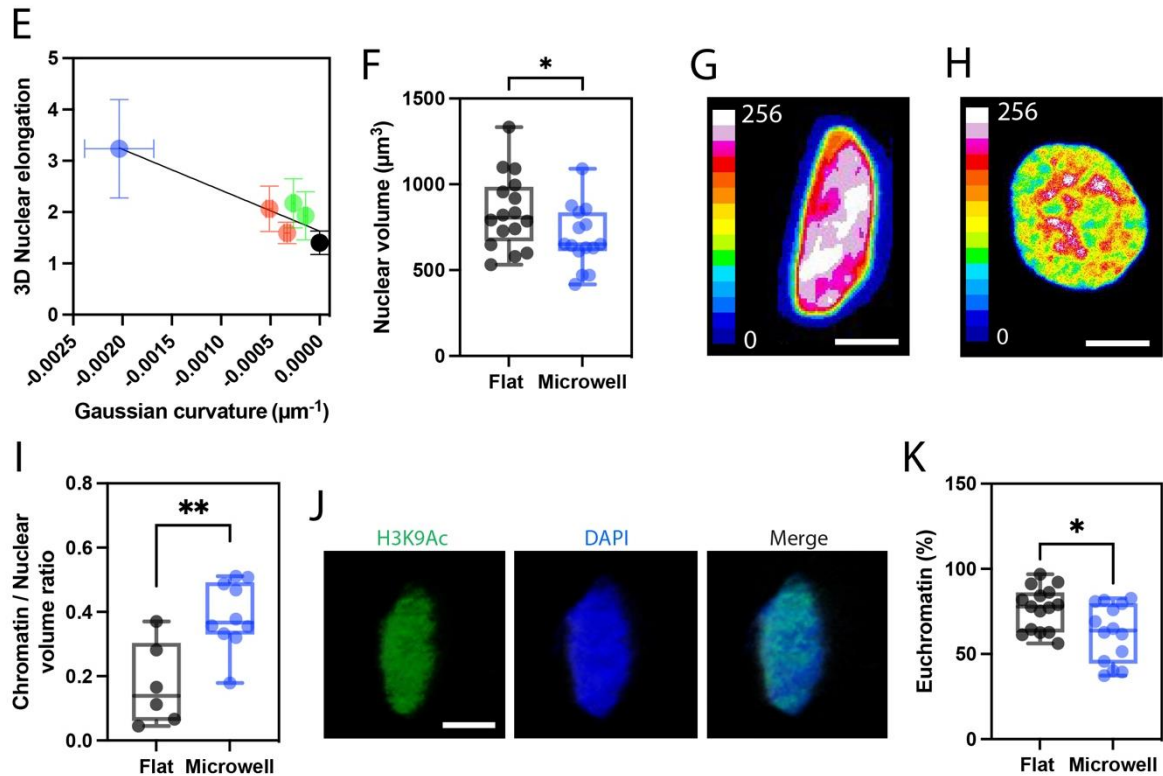


**Rebuttal Figure 21 – Dynamic characterization of the nuclear morphology in migrating cells.** Temporal evolution of (A-B) perimeter, (C-D) surface area and (E-F) elongation of individual nuclei ( $n=13$ ) migrating from the outer edge ( $t=0$ ) to the inner zone ( $t=600$  min.) of a 3D microwell of 100  $\mu\text{m}$  in radius. Means of nuclear perimeter, surface area and elongation are represented by black dots in B, D and F, respectively. Standard deviations are represented in light grey around the mean.

**B11.** The authors need to define and reference their approach to quantitative measurement of chromatin compaction.

Firstly, we used quantitative procedures based on DAPI staining and 3D confocal imaging at high magnifications (M. Versaevel et al Nature Communications 3, 1-11 2012 and M. Luciano et al. Nature Physics 17, 1382-1390 2021) to determine the average spatial density of chromatin, which is a reliable indicator of chromatin condensation. Our results demonstrated that elongated nuclei localized at the maximal Gaussian curvature zone exhibited higher levels of fluorescence intensity (**Rebuttal Figure 22G**) compared to rounded nuclei in flat zones (**Rebuttal Figure 22H**). Furthermore, our findings revealed higher chromatin compaction values in Gaussian curvature zones ( $0.39 \pm 0.11$ , **Rebuttal Figure 22I**) than in flat ones ( $0.17 \pm 0.13$ ). These results suggest that the Gaussian curvature imposed at the microwell entrance leads to a nuclear elongation, which is accompanied by higher levels of chromatin condensation.

To confirm these results, we characterized the level of histone H3 acetylation at lysine 9 (H3K9ac) by immunostaining to determine the level of euchromatin histone marks, which correspond to the loosely packed chromatin domain that is transcriptionally accessible (Y. Kalukula et al. Nat Rev Mol cell Biol 2022). Interestingly, elongated nuclei located at Gaussian curvature zones exhibited a lower volume (**Rebuttal Figure 22F**), a higher compacted chromatin state (**Rebuttal Figure 22G-I**) and a lower percentage of euchromatin (**Rebuttal Figure 22J-K**).



**Rebuttal Figure 22** – (E) 3D nuclear elongations were both linearly related with the Gaussian curvature, with  $R^2=0.8413$  and  $R^2=0.8616$ , respectively. Data in black correspond to the nuclear elongation on flat zones. Nuclear volume of cells located in flat (in black) and Gaussian (in blue) curvature zones. Typical images of the chromatin condensation obtained from a Z-projection for nuclei localized in (G) maximal curvature zones and (H) flat zones of a microwell of  $30\ \mu\text{m}$  in radius. Intensities of DNA staining were digitized in 256 bits and color coded for each Z-stack. Highly condensed domains show higher fluorescence intensity (white zones) with respect to the less condensed ones (blue zones). (I) Chromatin to nuclear volume ratio for nuclei localized on flat (in black) and Gaussian (in blue) curvature zones. (J) Representative confocal images of an elongated nuclei in a Gaussian curvature zone stained for H3K9Ac (in green) and DAPI (in blue). (K) Percentage of heterochromatin in nuclei localized on flat (in black) and Gaussian (in blue) curvature zones. \* $p < 0.05$  and \*\* $p < 0.0025$ .

Additional minor issues include the following:

**B12.** How was nuclear volume measured?

The nuclear volume was measured on 3D confocal images acquired with high-resolution (x40 or x100 silicon) objectives on a Nikon A1R laser-scanning microscope (Nikon, Japan) with Z increments of 0.125  $\mu\text{m}$ . Confocal images were deconvolved using a precalculated point spread function (PSF), after which cell boundaries were determined using Otsu's method. Voxels within the nuclear boundary of each stack were determined using the Voxel counter plugin in ImageJ and included in the calculation of the nuclear volume. The method section of the manuscript has been revised to include all technical details of this procedure.

**B13.** Are the scale bars for Figure 1 are all 20 microns in length?

Only scale bars in Fig. 1H-J are 20 microns, while scale bars are 50 microns in Fig. 1C and 500 microns in Fig. 1D. The previous legend, which could have led to confusion, has been revised.

**B14.** Please add to Figure 3c "the line passing through the cell center of mass".

This has been corrected.

**B15.** A thorough proofreading of the manuscript is needed to address spelling, grammar and diction.

The manuscript has been thoroughly revised and a proofread to improve its quality. We hope that these changes will improve the readability and fluidity of our manuscript.

---

### Response to Reviewer #3

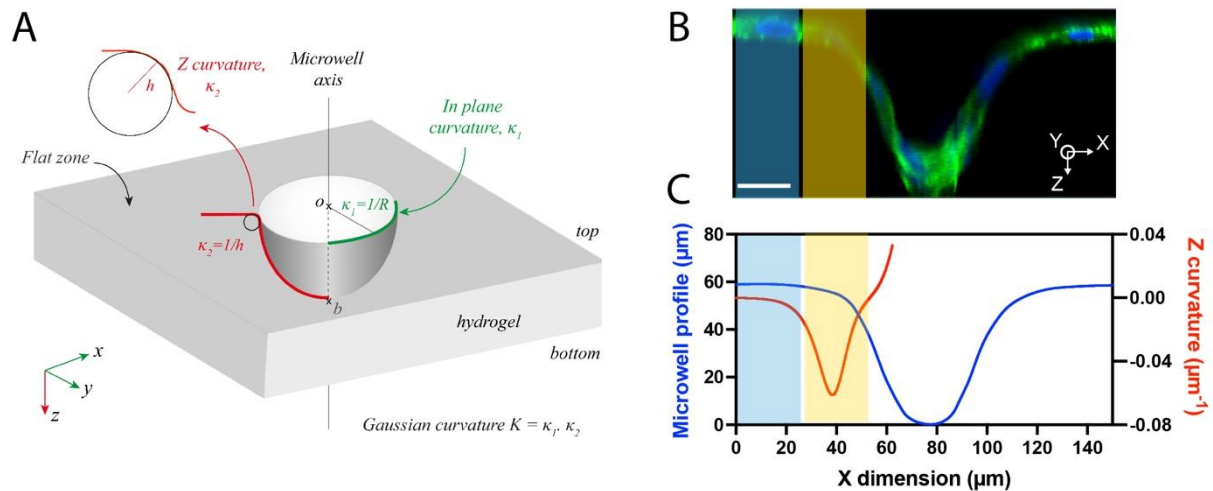
---

The manuscripts report a detailed experimental investigation of the effect of substrate curvature on the mechanoreponse of epithelial tissues, as well as the regulation of architecture and dynamics of collective epithelial assemblies. For this purpose, microwells of various diameters in hydrogels are constructed to induce the formation of curved epithelial structures. The main observations are: (i) Curvature governed by the microwell radius drives the centripetal orientation of cells and nuclei close to the edge of the microwell. (ii) Convex curvature imposed at the microwell entrance leads to a vertical orientation of the nuclei towards the microwell axis. (iii) Epithelial cells exhibit higher directionality and speed around the microwell edge. The effect of substrate curvature on the organization and structure of epithelial cell layers is an interesting and important topic. The current study makes a relevant contribution to the progress in this field.

**C1.** I find the use of the terms "in-plane curvature" and "out-of-plane curvature" in title, abstr radius and negative Gaussian curvature at the microwell entrance instead

We have revised our definition of the different curvatures as well as the different zones studied. Microwells exhibited a combination of an in-plane ( $xy$ ) curvature,  $k_1$ , determined by the radius,

R, as  $k_1=1/R$ , with an out-of-plane ( $xz$ ), or Z curvature,  $k_2$  localized at the microwell entrance and determined as  $k_2=1/h$ , with  $h$  the microwell depth (**Rebuttal Fig. 23A**). The product of the two principal curvatures  $k_1$  and  $k_2$  at the microwell entrance defines the microwell Gaussian curvature, such as:  $K = k_1 \times k_2$  (**Rebuttal Fig. 23A**). We can therefore define a flat zone around the microwell (light blue box in **Rebuttal Fig. 23B**) and a Gaussian curvature zone at the microwell entrance (light yellow box in **Rebuttal Fig. 23C**). Changes presented in the **Rebuttal Fig. 23** have been incorporated in the **Fig. 2A-C** of the revised manuscript.



**Rebuttal Figure 23 – Gaussian curvatures at the entrance of 3D synthetic microwells.** (A) Bowl-shaped 3D microwells were characterized by a combination of an in-plane ( $xy$ , in green) curvature,  $k_1$ , determined by the microwell radius,  $R$ , as  $k_1=1/R$ , with a Z ( $xz$ , in red) curvature  $k_2$  localized at the microwell entrance and determined as  $k_2=1/h$ , with  $h$  the microwell depth. A flat hydrogel zone surrounds each 3D microwell. The Gaussian curvature  $K$  at the microwell entrance corresponds to  $K = k_1 \times k_2$ . (B) Representative confocal profile of a microwell of  $30 \mu\text{m}$  in radius covered with a monolayer of epithelial cells stained for actin (in green) and DNA (in blue). (C) Profile of a microwell of  $30 \mu\text{m}$  in radius (in blue) and the corresponding Z curvature (in red) calculated at each point of the microwell profile. The light blue box on (B) and (C) represents the flat zone around the microwell, while the light-yellow box delimits the Gaussian curvature zone at the microwell entrance.

**C2.** The authors mention "positive curvature" and "bidimensional variation of substrate geometries". These terms need clarification?

In the previous version of the manuscript, this sentence described the work of Chen and coworkers in Nature Physics 2019 studying the role of concave and convex modulations of the leading edge of an epithelial monolayer on actin flow. In this work, positive curvatures refer to convex zones, while negative curvature refer to concave ones. The bidimensional variation of substrate geometries was related to the use of flower-shaped 2D micropatterns that imposed convex and concave adhesive zones on lamellipodial protrusions. This section has been rewritten in the revised manuscript as : « Using flower-shaped micropatterns, it has been shown that cells distinguish between zones of convex (i.e. positive) and concave (i.e. negative) curvatures in their 2D physical environment by forming actin retrograde flow in lamellipodial protrusions at positive curvature zones and contractile actin cables at negative ones <sup>[9]</sup>. These

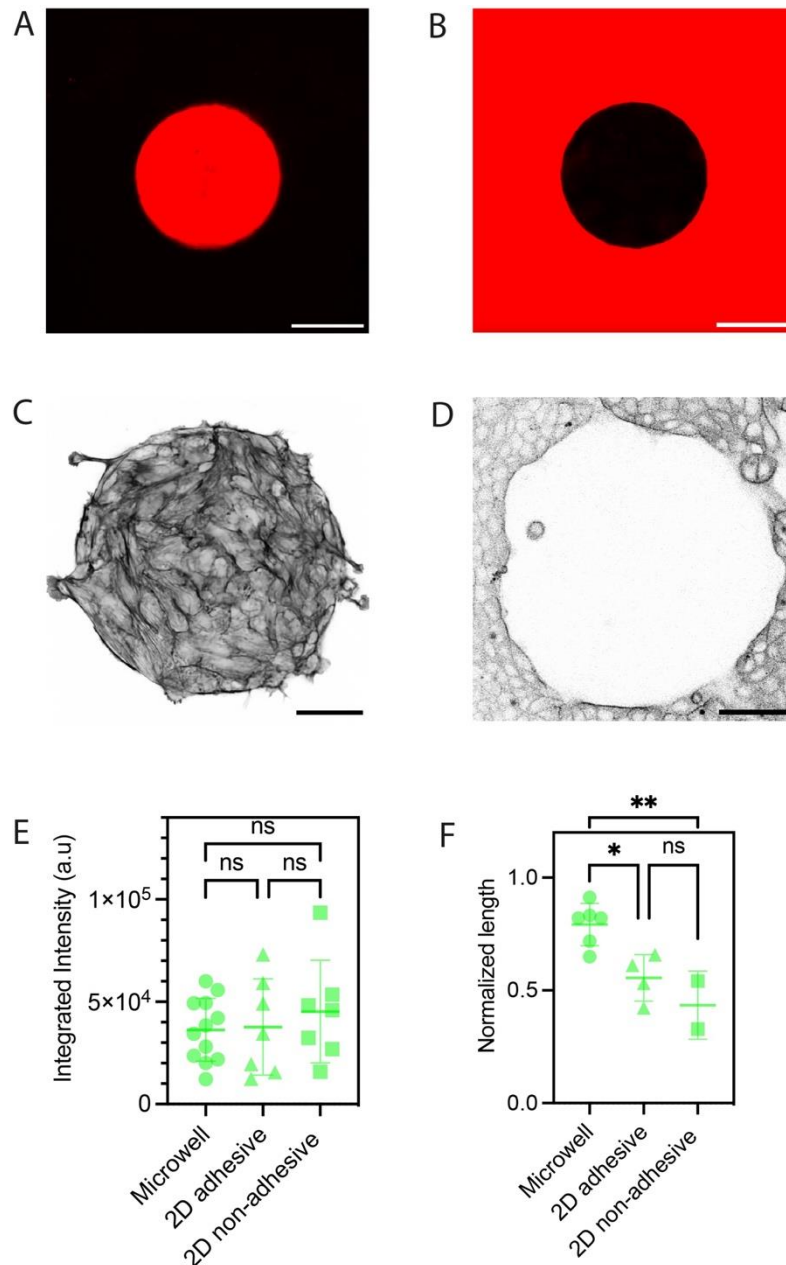
adaptive responses are believed to aid in sensing and navigating the cellular environment in response to geometric and mechanical cues. »

**C3.** What is a "three-dimensional (3D) substrate curvature"?

This term is no longer used in the manuscript and the definitions of curvature have been revised (see comment C1).

**C4.** The authors state (p.8) that "in-plane microwell curvature decreases and support the hypothesis that decreasing the in-plane microwell curvature promotes the formation of a contractile actomyosin ring that exerts centripetal forces on cells localized around the microwell edge". What happens in the limit of zero curvature ??? (FLAT PATTERNS)

We thank the Reviewer for this very interesting comment. We now provide new experiments using two-dimensional (2D) adhesive micropatterns of similar diameters (and consequently in-plane curvature) which are "flat patterns" (see Comment #A1). These 2D circular adhesive (**Rebuttal Fig. 24A**) and non-adhesive (**Rebuttal Fig. 24B**) micropatterns of 100  $\mu\text{m}$  in radius were used to impose similar in-plane curvatures to epithelial monolayers than those observed in 3D microwells. to change one variable (e.g. in plane curvature) without affecting all other variables to determine the role of the Gaussian curvature on the formation of supracellular actin rings. By using this strategy, we aimed to decouple the individual role of in-plane and Gaussian curvatures in the formation of supracellular actin cables by quantifying the amount of actin signal in a supracellular actin cables and their normalized length. As shown in **Rebuttal Fig. 24C-D**, we observed the formation of a supracellular actin cable on both conditions, which contain a similar amount of actin than observed in 3D microwells (**Rebuttal Fig. 24E**). Surprisingly, our findings showed that the length of supracellular actin cables normalized by the total perimeter was significantly larger in 3D microwells than on adhesive and non-adhesive circular patterns (**Rebuttal Fig. 24F**). Altogether, our findings showed that the Gaussian curvature imposed at the microwell entrance by its 3D morphology promotes the maturation of the supracellular actin cable architecture. The **Rebuttal Fig. 24** has been now added as **Supplementary Figure 4** in the revised manuscript. The legend and the method section have been modified accordingly.

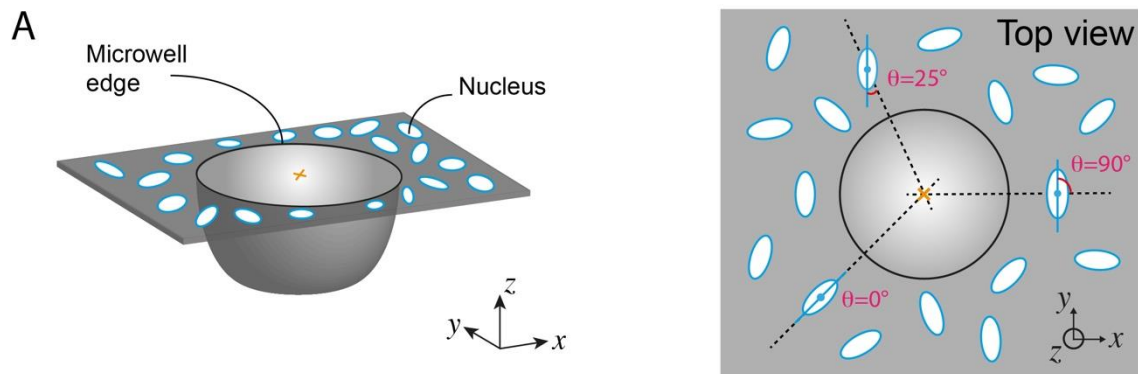


**Rebuttal Figure 24 – Supracellular actin ring in 2D micropatterned epithelial monolayers.** 2D circular (A) adhesive and (B) non-adhesive fibronectin (in red) micropatterns of 100  $\mu\text{m}$  radius. The scale bars are 100  $\mu\text{m}$ . Representative image of the actin cytoskeleton of MDCK cells grown for 24 hours on 2D circular (C) adhesive and (D) non-adhesive fibronectin micropatterns. The scale bars are 50  $\mu\text{m}$ . (E) Integrated intensity and (F) normalized length of the actin ring in 3D microwell of 100  $\mu\text{m}$  in radius (circles), 2D adhesive circular patterns of 100  $\mu\text{m}$  in radius (triangles) and 2D non-adhesive circular patterns of 100  $\mu\text{m}$  in radius (squares).

**C5.** "... nuclei ... mostly oriented towards the microwell axis." What does this mean?



We characterized the nuclear orientation around the edge of the microwell by determining the angle between the nuclear long axis and a line passing through the ( $xy$ ) center of the microwell and the center of mass of the nucleus (**Rebuttal Figure 25**). To this aim, the nuclear shape was assumed to be ellipsoidal. The **Rebuttal Figure 25** is now provided as **Fig. 5A in the revised manuscript**.



**Rebuttal Figure 25 – Nuclear orientations around the microwell edge.** Schematic representation of different scenarios of nuclear orientation around the microwell edge (black circle on the top view). The nuclear orientation was obtained by determining the angle (in red) between the nuclear long axis (blue line) and the dotted line passing through the ( $xy$ ) center of the microwell (orange cross) and the center of mass of the nucleus (blue dot). Angles ranged from  $\theta=0^\circ$  and  $\theta=90^\circ$  for nuclei parallel or perpendicular respectively to the dotted line passing through the ( $xy$ ) center of the microwell and their center of mass. An intermediate situation with  $\theta = 25^\circ$  is presented.  $\theta=0^\circ$  corresponds to a centripetal orientation of the nucleus.

**C6.** "convex out-of-plane curvature led to more flattened nuclei, in agreement with previous observations ... [20]." This concerns a previous study by the authors. Has a similar behavior observed by other groups?

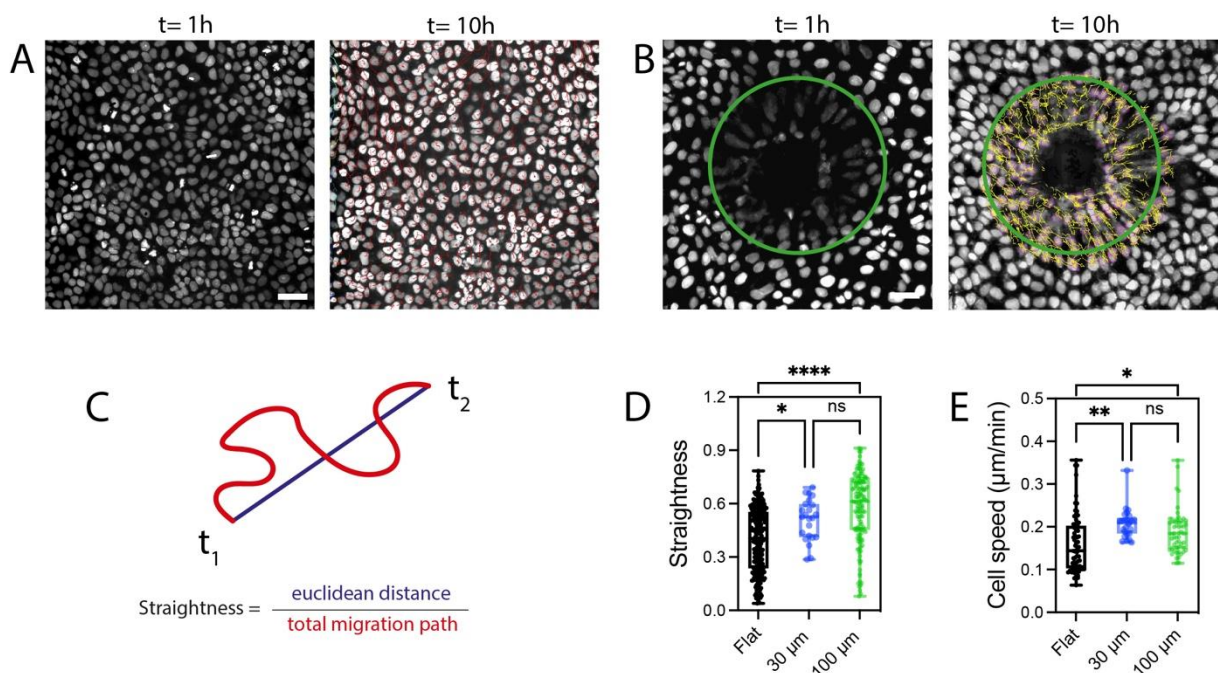
To our knowledge, only very few works studied the mechanical deformation of the nucleus in response to changes of matrix curvature. Interestingly, Werner and coworkers (M. Werner et al. *Advanced Science* 2016 <https://doi.org/10.1002/advs.201600347>) have also reported nuclear deformations in human mesenchymal stem cells (hMSCs) plated on convex spherical surfaces (see Figs. 5 and 6). The authors showed that nuclear deformations are a consequence of a substantial increase in cytoskeletal forces convex spherical surfaces, which can promote osteogenic differentiation in hMSCs. However, this work was performed on single cells only and did not characterize the effect of the curvature on chromatin compaction. The work of Werner and coworkers was already cited in our manuscript, but we have revised the section on nuclear deformations to cite it more specifically.

**C7.** Text at top of p.10 is a summary. Why part of Sec. 2.6 "collective migration"?

The architecture of the manuscript has been revised, the text has been rewritten and the section on collective migration has been moved. We hope that these changes will improve the readability and fluidity of our manuscript.

**C8.** Fig. 6: Is the increase of cell speed significant?

We have performed new time-lapse experiments on microwells of 30  $\mu\text{m}$  in diameter to provide additional results on the straightness and cell speed around microwell edges (**Rebuttal Figure 26**). We found that cell straightness and speed were enhanced at the edge of microwells of 30  $\mu\text{m}$  (n=34) and 100  $\mu\text{m}$  (n=137) compared with controls (flat zones, n=253). We found a mean cell velocity of  $0.15 \pm 0.07 \mu\text{m}/\text{min}$  for flat zones,  $0.19 \pm 0.05 \mu\text{m}/\text{min}$  for microwells of 30  $\mu\text{m}$  and  $0.21 \pm 0.03 \mu\text{m}/\text{min}$  for microwells of 100  $\mu\text{m}$  in radius (**Rebuttal Figure 26E**). Furthermore, statistical analysis showed that differences between cell speed on microwells of 30  $\mu\text{m}$  and 100  $\mu\text{m}$  with those on controls (flat zones) were statistically different.



**Rebuttal Figure 26 – Convex curvature at the microwell entrance enhances collective migration straightness and speed.** Time-lapse sequence in epifluorescent mode of the cumulative trajectories over 10 hours of individual cells within a confluent epithelial tissue on (A) a flat zone and (B) around the edge of a 3D microwell of 30 and 100  $\mu\text{m}$  in radius. Scale bars represent 50  $\mu\text{m}$ . The green circle delimits the zone around the microwell edge. (C) Schematic representation of the straightness parameter, defined by the ratio between the Euclidean distance and the total migration path. Cell (D) straightness and (E) speed within a confluent epithelial tissue on a flat zone (in black, n=253) and around the edge of a 3D microwell of 30  $\mu\text{m}$  in radius (in blue) and 100  $\mu\text{m}$  in radius (in green, n=137) with \* $p < 0.05$  and \*\*\*\* $p < 0.0001$ .

**C9.** Sec. 3 is not really about "conclusions", but again mainly a summary. Should be combined with text at top of p.10.

We thank the reviewer for helping us improve the manuscript. In accordance with the guidelines provided by the Wiley for Advanced Healthcare journal, the conclusion section has been removed and the discussion has been rewritten. For instance, we now discuss the recent

example of elongated keratinocytes forming an actin rim to exert contractile forces around the mammary bud, resulting in a process of invagination<sup>[40]</sup>. We also extend this section by discussing the need for cutting-edge techniques, such as laser ablation to dissect the actomyosin cytoskeleton<sup>[36]</sup> or computational methods to map the internal stress in curved epithelial<sup>[41]</sup>, that could offer valuable insights to quantify the tension sustained by supracellular actin cables and unravel their specific roles in maintaining lobular structure homeostasis. We hope these modifications will improve the clarity of the discussion.

# Mechanoresponse of curved epithelial monolayers lining bowl-shaped 3D microwells

Marine Luciano<sup>#1</sup>, Marie Versaevel<sup>#1</sup>, Yohalie Kalukula<sup>1</sup> and Sylvain Gabriele<sup>1\*</sup>

<sup>1</sup> Mechanobiology & Biomaterials group, Interfaces and Complex Fluids Laboratory,  
Research Institute for Biosciences, CIRMAP, University of Mons, Place du Parc, 20 B-7000  
Mons, Belgium

<sup>#</sup>Contributed equally to this work

\*To whom correspondence should be addressed: [sylvain.gabriele@umons.ac.be](mailto:sylvain.gabriele@umons.ac.be)

The optimal functioning of many organs relies on the curved architecture of their epithelial tissues. However, the mechanoresponse of epithelia to changes in curvature remains misunderstood. Here, we designed bowl-shaped microwells in hydrogels via photopolymerization to faithfully replicate the shape and dimensions of lobular structures. Leveraging these hydrogel-based microwells, we engineered curved epithelial monolayers and investigated how in-plane and Gaussian curvatures at the microwell entrance influence epithelial behavior. Cells and nuclei around the microwell edge displayed a more pronounced centripetal orientation as the in-plane curvature decreases, and enhanced cell straightness and speed. Moreover, cells reorganized their actin cytoskeleton by forming a supracellular actin cable at the microwell edge, with its size becoming more pronounced as the in-plane curvature decreased. The Gaussian curvature at the microwell entrance enhanced the maturation of the supracellular actin cable architecture and led to a vertical orientation of nuclei towards the bottom of the microwell. Increasing Gaussian curvature resulted in flattened and elongated

1 nuclear morphologies characterized by highly compacted chromatin states. Our approach  
2 provides a better understanding of the mechanoresponse of curved epithelial monolayers  
3 curvatures lining lobular structures. Additionally, bowl-shaped microwells offer a powerful  
4 platform to study curvature-dependent mechanotransduction pathways in anatomically relevant  
5 3D structures.  
6  
7  
8  
9  
10

## 11 **1. Introduction**

12  
13  
14  
15  
16  
17  
18  
19 Accumulative research provide compelling evidence concerning the remarkable capacity of  
20 cells to perceive and react to changes in the physico-chemical properties of their extracellular  
21 matrix (ECM) <sup>[1]</sup>. Indeed, cells reside in a complex native microenvironment that guides and  
22 regulates their functions <sup>[2]</sup>. Notably, extensive studies have demonstrated that the mechanical  
23 stiffness of the cellular microenvironment profoundly influences cell migration <sup>[3]</sup>, stem cell  
24 differentiation <sup>[4]</sup> and even impact tissue regeneration <sup>[5]</sup>. More recently, mounting evidence  
25 suggests that the geometrical properties of the cell's microenvironment also play a pivotal role  
26 in governing cellular functions. For example, the unique architecture of the intestinal crypt-  
27 villus system, where dividing stem cells exclusively occupy the concave zones, exemplifies the  
28 influence of curvature <sup>[6]</sup>.  
29  
30  
31  
32  
33  
34  
35  
36  
37  
38  
39  
40  
41  
42

43  
44 Previous studies have highlighted the impact of two-dimensional (2D) variations in  
45 substrate geometries on the spatial organization of stress fibers and focal adhesions, influencing  
46 internal forces exerted by the actin cytoskeleton on the nucleus <sup>[7]</sup>. Notably, cells on adhesive  
47 islands with constant area but different geometries displayed distinct differentiation profiles,  
48 with high aspect-ratio micropatterns and high subcellular curvature promoting increased  
49 cellular contractility and osteogenic differentiation <sup>[8]</sup>. Using flower-shaped micropatterns, it  
50 has been shown that cells distinguish between zones of convex (i.e. positive) and concave (i.e.  
51  
52  
53  
54  
55  
56  
57  
58  
59  
60  
61  
62  
63  
64  
65

1 negative) curvatures in their 2D physical environment by forming actin retrograde flow in  
2 lamellipodial protrusions at positive curvature zones and contractile actin cables at negative  
3 ones <sup>[9]</sup>. These adaptive responses are believed to aid in sensing and navigating the cellular  
4 environment in response to geometric and mechanical cues.  
5  
6  
7  
8  
9

10 In addition to 2D curvature changes, increasing evidence suggests that three-  
11 dimensional (3D) substrate curvature plays a critical role in cellular organization <sup>[10]</sup>. Indeed,  
12 epithelial tissues, such as lung alveoli, kidney glomerulus, intestinal villi, and breast acini,  
13 exhibit complex morphologies dominated by curved surfaces <sup>[11]</sup>. Furthermore, tissue curvature  
14 and associated changes in apicobasal tension are fundamental determinants of epithelial  
15 tumorigenesis in pancreatic ducts and tubular epithelia of the liver and lung <sup>[12]</sup>. Studies using  
16 macroscale substrates with radii of curvature ranging from tens to hundreds of micrometers  
17 have observed that cell alignment and migration in response to 3D cell-scale curvature patterns  
18 is a complex process that relies on cell-cell interactions and depends on cell types. For instance,  
19 isolated vascular smooth muscle cells aligned more weakly than single fibroblasts on  
20 cylindrical substrates, whereas both cell types in confluent monolayers aligned prominently  
21 with respect to the cylinder axis <sup>[13]</sup>. Cells exhibit different morphologies on convex and  
22 concave surfaces to minimize the contact area on concave zones and compressive forces on the  
23 nucleus <sup>[14]</sup>. Cell migration speed of human mesenchymal stem cells (hMSCs) is significantly  
24 higher on concave spherical surfaces than on convex spherical surfaces, whereas substantial  
25 deformations occur on convex surfaces leading to an increase of lamin A expression in the  
26 nuclear envelope <sup>[15]</sup>.  
27  
28  
29  
30  
31  
32  
33  
34  
35  
36  
37  
38  
39  
40  
41  
42  
43  
44  
45  
46  
47  
48  
49  
50  
51

52 Although these studies have generated valuable findings on the curvature-sensitive  
53 cellular response, most of them have been conducted at the single-cell level and used rigid  
54 substrates with a non-physiological stiffness <sup>[13][14][16][17]</sup>. Recent works have addressed this  
55 issue by developing original physico-chemical strategies to pattern hydrogels with tunable  
56  
57  
58  
59  
60  
61  
62  
63  
64  
65

1 rigidities and 3D microstructures <sup>[18]</sup>. Endothelial cells, for instance, have demonstrated self-  
2 organization in response to combinatorial effects of stiffness and geometry, independent of  
3  
4 protein or chemical patterning <sup>[19]</sup>. Formation of well-defined corrugated hydrogels has revealed  
5  
6 that substrate curvature influences the thickness of epithelial monolayers, nuclear morphology,  
7  
8 and positioning <sup>[20]</sup>. Intriguingly, recent reports have described the spontaneous growth of 3D  
9  
10 epithelial cavitating spheres during the naive-to-primed transition of human pluripotent stem  
11  
12 cells (hPSCs), accurately modeling peri-implantation epiblast development <sup>[21]</sup>. These findings  
13  
14 collectively underscore the fundamental capacity of cells to respond to curvature-sensitive cues.  
15  
16

17  
18  
19 However, the impact of in-plane and Gaussian curvatures on multicellular organization  
20  
21 remains poorly understood due to the lack of engineering methods capable of mimicking  
22  
23 anatomically relevant 3D complex morphologies, such as those found in lobular structures  
24  
25 lining human organs. To address this gap, here we present a simple method for creating bowl-  
26  
27 shaped 3D microwells in hydrogels and engineering curved epithelial monolayers with  
28  
29 morphologies resembling those of epithelial tissues in lobular structures. Leveraging this  
30  
31 approach, we investigated the distinct roles of in-plane and Gaussian curvatures on the  
32  
33 mechanoresponse of curved epithelial monolayers.  
34  
35  
36  
37  
38  
39  
40  
41  
42

## 43 **2. Results and Discussion**

### 44 45 **2.1. Microfabrication of bowl-shaped 3D microwells in hydroxy-PAAm hydrogels by** 46 47 **photolithography** 48 49

50  
51 We designed curved epithelia with a controlled lobular morphology by photopolymerizing soft  
52  
53 hydroxy-polyacrylamide (hydroxy-PAAm) hydrogels <sup>[22]</sup> under UVA illumination from 315 to  
54  
55 400 nm with the photoinitiator Irgacure 2959, which generates ketyl radicals (**Fig. 1a**). We  
56  
57 achieved the formation of bowl-shaped 3D microwells in hydroxy-PAAm hydrogels by  
58  
59  
60  
61  
62  
63  
64  
65

1 illuminating the polymer solution through a transparent quartz optical photomask that contains  
2 dark circular chromium zones (**Fig. 1b**). As reported previously, hydroxyl groups allowed the  
3 hydrogel functionalization with fibronectin <sup>[20][22]</sup>, enabling the establishment of specific cell-  
4 substrate adhesions crucial for preventing the delamination of the epithelial monolayer on  
5 curved zones <sup>[20]</sup> (**Fig. 1c**). Photopolymerization through a transparent chromium optical  
6 photomask was employed to create a periodical organization of microwells of various diameters  
7 over large surface areas (10x10 mm<sup>2</sup>) (**Fig. 1d**). We maintained a spacing of 500 μm between  
8 adjacent microwells to minimize neighbour interactions and include flat zones as controls.  
9 Circular patterns of 25, 50, 100 and 150 μm in radius were used to form microwells of 20 ± 2  
10 μm, 30 ± 3 μm, 65 ± 8 μm and 100 ± 4 μm in radius, respectively (**Fig. 1e**). Our technique led  
11 to highly reproducible microwell morphologies (**Supplementary Fig. 1**). The depth of the  
12 microwell was determined through confocal microscopy (**Fig. 1f**), establishing the relationship  
13 between radius and depth of the microwells (**Fig. 1g**).

## 2.2. Gaussian curvature of microwells matches the curvature range in anatomical lobular structures.

34  
35  
36  
37  
38  
39  
40 Our results demonstrated the formation of uniform and cohesive monolayer of Madin-Darby  
41 canine kidney (MDCK) cells around and within microwells of varying radii of 30 μm (**Fig. 1h**,  
42 **Supplementary Movie S1**), 65 μm (**Fig. 1i**, **Supplementary Movie S2**) and 100 μm (**Fig. 1j**,  
43 **Supplementary Movie S3**) after 24 hours in culture. Microwells exhibited a combination of  
44 an in-plane ( $xy$ ) curvature,  $k_1$ , determined by their radius,  $R$ , as  $k_1=1/R$ , with an out-of-plane  
45 ( $xz$ ), or  $Z$  curvature,  $k_2$ , localized at the microwell entrance and determined as  $k_2=1/h$ , with  $h$   
46 the microwell depth (**Fig. 2a**). We used confocal microscopy (**Fig. 2b**) to obtain their ( $xz$ )  
47 profiles and to determine the  $Z$  curvature (**Fig. 2c**). The product of the two principal curvatures  
48  $k_1$  and  $k_2$  at the microwell entrance defines the microwell Gaussian curvature, such as:  $K = k_1 \times k_2$   
49  
50  
51  
52  
53  
54  
55  
56  
57  
58  
59  
60  
61  
62  
63  
64  
65



1  
2  
3  
4  
5  
6  
7  
8  
9  
10  
11  
12  
13  
14  
15  
16  
17  
18  
19  
20  
21  
22  
23  
24  
25  
26  
27  
28  
29  
30  
31  
32  
33  
34  
35  
36  
37  
38  
39  
40  
41  
42  
43  
44  
45  
46  
47  
48  
49  
50  
51  
52  
53  
54  
55  
56  
57  
58  
59  
60  
61  
62  
63  
64  
65

(**Fig. 2d**). We can therefore define a flat zone around the microwell (light blue box in **Fig. 2b-c**) and a Gaussian curvature zone at the microwell entrance (light yellow box in **Fig. 2b-c**). Our findings revealed that as the bowl-shaped microwell radius increased from 25 to 100  $\mu\text{m}$ , the Gaussian curvature at the microwell entrance decreased from approximately  $-10^{-2}$  to  $-10^{-3} \mu\text{m}^{-1}$  (**Fig. 2d**). Importantly, we demonstrated a strong correspondence between this range of Gaussian curvatures and the typical values of Gaussian curvature observed in anatomic lobular structures within the lung <sup>[23]</sup>, kidney <sup>[24]</sup>, breast <sup>[25]</sup>, and pancreas <sup>[12]</sup> (**Fig. 2e**). Our findings underscore therefore the clinical relevance of bowl-shaped microwells to investigate the mechanoresponse of curved epithelial monolayers that line lobular structures<sup>[26]</sup>.

We studied the mechanoresponse of epithelial cells across the two main regions (flat and Gaussian curvature zones) around the entrance of bowl-shaped 3D microwells (**Fig. 2b-c**), progressing from the outer edge to the inner regions (**Supplementary Fig. 2a**). Based on segmented images (**Supplementary Fig. 2b**), our results indicated that both zones exhibited similar cell density (**Supplementary Fig. 2c**) and comparable rates of division events (**Supplementary Fig. 2d**). The bottom part of the microwell has not been studied to avoid artifacts caused by imaging issues and potential modification of cellular density.

### 2.3. The centripetal orientation of cells around the microwell edge is enhanced at low in-plane curvature.

A closer look at the architecture of the epithelial monolayer indicated significant changes of cellular orientations around the microwell edge. To get further insight into this phenomenon, we used a MDCK cell line expressing red fluorescent E-cadherin at cell-cell contacts. As shown in **Fig. 3a**, epithelial cells around the microwell edge adopted a different orientation as a function of the microwell diameter. The cell angle ranged between  $0^\circ$ , corresponding to a long cell axis passing through the ( $xy$ ) center of the microwell, and  $90^\circ$  where the long cell axis was

1 perpendicular to the line passing through the cell center of mass and (xy) center of the  
2 microwell. Our results showed that the cell angle was larger for a small microwell radius  
3  
4 (36.6±20.1°) than for a large microwell radius (12.7±8.9°, **Fig. 3b**), indicating that the  
5  
6 centripetal orientation of epithelial cells is enhanced at low in-plane curvature.  
7  
8  
9

#### 10 11 12 **2.4. Low in-plane curvature promotes the formation of a supracellular actin cable at the** 13 14 **microwell edge.** 15 16

17  
18 Based on the modification of the cell orientation in response to the microwell radius, we next  
19  
20 sought to examine the organization of the actin cytoskeleton around the microwell edge. To this  
21  
22 aim, we performed confocal imaging within a short range of focal planes close to the microwell  
23  
24 edge (yellow line) (**Fig. 3c**). Our results indicated that actin accumulated at the microwell edge  
25  
26 to form a well-defined supracellular cable-like structure, resembling a purse string and  
27  
28 extending along the edge perimeter (**Fig. 3d and Supplementary Fig. 3**). Previous studies  
29  
30 reported actin ring structures in various developmental <sup>[27]</sup> and physiological processes <sup>[28]</sup>  
31  
32 previous works using flat epithelial monolayers indicated that such supracellular actin cables  
33  
34 sense and respond to the in-place local curvature of the gap <sup>[9][29][30]</sup>, contracting and pulling the  
35  
36 follower cells to heal the wound. The quantification of the integrated intensity (**Fig. 3e**) and  
37  
38 length (**Fig. 3f**) of this supracellular cable-like structure of actin in 30 μm, 65 μm and 100 μm  
39  
40 radius microwells indicated that supracellular cables were weaker and discontinuous at high in-  
41  
42 plane curvatures, while low in-plane curvatures (100 μm in radius) were characterized by  
43  
44 thicker and continuous cable structures.  
45  
46  
47  
48  
49  
50  
51

#### 52 53 54 **2.5. The Gaussian curvature at the microwell entrance promotes the maturation of the** 55 56 **supracellular actin cable architecture.** 57 58 59 60 61 62 63 64 65

1  
2  
3  
4  
5  
6  
7  
8  
9  
10  
11  
12  
13  
14  
15  
16  
17  
18  
19  
20  
21  
22  
23  
24  
25  
26  
27  
28  
29  
30  
31  
32  
33  
34  
35  
36  
37  
38  
39  
40  
41  
42  
43  
44  
45  
46  
47  
48  
49  
50  
51  
52  
53  
54  
55  
56  
57  
58  
59  
60  
61  
62  
63  
64  
65

To decouple the role of in-plane and Gaussian curvatures in the formation of supracellular actin cables, we imposed similar in-plane curvatures to epithelial monolayers by using 2D circular adhesive (**Supplementary Fig. 4a**) and non-adhesive (**Supplementary Fig. 4b**) micropatterns of 100  $\mu\text{m}$  in radius. As shown in **Supplementary Fig. 4c-d**, we observed the formation of a supracellular actin cable on both conditions, which contain a similar amount of actin than observed in 3D microwells (**Supplementary Fig. 4e**). Surprisingly, our findings showed that the normalized length of supracellular actin cables was significantly larger in 3D microwells than on adhesive and non-adhesive circular patterns (**Supplementary Fig. 4f**). Altogether, our findings showed that the Gaussian curvature imposed at the microwell entrance by its 3D morphology promotes the maturation of the supracellular actin cable architecture.

## 2.6. Cell straightness and speed are enhanced at the microwell edge.

Previous studies on 2D epithelial gap closure models have demonstrated that supracellular actin belts play a crucial role in coordinating migrating cells towards the center of the gap, enhancing cell directionality and persistence <sup>[31]</sup>. Additionally, recent evidence suggests that epithelial monolayers can adapt to curvature changes for maintaining homeostasis <sup>[20][32]</sup>. However, the specific contribution of curvature to collective dynamics is still unclear. The presence of a supracellular actin belt at the entrance of low in-plane curvature microwells raises important questions about the dynamic remodeling of curved epithelial monolayers lining lobular structures.

To address this question, we employed time-lapse microscopy to study the individual displacement of epithelial cells (**Supplementary Movie S4**) within confluent monolayers of similar densities located on either flat zones (**Fig. 4a**) or at the entrance of microwells with radii of 30  $\mu\text{m}$  and 100  $\mu\text{m}$  (**Fig. 4b**). Indeed, these sizes of microwells exhibited major differences of actin cytoskeleton with weak and discontinuous supracellular cables in 30  $\mu\text{m}$  microwells

1 and thicker and almost complete supracellular actin belts in 100  $\mu\text{m}$  microwells (**Figs. 3e-f**).  
2 Nuclei were labeled with Hoechst 33342 and their displacements were tracked over time on flat  
3 zones (**Fig. 4a**) and around the microwell edge (**Fig. 4b**) to determine straightness (**Fig. 4c**) and  
4 speed of each individual epithelial cell. Our results revealed that straightness of epithelial cells  
5 was significantly higher on large diameter microwells (**Fig. 4d**). Interestingly, cell speed was  
6 higher around microwell edges than on flat zones, but not significantly affected by the  
7 microwell diameter (**Fig. 4e**). Altogether, our findings demonstrate that cell orientation at the  
8 microwell entrance is accompanied by more directional and faster cell movements.  
9  
10  
11  
12  
13  
14  
15  
16  
17  
18  
19  
20  
21  
22

## 23 **2.7. The nuclear orientation around the microwell edge relies on contractile actomyosin** 24 **forces.**

25  
26  
27 During the nuclear tracking to determine the cell migration speed, we observed dynamic nuclear  
28 elongation and a preferential nuclear orientation in cells migrating towards the center of the  
29 microwell (**Supplementary Fig. 5**). To confirm these observations, nuclei located within a 60  
30  $\mu\text{m}$  annular zone around the microwell edge were immunostained with Hoechst 33342 and  
31 thresholded to determine their contour and long axis. The nuclear orientation was defined by  
32 the angle between the long nuclear axis and the ( $xy$ ) microwell axis (**Fig. 5a**). Immunostained  
33 images confirmed our results showing that nuclei around the edge of 30  $\mu\text{m}$  radius microwells  
34 exhibited random orientation (**Fig. 5b**), whereas increasing the microwell radius to 65  $\mu\text{m}$  (**Fig.**  
35 **5c**) and 100  $\mu\text{m}$  (**Fig. 5d**) induced a preferential orientation of the nuclei towards the ( $xy$ )  
36 microwell axis, consistent with the centripetal cellular orientation observed for low in-plane  
37 curvatures (**Fig. 3b**).  
38  
39  
40  
41  
42  
43  
44  
45  
46  
47  
48  
49  
50  
51  
52  
53

54  
55 We hypothesized therefore that nuclear orientation at the microwell entrance might be  
56 influenced by changes in actomyosin contractility. Indeed, nuclear orientation and deformation  
57 are linked to contractile tension in actin filaments <sup>[7][33]</sup>, which is transmitted to the nuclear  
58  
59  
60  
61  
62  
63  
64  
65

1 envelope through LINC complexes <sup>[34]</sup>. To test this hypothesis, we modulated myosin II-  
2 dependent contractility of the actin cytoskeleton with Blebbistatin, which inhibits myosin  
3 ATPase activity and suppresses actomyosin contraction <sup>[35]</sup>. The disruption of the actomyosin  
4 contractility with blebbistatin resulted in the collapse of the supracellular actin cable (**Fig. 5e-**  
5 **h** and **Supplementary Fig. 6**) and in random nuclear orientations in both 65  $\mu\text{m}$  (**Fig. 5g**) and  
6 100  $\mu\text{m}$  (**Fig. 5h**) microwells, which are similar to those observed in non-treated 30  $\mu\text{m}$   
7 microwells (**Fig 5b**).

8  
9  
10  
11  
12  
13  
14  
15  
16  
17 Altogether, our findings support the hypothesis that the contractile actomyosin ring may  
18 be involved in generating contractile forces that promote centripetal orientation of cells and  
19 nuclei at the microwell edge. Further experiments using laser ablation to dissect the actomyosin  
20 cytoskeleton with subcellular resolution will provide valuable insights into releasing the tension  
21 sustained by the supracellular actin cable <sup>[36]</sup> and elucidating its specific role in cellular and  
22 nuclear orientation.  
23  
24  
25  
26  
27  
28  
29  
30

## 31 **2.8. Gaussian curvature zones induce large vertical nuclear elongation.**

32  
33  
34  
35 Building upon the centripetal organization of cells and nuclei observed around the microwell  
36 edge in response to in-plane curvature values, we aimed to investigate the potential influence  
37 of Gaussian curvature on nuclear organization within the microwell. To address this, we  
38 determined the 3D morphology of the epithelial cell nuclei located at the highest convex  
39 curvature zone (**See Fig. 2b-c**). Confocal views of 30  $\mu\text{m}$ , 65  $\mu\text{m}$  and 100  $\mu\text{m}$  radius microwells  
40 (**Fig. 6a**) revealed a uniform distribution of nuclei along the microwell periphery with their long  
41 axis predominately oriented vertically towards the microwell bottom.  
42  
43  
44  
45  
46  
47  
48  
49  
50  
51  
52  
53  
54  
55

56 We first explore whether epithelial cells underwent morphological changes in response  
57 to the modulation of the Gaussian curvature by quantifying the 2D cell shape index (CSI). As  
58  
59  
60  
61  
62  
63  
64  
65

1 shown in **Fig. 6b**, the CSI decreased linearly with increasing the Gaussian curvature, suggesting  
2 that cells elongate to accommodate Gaussian curvature. We then assumed a nuclear  
3 morphology represented by a 3D ellipsoid with its long axis oriented towards the microwell  
4 bottom (**Fig. 6c**). To get more insight into the 3D nuclear shape changes, we quantified the two  
5 minor axes of the ellipsoid from confocal views of thresholded nuclei. Our results demonstrated  
6 a linear increase in the minor axis ratio with the Gaussian curvature (**Fig. 6d**), indicating that  
7 higher Gaussian curvatures resulted in more flattened nuclei, consistent with previous  
8 observations on crests of corrugated hydrogels <sup>[20]</sup>. Furthermore, in addition to being flattened,  
9 nuclei exhibited significant elongation as the Gaussian curvature increased (**Fig. 6e**) and a lower  
10 nuclear volume than nuclei on flat zones (**Fig. 6f**). Notably, our findings revealed a linear  
11 relationship between 3D nuclear elongation and Gaussian curvature, with the highest Gaussian  
12 curvatures leading to an approximate threefold increase in nuclear elongation. Collectively, our  
13 results demonstrate that Gaussian curvatures imposed by microwells mimicking lobular  
14 structures induce a vertical orientation of the nuclei towards the microwell axis and trigger  
15 substantial 3D nuclear elongation.

## 2.9. Elongated nuclei at high Gaussian curvature zones exhibit highly compacted chromatin domains.

16 Given the association between nuclear shape changes and chromatin organization<sup>[7][33]</sup>, we  
17 investigated whether nuclear elongations observed at the Gaussian zone of the microwell  
18 entrance could lead to differences in chromatin state. To this aim, we focused our attention on  
19 the more elongated nuclei corresponding to the largest Gaussian curvature values (**Fig. 6e**).  
20 Utilizing quantitative procedures based on DAPI staining and 3D confocal imaging at high  
21 magnifications <sup>[7][20]</sup>, we determined the average spatial density of chromatin, which is a reliable  
22 indicator of chromatin condensation. Our results demonstrated that elongated nuclei localized

1 at the maximal Gaussian curvature zone exhibited a lower volume (**Fig. 6f**) and higher levels  
2 of fluorescence intensity (**Fig. 6g**) compared to rounded nuclei in flat zones (**Fig. 6h**),  
3 suggesting a significant modification of the chromatin state in elongated nuclei at maximal  
4 Gaussian curvature zones. To further confirm this hypothesis, we quantified the chromatin  
5 compaction on flat and Gaussian curvature zones. As shown in **Fig. 6i**, our findings revealed  
6 higher chromatin compaction values in Gaussian curvature zones ( $0.39\pm 0.11$ ) than in flat ones  
7 ( $0.17\pm 0.13$ ). These results suggest that the Gaussian curvature imposed at the microwell  
8 entrance leads to a nuclear elongation, which is accompanied by a nuclear volume loss and  
9 higher levels of chromatin condensation. To confirm these results, we characterized the level  
10 of histone H3 acetylation at lysine 9 (H3K9ac) by immunostaining to determine the level of  
11 euchromatin histone marks, which correspond to the loosely packed chromatin domain that is  
12 transcriptionally accessible <sup>[37]</sup> (**Fig. 6j**). Our findings revealed that elongated nuclei located at  
13 high Gaussian curvature zones exhibited a lower percentage of euchromatin (**Fig. 6k**), further  
14 confirming a highly compacted chromatin state.  
15  
16  
17  
18  
19  
20  
21  
22  
23  
24  
25  
26  
27  
28  
29  
30  
31  
32  
33  
34  
35  
36

### 37 **3. Discussion**

38  
39  
40  
41 Recent advances in hydrogel synthesis and microscale patterning have led to new  
42 advances in understanding the role of physical cues of the matrix in cell organization <sup>[19]</sup>.  
43 Among the role of stiffness and small-scale topographies, cumulative evidence has shown that  
44 matrix curvature affects spatiotemporal organization of cells and tissues <sup>[10]</sup>. Despite recent  
45 advances in microfabrication techniques, including micro-machining <sup>[17]</sup>, soft lithography <sup>[38]</sup>,  
46 and two-photon polymerization <sup>[39]</sup>, fabricating curved cellular environments in soft matrices  
47 remains challenging. Therefore, novel technologies are needed to enable more comprehensive  
48  
49  
50  
51  
52  
53  
54  
55  
56  
57  
58  
59  
60  
61  
62  
63  
64  
65

1 studies of cell responses to different substrate curvatures and to can mimic the complexity of in  
2 vivo structures.

3  
4  
5 In this study, we examined how changes of in-plane and Gaussian curvatures influence  
6 the cytoskeletal architecture of epithelial monolayers, and their subsequent effects on nuclear  
7 morphology and chromatin compaction. The photopolymerization-based nature of our  
8 experimental strategy enables reproducible and cost-effective hydrogel patterning, making it  
9 easily implementable in various laboratories for creating customized microwell shapes in soft  
10 culture matrices without the need for replica molding or advanced material science expertise.

11  
12  
13  
14  
15  
16  
17  
18  
19  
20 Our findings reveal that an increase in microwell diameter promotes the development  
21 of a supracellular actin cable at the microwell edge, resembling a purse string and extending  
22 along the perimeter. Furthermore, we have shown that the Gaussian curvature at the microwell  
23 entrance enhances the maturation of the supracellular actin cable architecture, resulting in a  
24 preferential cellular and nuclear orientation around the microwell edge. These results are of  
25 significant interest within the context of recent studies aimed at elucidating the role of  
26 actomyosin contractility in lobular structures. For instance, a recent report indicates that  
27 elongated keratinocytes form an actin rim that exerts contractile forces around the mammary  
28 bud to drive an invagination process <sup>[40]</sup>. Collectively, these findings suggest that contractile  
29 circular structures of actin formed by epithelial cells in mammary tissues could be influenced  
30 by local curvature changes prevalent in lobular structures. Further investigations employing in  
31 vivo and in vitro experiments will be needed to confirm this hypothesis. Cutting-edge  
32 techniques, such as laser ablation to dissect the actomyosin cytoskeleton <sup>[36]</sup> or computational  
33 methods to map the internal stress in curved epithelial <sup>[41]</sup>, will offer valuable insights to  
34 quantify the tension sustained by supracellular actin cables and unravel their specific roles in  
35 maintaining lobular structure homeostasis.

36  
37  
38  
39  
40  
41  
42  
43  
44  
45  
46  
47  
48  
49  
50  
51  
52  
53  
54  
55  
56  
57  
58  
59  
60  
61  
62  
63  
64  
65



1  
2  
3  
4  
5  
6  
7  
8  
9  
10  
11  
12  
13  
14  
15  
16  
17  
18  
19  
20  
21  
22  
23  
24  
25  
26  
27  
28  
29  
30  
31  
32  
33  
34  
35  
36  
37  
38  
39  
40  
41  
42  
43  
44  
45  
46  
47  
48  
49  
50  
51  
52  
53  
54  
55  
56  
57  
58  
59  
60  
61  
62  
63  
64  
65

In addition, our observations revealed that Gaussian curvatures imposed at the microwell entrance can significantly impact the organization and dynamics of epithelial tissues, thereby modulating cytoskeletal forces acting on the nucleus and resulting in notable changes in nuclear orientation and chromatin compaction. The mechanisms of curvotaxis are still not well understood and it would be very interesting to further investigate the role of cell-matrix adhesions in the curve detection mechanism. Indeed, talin has been reported as a key player of the molecular clutch process that explains force transmission and transduction in response to matrix rigidity <sup>[42]</sup>, and its potential role in curvotaxis needs to be investigated.

These novel insights into the influence of curvature in anatomically relevant 3D microstructures on epithelial tissues contribute to a deeper understanding of curvature-responsive mechanical regulation in epithelial tissues that line lobular structures. By opening up new avenues for creating complex microenvironments, our strategy holds promise for investigating fundamental questions in cellular biology, such as the role of matrix curvature in stem cell differentiation regulation and the etiology of diseases associated with curved microenvironments, including cancer progression <sup>[12]</sup>. Furthermore, we anticipate that incorporating spatially controlled surface curvature as a material design parameter could serve as a simple yet powerful tool for enhancing tissue regeneration, biomaterial design, culture conditions, and drug testing.

## 4. Experimental Section

**Photopolymerization of the microwells.** Round glass coverslips of 22 mm in diameter were incubated 5 min in NaOH 0.1M, then rinsed 3 times with distilled water and dried with a nitrogen flow. A solution of 3-(trimethoxysilyl) propyl acrylate was incubated on clean coverslips for 1 hour. Coverslips were rinsed abundantly with distilled water and dried. A mix

1 solution was prepared containing hydroxyethylacrylamide (HEA), 28.6 % w/w aqueous  
2 acrylamide solution, 1.96 % w/w aqueous bisacrylamide solution, 1- [4- (2-hydroxyethoxy)  
3 phenyl] - 2-hydroxy-2-methyl-1-propanone (Irgacure 2959, 5mg/ml) and water to get final  
4 concentrations of 15% and 1/23 ratio of bisacrylamide to acrylamide. The solution was  
5 degassed during 15 min by nitrogen bubbling. A 50 µl droplet of the mix hydrogel solution was  
6 deposited on each pattern of a quartz photomask (Compugraphics, UK) and squeezed with a  
7 circular glass coverslip. The photomask was then insulated with UVA lights (Dymax) at a  
8 power of 10 mW/cm<sup>2</sup> for 10 minutes. Each glass coverslip covered with a microstructured  
9 hydrogel was then gently peeled off the photomask and swelled in sterile water for 24 hours.  
10 Hydrogels were sterilized by a germicide UV treatment of 15 min and incubated with 75 µg/ml  
11 solution of fibronectin for 1 hour and then rehydrated before cell seeding in sterile medium at  
12 37°C for 4 hours.

13  
14  
15  
16  
17  
18  
19  
20  
21  
22  
23  
24  
25  
26  
27  
28  
29 **Cell culture.** RFP E-cadherin expressing epithelial cells from the Madin–Darby canine kidney  
30 (MDCK) cell line were cultured in DMEM (Dubecco's Modified Eagle's medium)  
31 supplemented with 10% FBS (Fetal Bovine Serum, AE Scientific) and 1% antibiotic (Penicillin,  
32 Streptomycin, AE Scientific). MDCK cells were seeded on microstructured hydrogels at  
33 100,000 cells/cm<sup>2</sup> and incubated for 24 hours at 37°C with 5% of CO<sub>2</sub> in an environment  
34 saturated in humidity.

35  
36  
37  
38  
39  
40  
41  
42  
43  
44 **Immunostainings and drug treatment.** Cells were fixed with a 4% solution of  
45 paraformaldehyde and 0.05% Triton X-100 in PBS for 15 min at 37°C and washed three times  
46 in PBS. Nuclei and actin cytoskeleton were labelled by an incubation for 1 hour at RT with  
47 Hoechst 33342 and Alexa Fluor 488 Phalloidin (Molecular Probes, Invitrogen) and then rinsed  
48 3X with PBS. The coverslips with hydrogel microwells were then placed on a microscope  
49 sample-holder and covered with glycerol for imaging. Actomyosin contractility of MDCK cells  
50  
51  
52  
53  
54  
55  
56  
57  
58  
59  
60  
61  
62  
63  
64  
65

1 was inhibited with 100  $\mu\text{M}$  of blebbistatin for 1 hour. Cells were then immediately fixed and  
2 stained.  
3

4  
5 **Time-lapse experiments.** MDCK cells were seeded on microstructured hydrogels at 100,000  
6 cells/ $\text{cm}^2$  and incubated for 24 hours at 37°C with 5% of  $\text{CO}_2$  in a humidity-saturated  
7 environment. Time-lapse experiments were carried out with an inverted confocal microscope  
8 (Nikon TI2 A1R HD25, Japan) after 24 hours of incubation using a cage incubator (Okolab) to  
9 maintain the temperature at 37°C, 5%  $\text{CO}_2$  level and a high level of humidity. Acquisitions  
10 were made with 10-minute time intervals for a total duration of 10 hours.  
11  
12

13  
14  
15  
16  
17  
18  
19  
20 **Confocal microscopy.** 3D confocal images were acquired on an inverted Nikon Ti2 A1R HD25  
21 confocal microscope using Plan Apochromat silicon immersion lenses:  $\times 25$  (N.A.=1.05,  
22 W.D.=0.55 mm),  $\times 40$  (N.A.=1.25, W.D.=0.30 mm) and  $\times 100$  (N.A.=1.35, W.D.=0.30 mm).  
23 Images were acquired using small Z-depth increments of 0.125  $\mu\text{m}$  and the NIS Elements  
24 imaging software (NIS Elements Advanced Research v5.2). High resolution confocal images  
25 were acquired with a galvanometer-based scanner and Z-stack confocal time-lapses with a high-  
26 speed resonant scanner.  
27  
28

29  
30  
31  
32  
33  
34  
35  
36  
37  
38 **Images correction.** A flat-field correction (FFC) technique was used to improve image quality  
39 and to cancel the effects of image artifacts caused by variations in the pixel-to-pixel sensitivity  
40 of the detector and by distortions in the optical path. FFC corrections were performed in Fiji  
41 using the BaSiC plugin based on low-rank and sparse decomposition <sup>[43]</sup>.  
42  
43  
44  
45  
46  
47

48  
49  
50  
51 **Microwell profiles.** Samples were incubated with a solution of fluorescent particles of 0.2  $\mu\text{m}$   
52 in diameter (Fluospheres, Molecular Probes, Eugene, OR) diluted in glycerol. Confocal stacks  
53 were performed to obtain the transversal ( $xz$ ) cross-section. Microwell profiles were obtained  
54 from the outline of their topography thanks to binarization and skeletonizing of transversal ( $xz$ )  
55 cross-sections. A hyperbolic tangent function,  $y = \tanh(x)$  was then fitted to the half of the  
56  
57  
58  
59  
60  
61  
62  
63  
64  
65

1 microwell profile by a non-linear regression. The curvature was calculated at each point on the  
2 fitted equation by  $\kappa = \ddot{y} / (1 + \dot{y}^2)^{3/2}$  where the dot and double dot represent the first and the  
3  
4 second derivative of the function, respectively. The local maxima and minima of curvature  
5  
6 correspond to the most convex and most concave points, respectively. The quantification was  
7  
8 performed from at least 3 cross-sections obtained from 3 independent replicates.  
9  
10

11  
12 **Cellular density.** High resolution confocal images of m-cherry cadherin MDCK cells were  
13  
14 acquired at x40 (silicon objective) with an inverted confocal microscope (Nikon TI2 AIR  
15  
16 HD25, Japan). Individual cells located at either the flat zone or the Gaussian curvature zone  
17  
18 were segmented 3D confocal images of m-cherry cadherin confocal images using the image  
19  
20 analysis software package MorphGraphX). The total number of cells in each zone was  
21  
22 normalized by the corresponding surface area to obtain a cellular density. The surface area of  
23  
24 Gaussian curvature zone was approximated as one-quarter of the surface area of a torus of  
25  
26 similar Gaussian curvature. To determine the surface area of ROI at the Gaussian curvature  
27  
28 zones, we converted 3D z stack images of MDCK into 2D projections by using a method  
29  
30 previously used for tubes <sup>[44]</sup>. Background subtraction was performed to reduce signal-to-noise  
31  
32 ratio and z stack images were then resliced to project the xz plane for the circular cross section  
33  
34 of MDCK tissues. Afterward, a circle was fit to the Gaussian curvature zone and the perimeter  
35  
36 obtained was mapped into a line, which was straightened and resliced again to obtain a 2D  
37  
38 projection of the virtually flattened zone.  
39  
40  
41  
42  
43  
44  
45  
46

47 **2D and 3D nuclear orientation.** A Maximal Intensity Projection (MIP) image was created  
48  
49 from the Z slices corresponding to the top of the microwells. A circular region of interest (ROI)  
50  
51 centered on the center of the microwell and having a radius of 60 microns larger than the niche  
52  
53 radius was selected on each MIP image. Nuclei entirely included in the ROI were fitted by an  
54  
55 ellipse defined by a long and a short axis. The angle formed between the long nuclear axis and  
56  
57 the axis passing through the microwell center and the ellipse center of mass was used to  
58  
59  
60  
61  
62  
63  
64  
65

1 determine the nuclear orientation. 3D nuclear orientations and elongations were obtained from  
2 a 3D thresholding of Z stacks in NIS Elements. Nuclei included in the flat region around the  
3  
4 microwells (for control) or in the 30 first microns in depth at the entry of the niche were selected  
5  
6 and their 3D pitch as well as 3D elongation were measured.  
7  
8  
9

10 **Mechanical measurements.** The Young's modulus of immersed microwells was measured  
11  
12 with indentation (Chiaro, Optics11, The Netherlands) using spherical probe with a radius of 9  
13  
14  $\mu\text{m}$  and a stiffness of 0.49 N/m. Elastic moduli were determined by fitting force-indentation  
15  
16 curves with the Hertz equation.  
17  
18  
19

20 **2D projection and 3D tracking.** 3D confocal images of curved epithelial were projected on  
21  
22 2D surfaces using the LocalZprojector toolbox plugin <sup>[45]</sup> in Fiji. This correction algorithm was  
23  
24 used to project confocal images of either of m-cherry cadherin or AlexFluor 488 stained MDCK  
25  
26 tissues to determine the surface area of individual cells or the morphology of the actin ring at  
27  
28 the Gaussian curvature zone. Projection images of the Gaussian curvature zone were obtained  
29  
30 using standard deviation (std) filter for height map and the MIP (maximum intensity projection)  
31  
32 method for local projection.  
33  
34  
35  
36  
37

38 **Image analysis.** The quantification of the actin ring integrated intensity was realized on  
39  
40 confocal images obtained at high magnification (Nikon TI2 A1R HD25, Japan with  $\times 40$   
41  
42 silicone objective). Plot profiles of the actin fluorescence signal were drawn perpendicularly to  
43  
44 the periphery of the microwell borders in FIJI to determine the area under the curve that  
45  
46 corresponds to the actin ring fluorescence intensity. This signal was corrected by using a  
47  
48 baseline corresponding to the mean actin fluorescence signal inside the whole tissue. The length  
49  
50 of actin rings was manually measured on confocal images with Fiji for at least 4 different tissues  
51  
52 and then normalized by the perimeter of the microwell.  
53  
54  
55  
56  
57  
58  
59  
60  
61  
62  
63  
64  
65

1  
2  
3  
4  
5  
6  
7  
8  
9  
10  
11  
12  
13  
14  
**Nuclear volume.** The nuclear volume was measured on 3D confocal images acquired with high-resolution ( $\times 40$  or  $\times 100$  silicone) objectives on a Nikon A1R laser-scanning microscope (Nikon, Japan) with Z increments of  $0.125\ \mu\text{m}$ . Confocal images were deconvolved using a precalculated point spread function (PSF), after which cell boundaries were determined using Otsu's method in Fiji. Voxels within the nuclear boundary of each stack were determined using the Voxel counter plugin in Fiji and included in the calculation of the nuclear volume.

15  
16  
17  
18  
19  
20  
21  
22  
23  
24  
25  
26  
27  
28  
29  
30  
31  
32  
33  
34  
**Euchromatin staining and quantification.** MDCK cells were fixed and permeabilized with a 10 min incubation in PAF 4% and Triton X-100 1:2000 and blocked with a 30 min incubation in Tris-Tween 0.1% buffer with BSA 1%. DNA was stained with Hoechst 33342 for 1 hour, while euchromatin was stained with 1/200 H3KP9ac antibody (MA5-11195 ThermoScientific) for 1 hour. Cells were rinsed three times in Tris-Tween 0.1% buffer for 30 min each and incubated for an hour with 1/200 anti-rabbit FITC. Hoechst 33342 and euchromatin fluorescence signals were 3D thresholded with NIS Analysis Advanced Software (Nikon, Japan). Euchromatin and DNA volumes were determined from confocal stacks.

35  
36  
37  
38  
39  
40  
41  
42  
43  
44  
45  
46  
47  
48  
49  
50  
51  
52  
53  
54  
55  
56  
57  
58  
59  
60  
61  
62  
63  
64  
65  
**Adhesive 2D micropatterns.** Flat hydroxy-PAAm hydrogels containing 15% acrylamide and 1/23 ratio of bisacrylamide to acrylamide were polymerized with TEMED and APS. Hydroxy-PAAm hydrogels were photopatterned (PRIMO Alvéole, France). Negative and positive round patterns of  $100\ \mu\text{m}$  radius were designed with Inkscape. A solution of poly-L-lysine at  $100\ \mu\text{g/ml}$  (Sigma-Aldrich, Saint-Louis, MO, USA) was incubated at the surface of flat hydroxy-PAAm for 30 min. Hydrogels were washed three times with PBS (Capricorn, Germany) and with HEPES (Sigma-Aldrich, Saint-Louis, MO, USA) at  $\text{pH} = 8.3$ . Hydrogels were then passivated with a  $50\ \text{mg/ml}$  solution of PEG coupled with succinimidyl valerate (mPEG-SVA, Laysan Bio Inc., USA) at  $\text{pH} = 8.3$  for one hour, followed by three PBS rinses. Hydrogels were then transferred to the microscope stage and covered with a drop of photosensitive reagent PLPP gel (Alvéole, France) that was impaired under UV illumination (PRIMO Alvéole, France)

1  
2  
3  
4  
5  
6  
7  
8  
9  
10  
11  
12  
13  
14  
15  
16  
17  
18  
19  
20  
21  
22  
23  
24  
25  
26  
27  
28  
29  
30  
31  
32  
33  
34  
35  
36  
37  
38  
39  
40  
41  
42  
43  
44  
45  
46  
47  
48  
49  
50  
51  
52  
53  
54  
55  
56  
57  
58  
59  
60  
61  
62  
63  
64  
65

at 400 mJ/mm<sup>2</sup>. Hydrogels were then incubated for 10 min with a 75 µg/ml solution of fibronectin from human plasma (Merck Millipore, Germany) and rinsed with sterile PBS (Capricorn, Germany) before use. Photopatterning was controlled by incubating the sample in a solution of rhodamine-labelled fibronectin (Cytoskeleton Inc., USA, ref FNR-01B).

**Time-lapse experiments.** Time-lapse experiments were performed with a genetically modified cell line that stably expresses F-actin fused to GFP. Cells were imaged 90 minutes before to add 5 µM of Blebbistatin (Enzo Life Sciences) in the culture medium. Time-lapse was then recorded every 10 minutes for 10 hours in epifluorescent or Z-stack confocal mode.

**Statistical analysis.** Differences in means between groups were evaluated by two-tailed Student's *t*-tests performed in Prism 9 (GraphPad Software). For multiple comparisons, the differences were determined by using an analysis of variance followed by Tukey's post-hoc test. \**p* < 0.0500; \*\**p* < 0.0100; \*\*\**p* < 0.0010; \*\*\*\**p* < 0.0001; n.s., not significant. Unless stated otherwise, all data are presented as mean ± standard deviation (s.d.).

## Supporting Information

Supporting Information is available from the Wiley Online Library or from the author.

## Acknowledgments

S.G. acknowledges funding from FEDER PROSTEM Research project no. #1510614 (Wallonia DG06), the F.R.S.-FNRS EPIFORCE Project no. T.0092.21, the F.R.S.-FNRS CELLSQUEEZER project no. #J.0061.23, the F.R.S.-FNRS OPTOPATTERN Project no. #U.NO26.22, the Win<sup>2</sup>Wal INERVODERM project no. #2210040 (Wallonia DG06) and the Interreg MAT(T)ISSE project, which is financially supported by Interreg France-Wallonie-Vlaanderen (Fonds Européen de Développement Régional, FEDER-ERDF). M.L. is financially

1 supported by a WBI.World Scholarship Fellowship from the Wallonia-Brussels  
2 International (WBI) Excellence Grants Programme. Y.K. is financially supported by FRIA  
3 (F.R.S.- FNRS). [F-actin GFP MDCK cells are a gift from Benoit Ladoux \(Institut Jacques](#)  
4 [Monod, Paris\)](#). The authors thank Denis Dumont and Guillaume Pernollet for their technical  
5 help.  
6  
7  
8  
9  
10

## 11 **Conflicts of Interest**

12 The authors declare no conflict of interest.  
13  
14  
15

## 16 **Author contribution**

17 S.G., M.L. and M.V. conceived the project and S.G. supervised the project. M.L. developed  
18 photopolymerization methods of hydrogels. M.V. and M.L performed cell experiments and  
19 imaging. M.V. and M.L. and S.G. analyzed data. The article was written by M.L., M.V., Y.K.  
20 and S.G., read and corrected by all authors, who all contributed to the interpretation of the  
21 results.  
22  
23  
24

## 25 **Data Availability Statement**

26 The data that support the findings of this study are available in the supplementary material of  
27 this article.  
28  
29  
30  
31  
32  
33  
34  
35  
36  
37  
38  
39

## 40 **Keywords**

41 Curved hydrogel, epithelial monolayer, cytoskeleton, nuclear mechanics, tissue engineering  
42  
43  
44  
45  
46  
47  
48  
49  
50  
51  
52  
53  
54  
55  
56  
57  
58  
59  
60  
61  
62  
63  
64  
65



- 1 [1] D. Mohammed, M. Versaevel, C. Bruyère, L. Alaimo, M. Luciano, E. Vercruyse, A.  
2 Procès, S. Gabriele, *Front. Bioeng. Biotechnol.* **2019**, 7, 162.
- 3 [2] A. Shellard, R. Mayor, *Nature* **2021**, 600, 690.
- 4 [3] M. Riaz, M. Versaevel, D. Mohammed, K. Glinel, S. Gabriele, *Sci Rep* **2016**, 6,  
5 34141.
- 6 [4] C. Labouesse, B.X. Tan, C.C. Agle, M. Hofer, A.K. Winkel, G.G. Stirparo, H.T.  
7 Stuart, C.M. Verstreken, C. Mulas, W. Mansfield, P. Bertone, K. Franze, J.C.R. Silva, K.J.  
8 Chalut, *Nat Commun* **2021**, 12, 6132.
- 9 [5] B. Yi, *Bioactive Materials* **2022**, 15, 82.
- 10 [6] J. Creff, R. Courson, T. Mangeat, J. Foncy, S. Souleille, C. Thibault, A. Besson, L.  
11 Malaquin, *Biomaterials* **2019**, 221, 119404.
- 12 [7] M. Versaevel, T. Grevesse, S. Gabriele, *Nat Commun* **2012**, 3, 671.
- 13 [8] K.A. Kilian, B. Bugarija, B.T. Lahn, M. Mrksich, *Proc Natl Acad Sci USA* **2010**, 107,  
14 4872.
- 15 [9] T. Chen, A. Callan-Jones, E. Fedorov, A. Ravasio, A. Brugués, H.T. Ong, Y. Toyama,  
16 B.C. Low, X. Trepas, T. Shemesh, R. Voituriez, B. Ladoux, *Nat. Phys.* **2019**, 15, 393.
- 17 [10] S.J.P. Callens, R.J.C. Uyttendaele, L.E. Fratila-Apachitei, A.A. Zadpoor, *Biomaterials*  
18 **2020**, 232, 119739.
- 19 [11] D. Baptista, L. Teixeira, C. van Blitterswijk, S. Giselsbrecht, R. Truckenmüller, *Trends*  
20 *in Biotechnology* **2019**, 37, 838.
- 21 [12] H.A. Messal, S. Alt, R.M.M. Ferreira, C. Gribben, V.M.-Y. Wang, C.G. Cotoi, G.  
22 Salbreux, A. Behrens, *Nature* **2019**, 566, 126.
- 23 [13] N.D. Bade, R.D. Kamien, R.K. Assoian, K.J. Stebe, *Sci. Adv.* **2017**, 3, e1700150.
- 24 [14] M. Werner, S.B.G. Blanquer, S.P. Haimi, G. Korus, J.W.C. Dunlop, G.N. Duda,  
25 Dirk.W. Grijpma, A. Petersen, *Adv. Sci.* **2017**, 4, 1600347.
- 26 [15] M. Werner, A. Petersen, N.A. Kurniawan, C.V.C. Bouten, *Adv. Biosys.* **2019**, 3,  
27 1900080.
- 28 [16] J.Y. Park, D.H. Lee, E.J. Lee, S.-H. Lee, *Lab Chip* **2009**, 9, 2043.
- 29 [17] L. Pieuchot, J. Marteau, A. Guignandon, T. Dos Santos, I. Brigaud, P.-F. Chauvy, T.  
30 Cloatre, A. Ponche, T. Petithory, P. Rougerie, M. Vassaux, J.-L. Milan, N. Tusamda  
31 Wakhloo, A. Spangenberg, M. Bigerelle, K. Anselme, *Nat Commun* **2018**, 9, 3995.
- 32 [18] A.G. Castaño, M. García-Díaz, N. Torras, G. Altay, J. Comelles, E. Martínez,  
33 *Biofabrication* **2019**, 11, 025007.
- 34 [19] G.J. Pahapale, J. Tao, M. Nikolic, S. Gao, G. Scarcelli, S.X. Sun, L.H. Romer, D.H.  
35 Gracias, *Advanced Science* **2022**, 9, 2104649.
- 36 [20] M. Luciano, S.-L. Xue, W.H. De Vos, L. Redondo-Morata, M. Surin, F. Lafont, E.  
37 Hannezo, S. Gabriele, *Nat. Phys.* **2021**, 17, 1382.
- 38 [21] M. Rostovskaya, *Cell Stem Cell* **2022**, 29, 744.
- 39 [22] T. Grevesse, M. Versaevel, G. Circelli, S. Desprez, S. Gabriele, *Lab Chip* **2013**, 13,  
40 777.
- 41 [23] L. Conrad, S.V.M. Runser, H. Fernando Gómez, C.M. Lang, M.S. Dumond, A.  
42 Sapala, L. Schaumann, O. Michos, R. Vetter, D. Iber, *Development* **2021**, 148, dev194209.
- 43 [24] M. Mederacke, L. Conrad, R. Vetter, D. Iber, *Geometric Effects Position Renal*  
44 *Vesicles During Kidney Development*, *Developmental Biology* **2022**.
- 45 [25] M. Peurla, O. Paavolainen, E. Tammelinen, S.-R. Sulander, L. Mourao, P. Boström, N.  
46 Brück, C.L. Scheele, P. Hartiala, E. Peuhu, *Morphometric Analysis of the Terminal Ductal*  
47 *Lobular Unit Architecture in Human Breast*, **n.d.**
- 48 [26] Y. Kalukula, M. Luciano, S. Gabriele, *Clinical & Translational Med* **2022**, 12.
- 49 [27] J.D. Franke, R.A. Montague, D.P. Kiehart, *Current Biology* **2005**, 15, 2208.
- 50 [28] C. Schwayer, *Developmental Cell* **2016**, 37, 493.
- 51  
52  
53  
54  
55  
56  
57  
58  
59  
60  
61  
62  
63  
64  
65

- 1 [29] Q. Wei, X. Shi, T. Zhao, P. Cai, T. Chen, Y. Zhang, C. Huang, J. Yang, X. Chen, S.  
2 Zhang, *Proc. Natl. Acad. Sci. U.S.A.* **2020**, *117*, 33263.
- 3 [30] S.R.K. Vedula, H. Hirata, M.H. Nai, A. Brugués, Y. Toyama, X. Trepát, C.T. Lim, B.  
4 Ladoux, *Nature Mater* **2014**, *13*, 87.
- 5 [31] E. Anon, X. Serra-Picamal, P. Hersen, N.C. Gauthier, M.P. Sheetz, X. Trepát, B.  
6 Ladoux, *Proceedings of the National Academy of Sciences* **2012**, *109*, 10891.
- 7 [32] C. Tomba, V. Luchnikov, L. Barberi, C. Blanch-Mercader, A. Roux, *Developmental*  
8 *Cell* **2022**, *57*, 1257.
- 9 [33] Y. Kalukula, A.D. Stephens, J. Lammerding, S. Gabriele, *Nat Rev Mol Cell Biol* **2022**.
- 10 [34] M. Versaevel, J.-B. Braquenier, M. Riaz, T. Grevesse, J. Lantoine, S. Gabriele, *Sci*  
11 *Rep* **2015**, *4*, 7362.
- 12 [35] A.F. Straight, A. Cheung, J. Limouze, I. Chen, N.J. Westwood, J.R. Sellers, T.J.  
13 Mitchison, *Science* **2003**, *299*, 6.
- 14 [36] A.B. Kobb, K.E. Rothenberg, R. Fernandez-Gonzalez, *MBoC* **2019**, *30*, 2901.
- 15 [37] Y. Kalukula, A.D. Stephens, J. Lammerding, S. Gabriele, *Nat Rev Mol Cell Biol* **2022**,  
16 *23*, 583.
- 17 [38] G.M. Whitesides, E. Ostuni, S. Takayama, X. Jiang, D.E. Ingber, *Annu. Rev. Biomed.*  
18 *Eng.* **2001**, *3*, 335.
- 19 [39] T. Weiß, G. Hildebrand, R. Schade, K. Liefelth, *Eng. Life Sci.* **2009**, *9*, 384.
- 20 [40] E. Trela, Q. Lan, S.-M. Myllymäki, C. Villeneuve, R. Lindström, V. Kumar, S.A.  
21 Wickström, M.L. Mikkola, *Journal of Cell Biology* **2021**, *220*, e202008062.
- 22 [41] A. Marín-Llauradó, S. Kale, A. Ouzeri, T. Golde, R. Sunyer, A. Torres-Sánchez, E.  
23 Latorre, M. Gómez-González, P. Roca-Cusachs, M. Arroyo, X. Trepát, *Nat Commun* **2023**,  
24 *14*, 4014.
- 25 [42] A. Elosegui-Artola, R. Oria, Y. Chen, A. Kosmalska, C. Pérez-González, N. Castro, C.  
26 Zhu, X. Trepát, P. Roca-Cusachs, *Nat Cell Biol* **2016**, *18*, 540.
- 27 [43] T. Peng, K. Thorn, T. Schroeder, L. Wang, F.J. Theis, C. Marr, N. Navab, *Nat*  
28 *Commun* **2017**, *8*, 14836.
- 29 [44] W. Xi, S. Sonam, T. Beng Saw, B. Ladoux, C. Teck Lim, *Nat Commun* **2017**, *8*, 1517.
- 30 [45] S. Herbert, L. Valon, L. Mancini, N. Dray, P. Caldarelli, J. Gros, E. Esposito, S.L.  
31 Shorte, L. Bally-Cuif, N. Aulner, R. Levayer, J.-Y. Tinevez, *BMC Biol* **2021**, *19*, 136.
- 32  
33  
34  
35  
36  
37  
38  
39  
40  
41  
42  
43  
44  
45  
46  
47  
48  
49  
50  
51  
52  
53  
54  
55  
56  
57  
58  
59  
60  
61  
62  
63  
64  
65

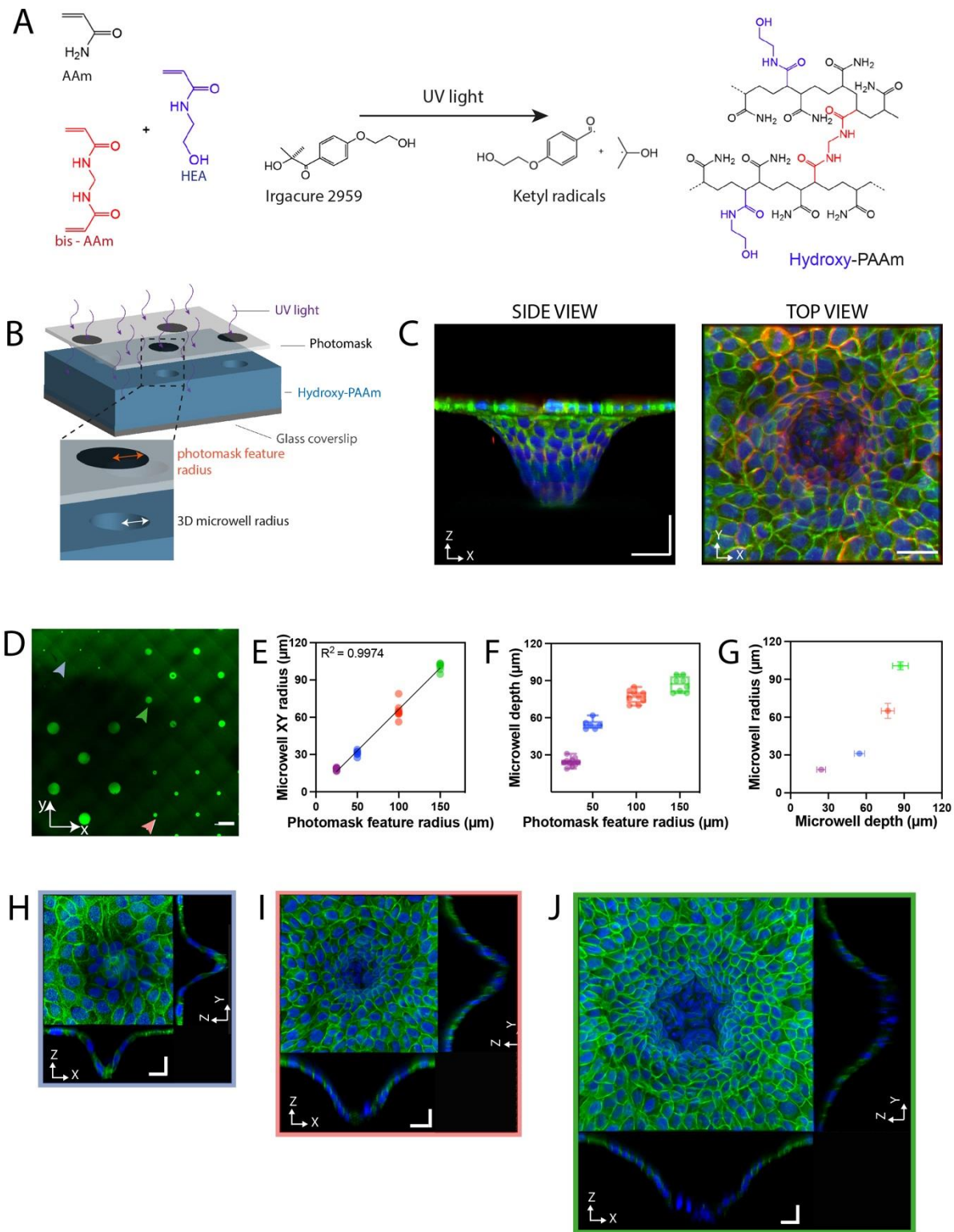


**Figure 1 – Microfabrication and epithelialization of 3D microwells.** (A) The radical polymerization of acrylamide (AAm, in black), bis-acrylamide (bis-AAm, in red) and N-hydroxyethylacrylamide (HEA, in blue) is amorced by the photoinitiator Irgacure 2959 under

1 UV illumination, leading to the polymerization of a polyacrylamide hydrogel with hydroxyl  
2 groups (hydroxy-PAAm). (B) Bowl-shaped 3D microwells are formed by photopolymerizing  
3 hydroxy-PAAm hydrogels through a transparent chromium optical photomask that contains  
4 circular dark patterns. (C) Confocal images showing side ( $xz$ ) and top ( $xy$ ) views of an epithelial  
5 monolayer covering the surface of a 3D microwell. Cadherins are labelled in red, actin filaments  
6 in green and DNA in blue. Scale bars are 50  $\mu\text{m}$ . (D) Large image of the spatial distribution of  
7 3D microwells of various diameters in a hydroxy-PAAm hydrogel that was incubated with  
8 green fluorescent microbeads. The scale bar is 500  $\mu\text{m}$ . (E) The microwell radius ( $xy$ ) is linearly  
9 related to the radius of the circular patterns on the photomask ( $R^2=0.9974$ ). (F) Microwell depth  
10 ( $xz$ ) as a function of the photomask feature radius with radius of 25  $\mu\text{m}$  in purple, 50  $\mu\text{m}$  in  
11 blue, 100  $\mu\text{m}$  in orange and 150  $\mu\text{m}$  in green. (G) Microwell radius as a function of the  
12 microwell depth. Typical confocal images showing top ( $xy$ ) and side ( $xz$ ;  $yz$ ) views of 3D  
13 microwells of (H)  $30 \pm 3 \mu\text{m}$ , (I)  $65 \pm 3 \mu\text{m}$  and (J)  $100 \pm 3 \mu\text{m}$  in radius covered by a confluent  
14 epithelial monolayer. Scale bars in (H-J) represent 20  $\mu\text{m}$ .

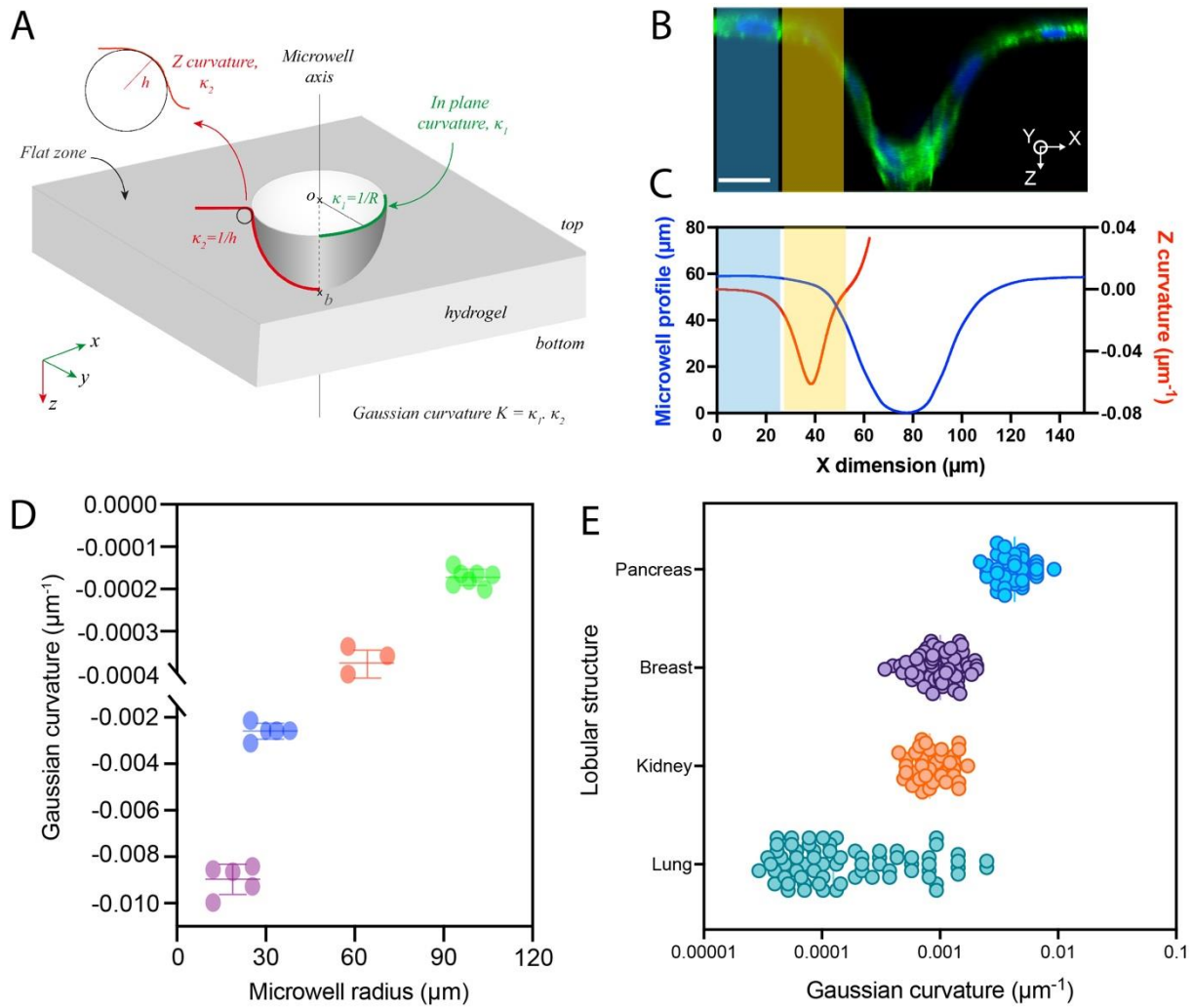


**Figure 2 – Gaussian curvatures at the entrance of 3D synthetic microwells and in human lobules.** (A) Bowl-shaped 3D microwells were characterized by a combination of an in-plane ( $xy$ , in green) curvature,  $\kappa_1$ , determined by the microwell radius,  $R$ , as  $\kappa_1=1/R$ , with an  $Z$  ( $xz$ , in red) curvature  $\kappa_2$  localized at the microwell entrance and determined as  $\kappa_2=1/h$ , with  $h$  the microwell depth. A flat hydrogel zone surrounds each 3D microwell. The Gaussian curvature  $K$  at the microwell entrance corresponds to  $K = \kappa_1 \times \kappa_2$ . (B) Representative confocal profile of a microwell of 30  $\mu\text{m}$  in radius covered with a monolayer of epithelial cells stained for actin (in green) and DNA (in blue). (C) Profile of a microwell of 30  $\mu\text{m}$  in radius (in blue) and the corresponding  $Z$  curvature (in red) calculated at each point of the microwell profile. The light blue box on (B) and (C) represents the flat zone around the microwell, while the light-yellow box delimits the Gaussian curvature zone at the microwell entrance. (D) Gaussian curvature at

the entrance of microwells with radius of 20  $\mu\text{m}$  (in purple), 30  $\mu\text{m}$  (in blue), 65  $\mu\text{m}$  (in red) and 100  $\mu\text{m}$  (in green). Each point corresponds to one replicate with  $n \geq 5$  microwells per replicate. (E) Typical Gaussian curvatures in the lobular structures of four human organs: lung (in green), kidney<sup>[23][24]</sup> (in orange), breast<sup>[25]</sup> (in purple) and pancreas<sup>[12]</sup> (in blue).

1  
2  
3  
4  
5  
6  
7  
8  
9  
10  
11  
12  
13  
14  
15  
16  
17  
18  
19  
20  
21  
22  
23  
24  
25  
26  
27  
28  
29  
30  
31  
32  
33  
34  
35  
36  
37  
38  
39  
40  
41  
42  
43  
44  
45  
46  
47  
48  
49  
50  
51  
52  
53  
54  
55  
56  
57  
58  
59  
60  
61  
62  
63  
64  
65

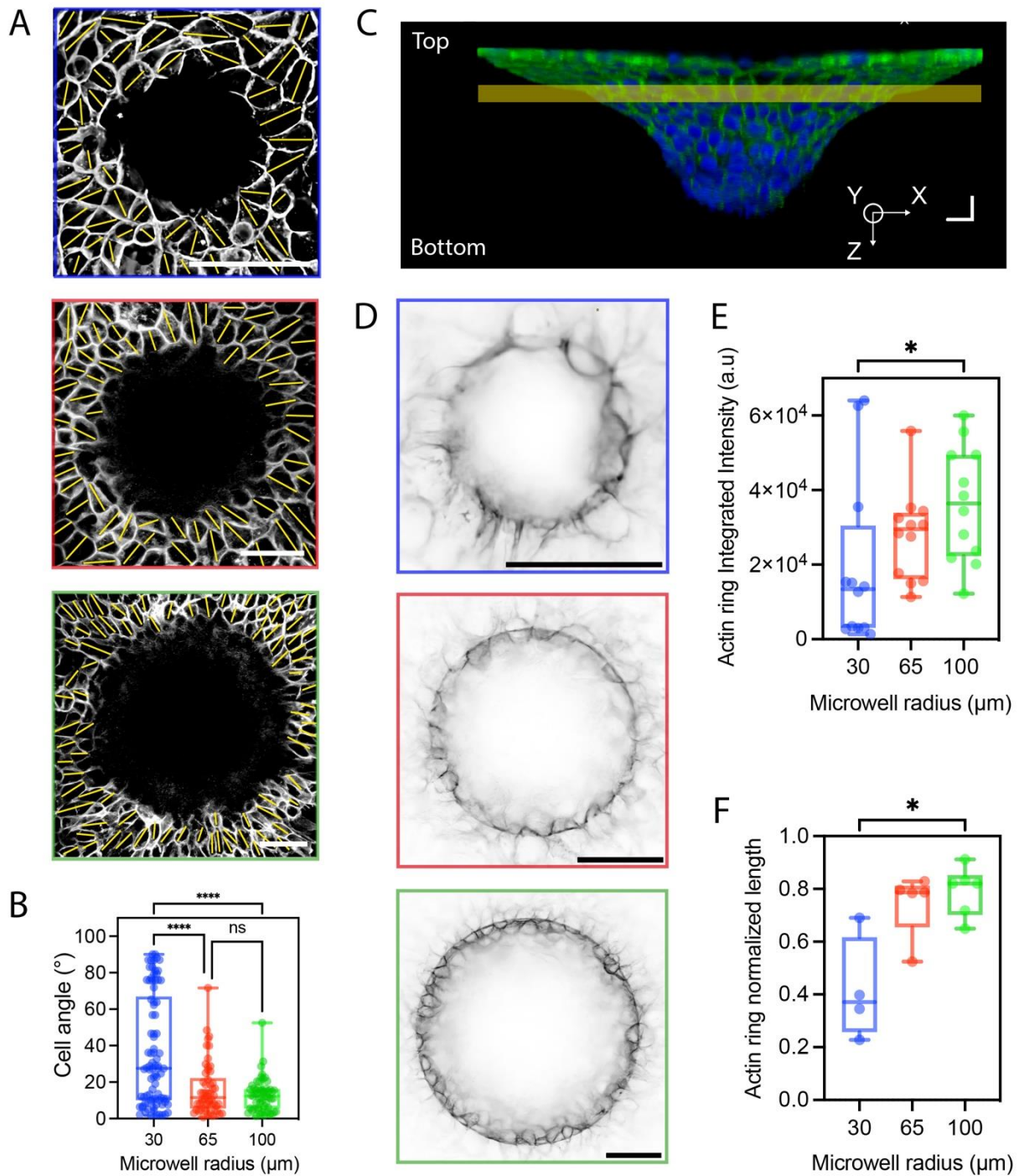


**Figure 3 – Low in-plane curvature promotes centripetal cell orientation and formation of a supracellular actin cable at the microwell edge.** (A) Top view images of E-cadherin cells were used to determine (B) cellular orientations around the edge of 30  $\mu\text{m}$  in radius (n=89, in blue), 65  $\mu\text{m}$  in radius (n=68, in red) and 100  $\mu\text{m}$  in radius (n=75, in green) microwells (n=3 for each condition). Fluorescent images were inverted, and orientations of the long cell axis

1 were depicted by yellow segments. Scale bars are 50  $\mu\text{m}$ . (C) Confocal images were acquired  
2 at focal planes corresponding with the maximal Z curvature zone (light yellow line) to  
3 characterize the organization of the actin cytoskeleton at the Z curvature zone. (D)  
4 Representative confocal images of the actin cytoskeleton at the Z curvature zone of 30  $\mu\text{m}$  (in  
5 blue), 65  $\mu\text{m}$  (in red) and 100  $\mu\text{m}$  (in green) in radius. Actin was stained with phalloidin, and  
6 images were inverted to visualize the formation of an actin ring at the microwell edge. Scale  
7 bars are 50  $\mu\text{m}$ . (E) Integrated intensity and (F) normalized length of the actin ring for microwell  
8 radii of 30  $\mu\text{m}$  (in blue), 65  $\mu\text{m}$  (in red) and 100  $\mu\text{m}$  (in green).  
9  
10  
11  
12  
13  
14  
15  
16  
17  
18  
19  
20  
21  
22  
23  
24  
25  
26  
27  
28  
29  
30  
31  
32  
33  
34  
35  
36  
37  
38  
39  
40  
41  
42  
43  
44  
45  
46  
47  
48  
49  
50  
51  
52  
53  
54  
55  
56  
57  
58  
59  
60  
61  
62  
63  
64  
65



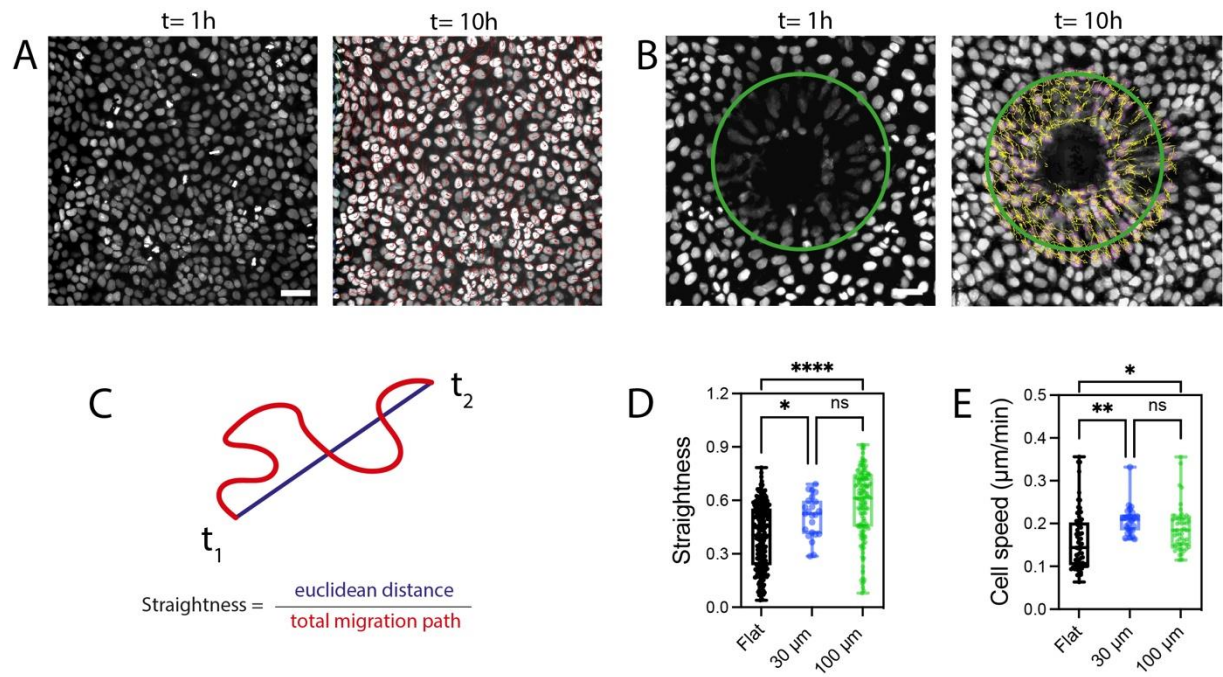


**Figure 4 – Convex curvature at the microwell entrance enhances collective migration straightness and speed.** Time-lapse sequence in confocal mode (maximum intensity projection) of the cumulative trajectories over 10 hours of individual cells within a confluent epithelial tissue on (A) a flat zone and (B) around the edge of a 3D microwell of 100 μm in radius. Scale bars represent 50 μm. The green circle delimits the zone around the microwell edge. (C) Schematic representation of the straightness parameter, defined by the ratio between the Euclidean distance and the total migration path. Cell (D) straightness and (E) speed within a confluent epithelial tissue on a flat zone (in black, n=253) and around the edge of a 3D microwell of 30 μm in radius (in blue, n=24) and 100 μm in radius (in green, n=137) with \*p < 0.05 and \*\*\*\*p < 0.0001.

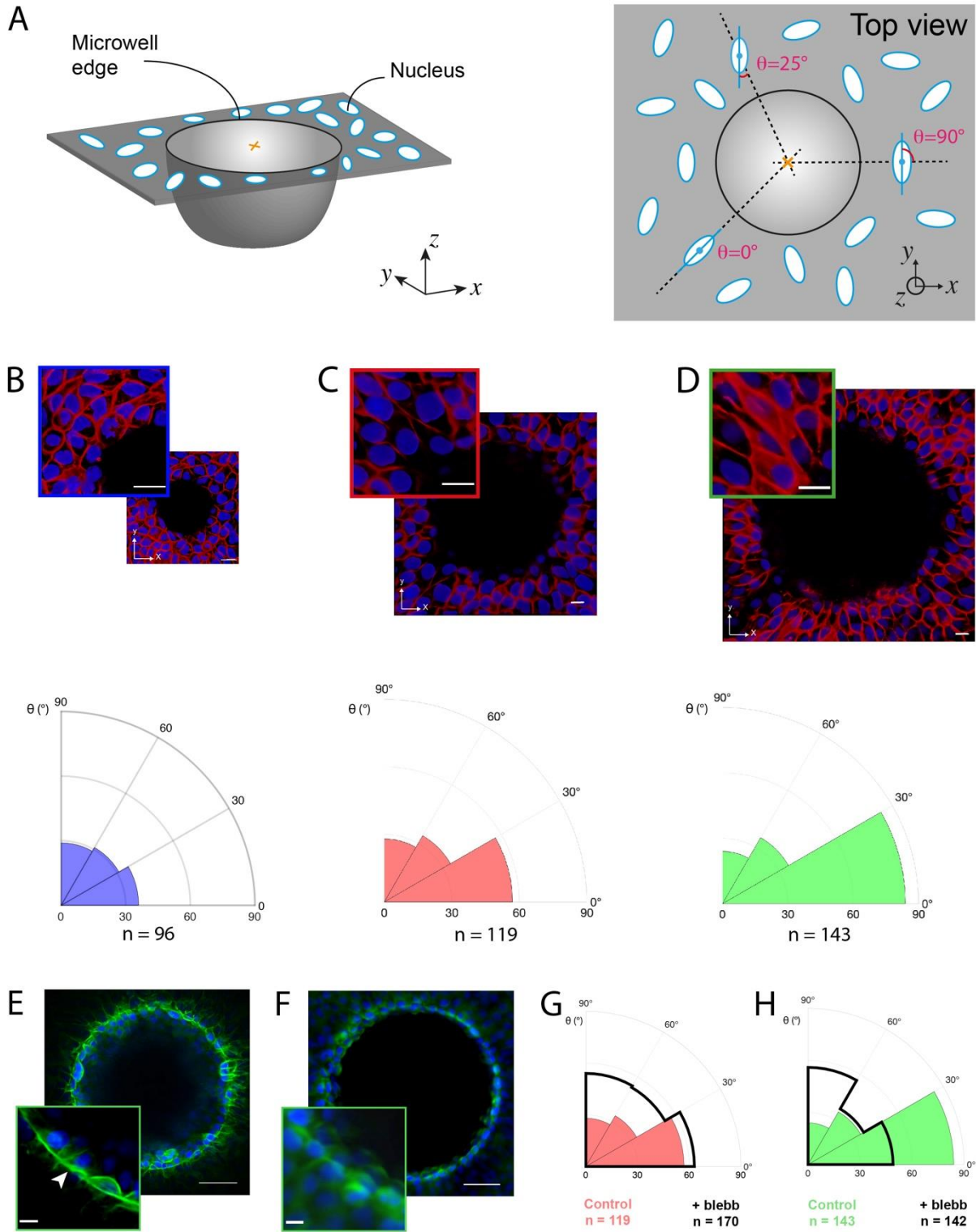


**Figure 5 – The nuclear orientation around the edge of the microwells relies on contractile actomyosin forces.** (A) Schematic representation of different scenarios of nuclear orientation around the microwell edge (black circle on the top view). The nuclear orientation was obtained by determining the angle (in red) between the nuclear long axis (blue line) and the dotted line

1 passing through the ( $xy$ ) center of the microwell (orange cross) and the center of mass of the  
2 nucleus (blue dot). Angles ranged from  $\theta=0^\circ$  and  $\theta=90^\circ$  for nuclei parallel or perpendicular  
3 respectively to the dotted line passing through the ( $xy$ ) center of the microwell and their center  
4 of mass. An intermediate situation with  $\theta = 25^\circ$  is presented. Top view ( $xy$ ) confocal images  
5 and corresponding nuclear orientations around the edge of microwells of (B) 30  $\mu\text{m}$  in radius  
6 (n=96, in blue), (C) 65  $\mu\text{m}$  in radius (n=119, in red) and (D) 100  $\mu\text{m}$  (n=143, in green) in radius.  
7 Cadherins are labeled in red and nuclei in blue. Scale bars are 20  $\mu\text{m}$ . Confocal top view ( $xy$ )  
8 images of the actin ring in microwell of 100  $\mu\text{m}$  in radius (E) before and (F) after blebbistatin  
9 treatment. Scale bars are 50  $\mu\text{m}$  and 10  $\mu\text{m}$  for the insets. Nuclear orientation for normal (plain  
10 colors) and blebbistatin-treated cells (superimposed in black) at the edge of microwells of (G)  
11 65  $\mu\text{m}$  and (H) 100  $\mu\text{m}$  in radius. Nuclear orientation for microwells of 65  $\mu\text{m}$  (n=170) and 100  
12  $\mu\text{m}$  (n=142) in radius are presented in red and green, respectively.  
13  
14  
15  
16  
17  
18  
19  
20  
21  
22  
23  
24  
25  
26  
27  
28  
29  
30  
31  
32  
33  
34  
35  
36  
37  
38  
39  
40  
41  
42  
43  
44  
45  
46  
47  
48  
49  
50  
51  
52  
53  
54  
55  
56  
57  
58  
59  
60  
61  
62  
63  
64  
65

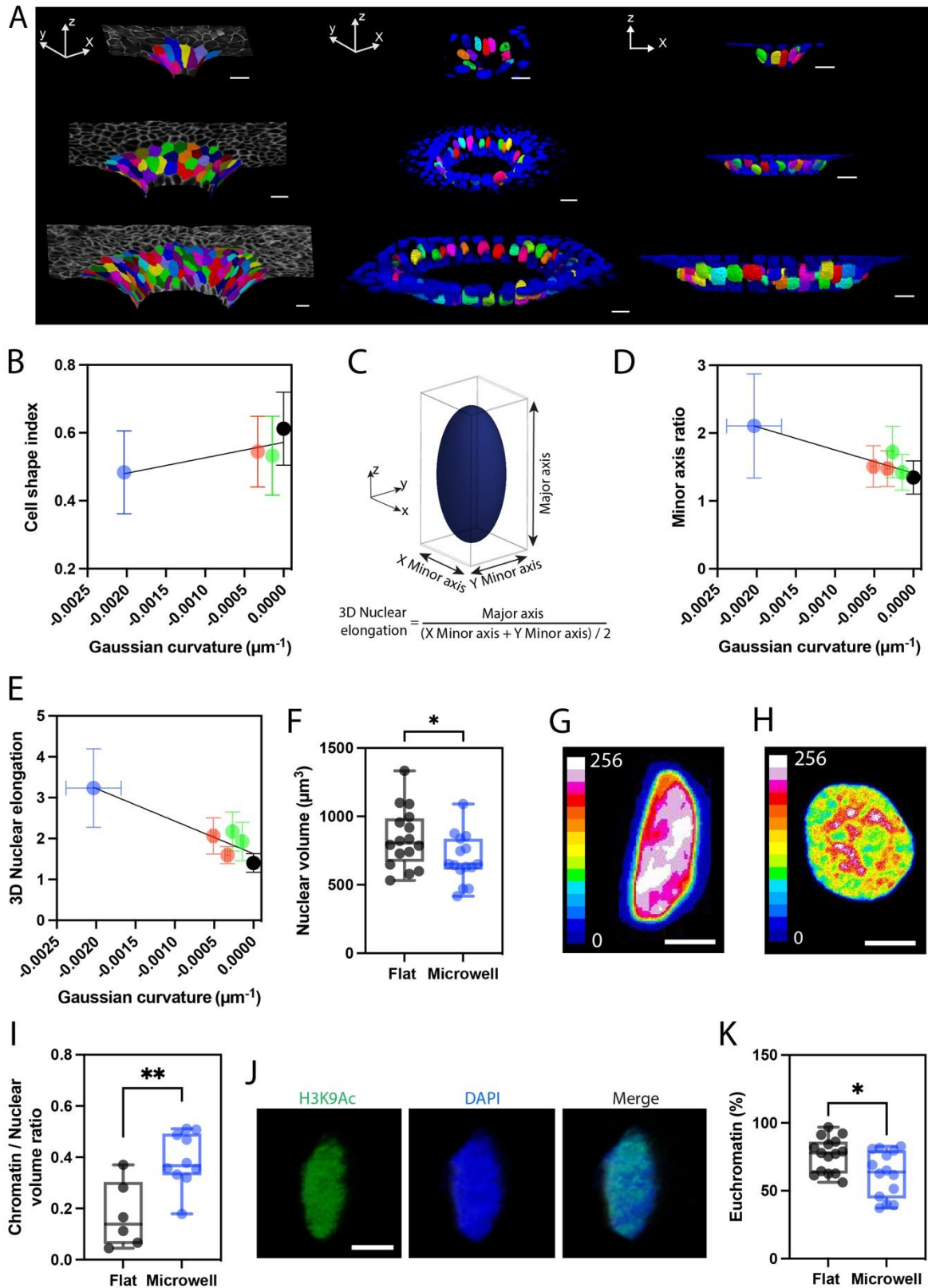
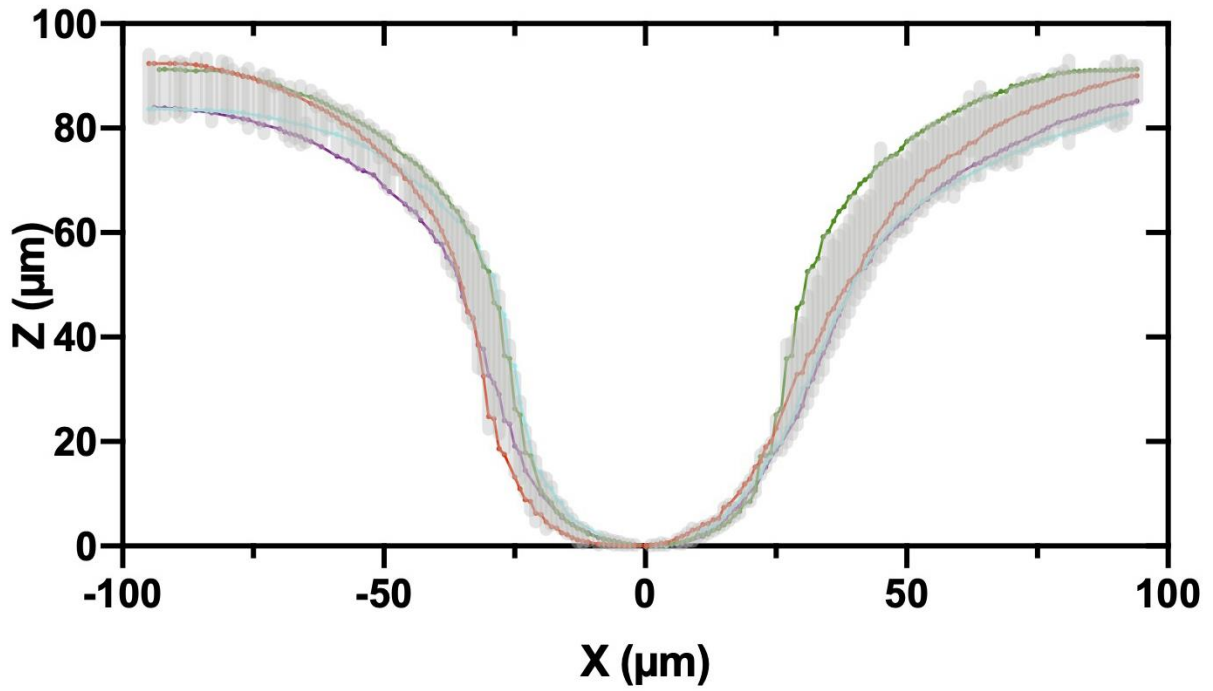


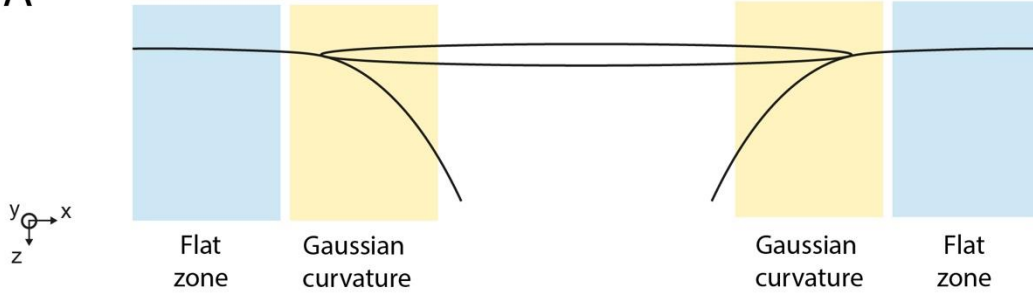
**Figure 6 – The Gaussian curvature at the microwell entrance induces a vertical nuclear elongation towards the microwell bottom.** (A) Tilted ( $xyz$ ) and side ( $xz$ ) confocal views of cells located at the maximal convex curvature zone in microwells of 30  $\mu\text{m}$  (top row), 65  $\mu\text{m}$

1 (middle row) and 100  $\mu\text{m}$  (bottom row) in radius. Individual cells and nuclei were thresholded  
2 and color-coded for better spatial representation. Scale bars are 20  $\mu\text{m}$ . (B) Mean cell shape  
3 index (CSI) as a function of the Gaussian curvature. Microwells of 30  $\mu\text{m}$  in radius are in blue  
4 (n=68), 65  $\mu\text{m}$  in radius in red (n=241), 100  $\mu\text{m}$  in radius in green (n=468), while data in black  
5 represent flat hydrogel zones (n=689). All conditions used 3 replicates. (C) Schematic  
6 representation of an elongated nucleus with the major axis oriented towards the microwell axis.  
7 (D) Minor axis ratio and (E) 3D nuclear elongations were both linearly related with the  
8 Gaussian curvature, with  $R^2=0.8413$  and  $R^2=0.8616$ , respectively. Data in black correspond to  
9 the nuclear elongation on flat zones. (F) Nuclear volume of cells located in flat (in black) and  
10 Gaussian (in blue) curvature zones. Typical images of the chromatin condensation obtained  
11 from a Z-projection for nuclei localized in (G) maximal curvature zones and (H) flat zones of  
12 a microwell of 30  $\mu\text{m}$  in radius. Intensities of DNA staining were digitized in 256 bits and color  
13 coded for each Z-stack. Highly condensed domains show higher fluorescence intensity (white  
14 zones) with respect to the less condensed ones (blue zones). (I) Chromatin to nuclear volume  
15 ratio for nuclei localized on flat (in black) and Gaussian (in blue) curvature zones. (J)  
16 Representative confocal images of an elongated nuclei in a Gaussian curvature zone stained for  
17 H3K9Ac (in green) and DAPI (in blue). (K) Percentage of euchromatin in nuclei localized on  
18 flat (in black) and Gaussian (in blue) curvature zones. \* $p < 0.05$  and \*\* $p < 0.0025$ .

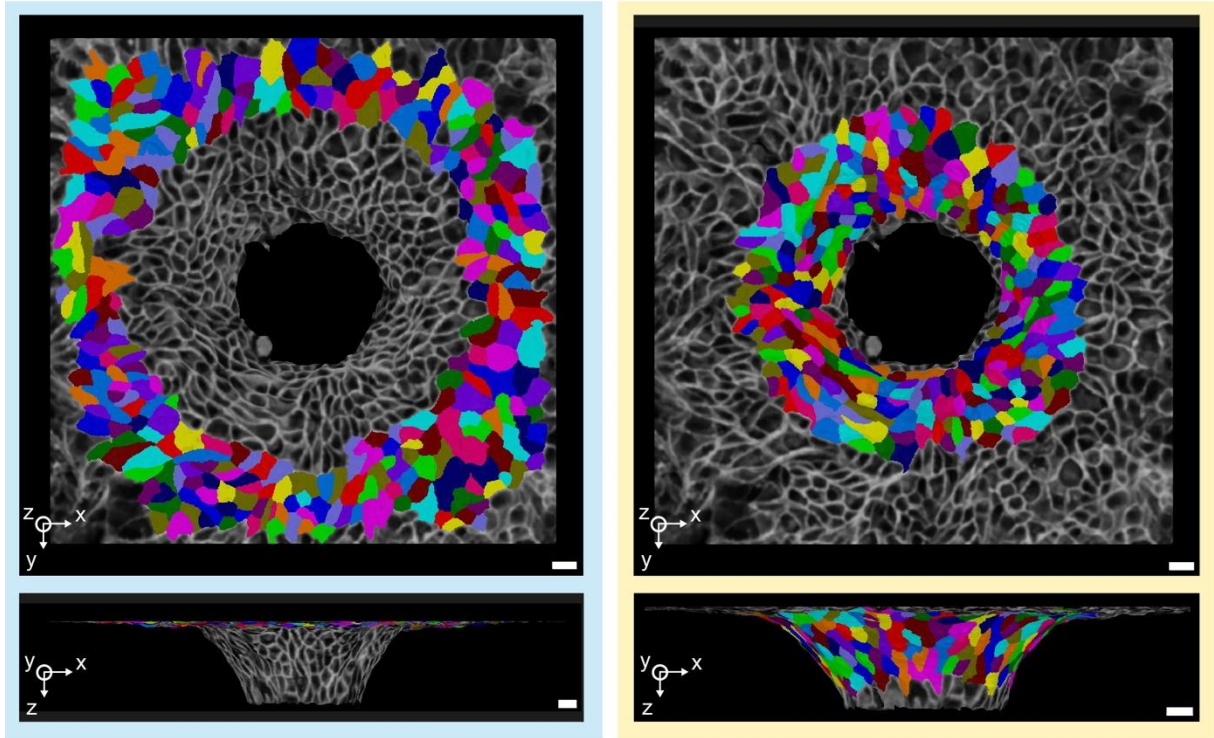


**Supplementary Figure 1 – Microwell profiles.** Superimposed ( $xz$ ) profiles of microwells of 60  $\mu\text{m}$  in radius. Each solid curve ( $n=4$  replicates) corresponds to the mean of 3 microwell profiles with S.D in dashed gray.

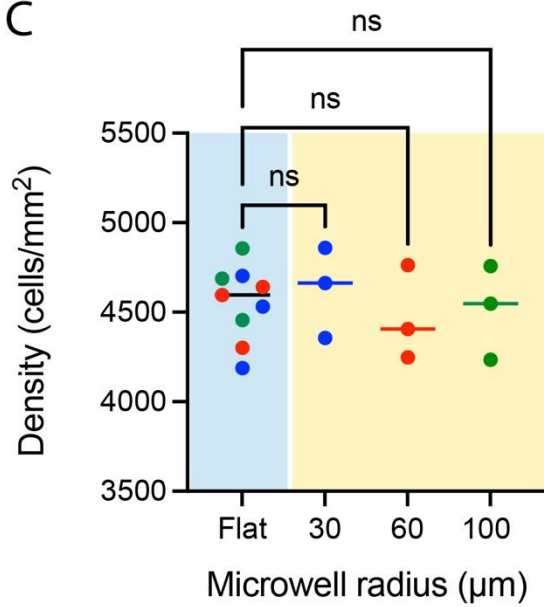
A



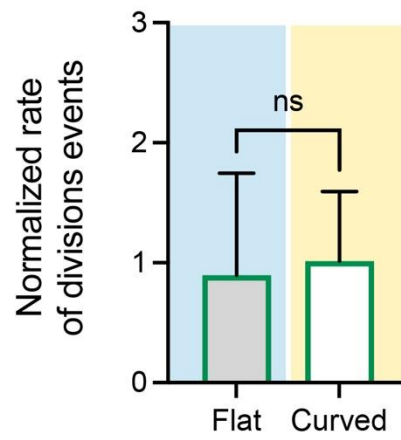
B



C



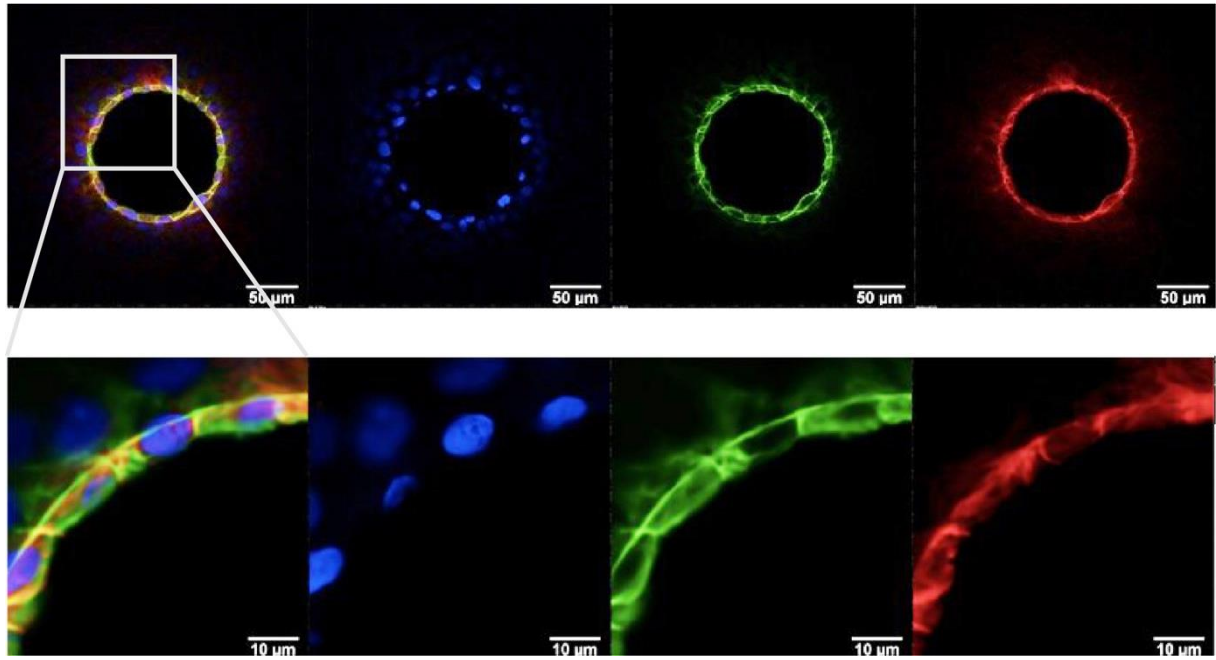
D



**Supplementary Figure 2 – Cell density and proliferation rate.** (A) Schematic representation of two distinct regions around the entrance of bowl-shaped 3D microwells, progressing from the outer edge to the inner regions. The first zone (in light blue) corresponds to a flat area surrounding the curved edge of the microwells, where the in-plane curvature is determined by the diameter of the well. The second region corresponds to the maximal Gaussian curvature zone (in light yellow) at the microwell entrance. (B) Individual cells located at either the flat zone (blue box on the left) or the Gaussian curvature zone (yellow box on the right) were segmented on m-cherry cadherin confocal images. Top and bottom rows show normal and side confocal views of both zones in a microwell of 100  $\mu\text{m}$  in radius, respectively. (C) Cellular density in flat (light blue box) and Gaussian curvature (yellow box) zones for microwell radius of 30  $\mu\text{m}$  (in blue), 60  $\mu\text{m}$  (in red) and 100  $\mu\text{m}$  (in green). (D) Normalized rate of division events in flat (light blue box) and Gaussian curvature (light yellow box) zones of a microwell of 100  $\mu\text{m}$  in radius. n.s. is not significant.

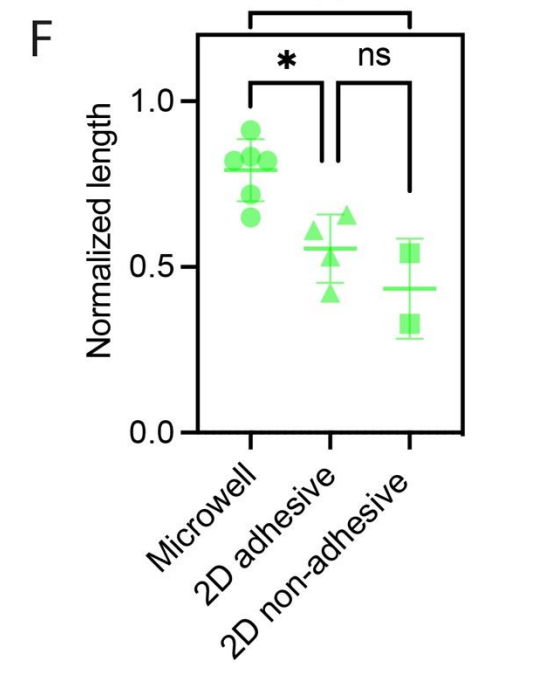
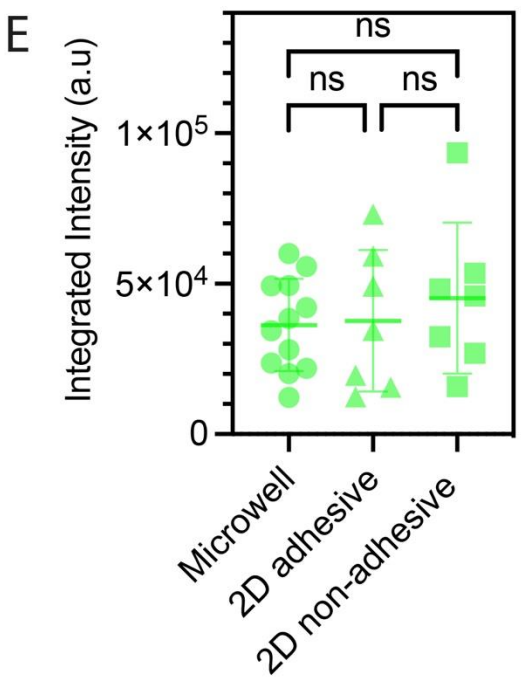
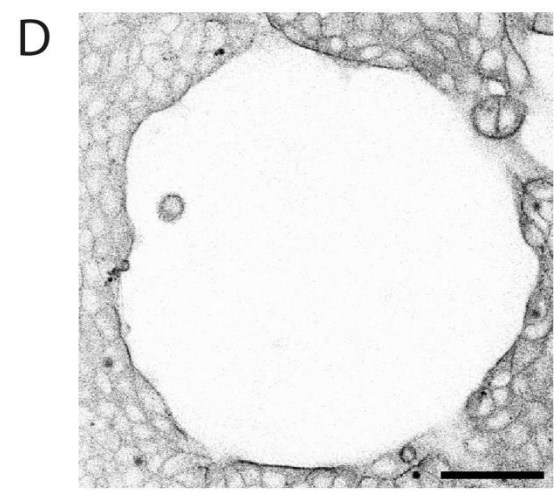
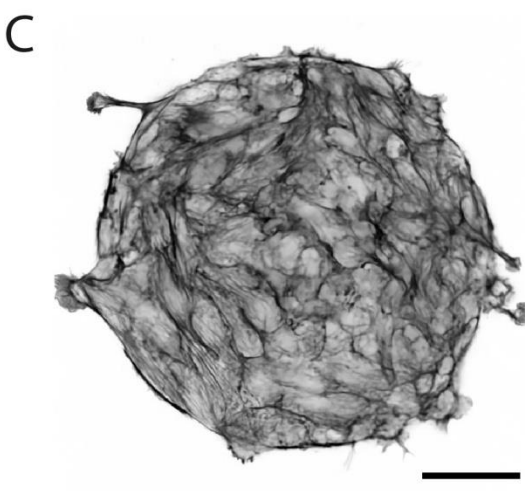
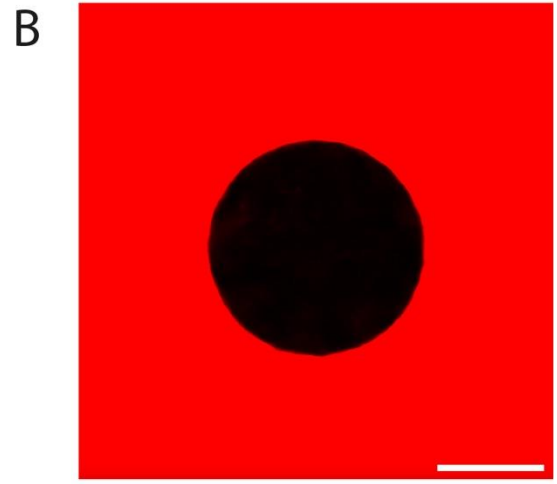
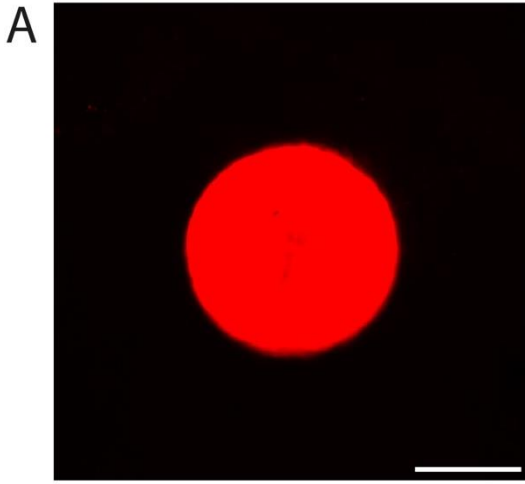
1  
2  
3  
4  
5  
6  
7  
8  
9  
10  
11  
12  
13  
14  
15  
16  
17  
18  
19  
20  
21  
22  
23  
24  
25  
26  
27  
28  
29  
30  
31  
32  
33  
34  
35  
36  
37  
38  
39  
40  
41  
42  
43  
44  
45  
46  
47  
48  
49  
50  
51  
52  
53  
54  
55  
56  
57  
58  
59  
60  
61  
62  
63  
64  
65





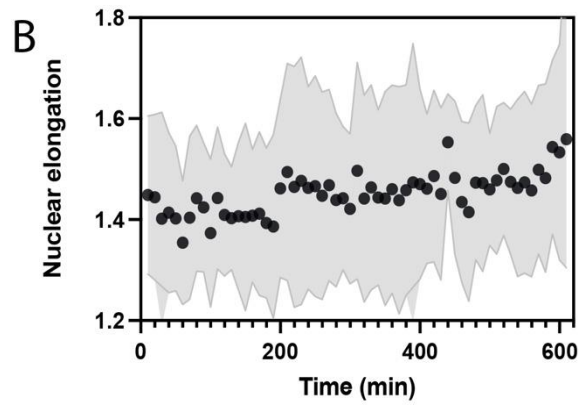
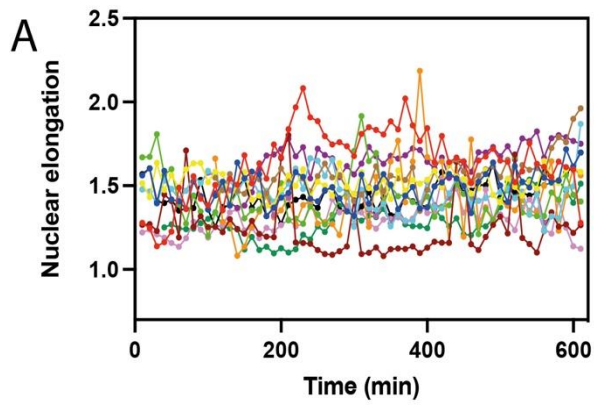
**Supplementary Figure 3 – Supracellular actin ring at the microwell entrance.** Confocal top (*xy*) view of a supracellular actin ring in a microwell of 100 μm in radius. Nuclei are stained in blue (Hoechst 33342), the actin cytoskeleton in green (AlexaFluor488 Phalloidin) and the cell-cell junctions in red (m-cherry cadherins). Scale bars are 50 μm (top) and 10 μm (bottom).

1  
2  
3  
4  
5  
6  
7  
8  
9  
10  
11  
12  
13  
14  
15  
16  
17  
18  
19  
20  
21  
22  
23  
24  
25  
26  
27  
28  
29  
30  
31  
32  
33  
34  
35  
36  
37  
38  
39  
40  
41  
42  
43  
44  
45  
46  
47  
48  
49  
50  
51  
52  
53  
54  
55  
56  
57  
58  
59  
60  
61  
62  
63  
64  
65



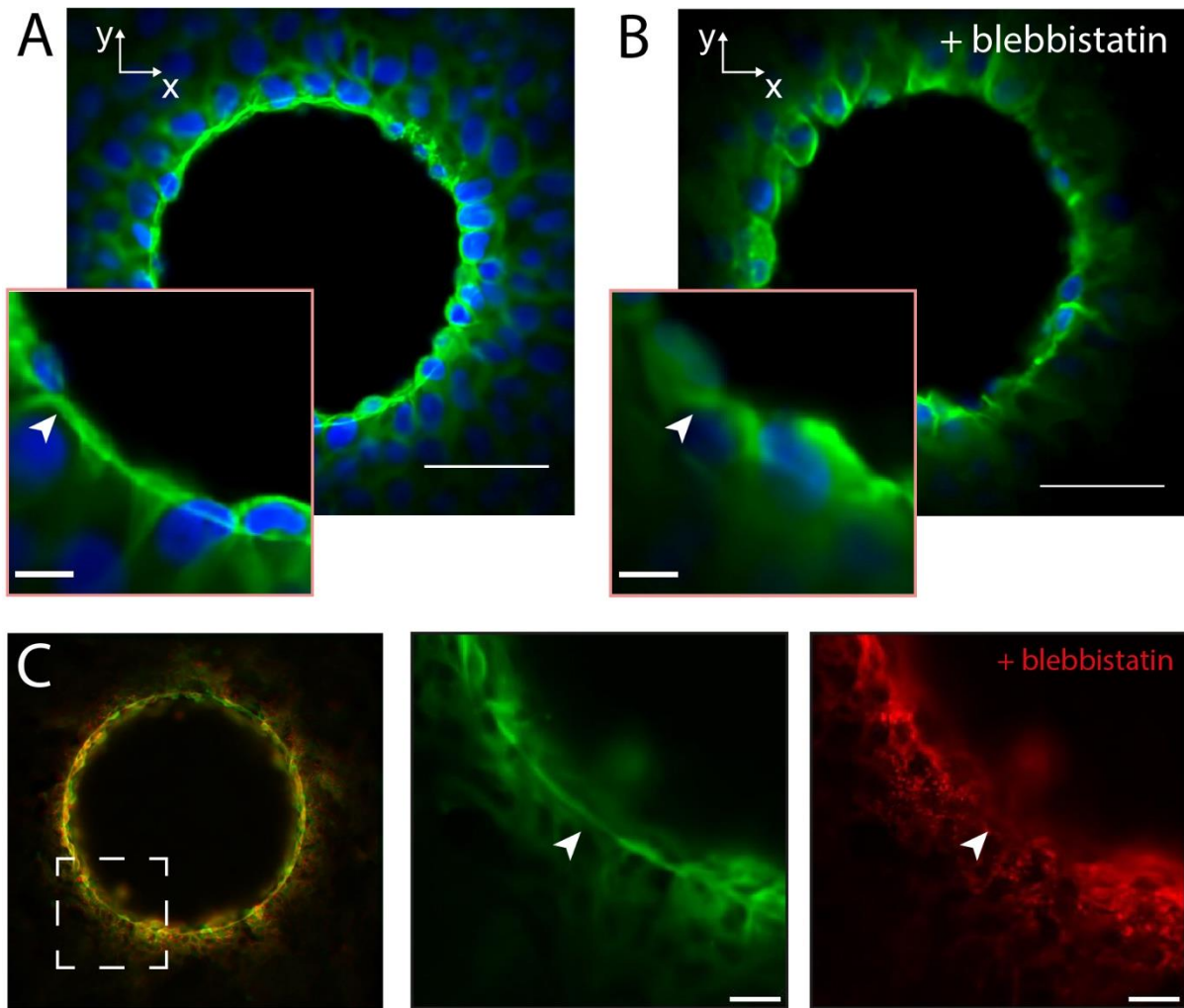
**Supplementary Figure 4 – Supracellular actin ring in 2D micropatterned epithelial monolayers.** 2D circular (A) adhesive and (B) non-adhesive fibronectin (in red) micropatterns of 100  $\mu\text{m}$  radius. The scale bars are 100  $\mu\text{m}$ . Representative image of the actin cytoskeleton of MDCK cells grown for 24 hours on 2D circular (C) adhesive and (D) non-adhesive fibronectin micropatterns. The scale bars are 50  $\mu\text{m}$ . (E) Integrated intensity and (F) normalized length of the actin ring in 3D microwell of 100  $\mu\text{m}$  in radius (circles), 2D adhesive circular patterns of 100  $\mu\text{m}$  in radius (triangles) and 2D non-adhesive circular patterns of 100  $\mu\text{m}$  in radius (squares).

1  
2  
3  
4  
5  
6  
7  
8  
9  
10  
11  
12  
13  
14  
15  
16  
17  
18  
19  
20  
21  
22  
23  
24  
25  
26  
27  
28  
29  
30  
31  
32  
33  
34  
35  
36  
37  
38  
39  
40  
41  
42  
43  
44  
45  
46  
47  
48  
49  
50  
51  
52  
53  
54  
55  
56  
57  
58  
59  
60  
61  
62  
63  
64  
65



**Supplementary Figure 5 – Dynamic nuclear deformation.** Evolution of the nuclear elongation (major to minor axis ratio) of epithelial cells (n=13) moving from the outer edge (t=0) to the inner zone (t=600 min.) of a 3D microwell of 100  $\mu\text{m}$  in radius. (A) Each color-coded curve represents one nucleus (n=11). (B) Evolution of the mean nuclear deformation with standard deviation represented in light grey. The total duration time is 10 hours.

1  
2  
3  
4  
5  
6  
7  
8  
9  
10  
11  
12  
13  
14  
15  
16  
17  
18  
19  
20  
21  
22  
23  
24  
25  
26  
27  
28  
29  
30  
31  
32  
33  
34  
35  
36  
37  
38  
39  
40  
41  
42  
43  
44  
45  
46  
47  
48  
49  
50  
51  
52  
53  
54  
55  
56  
57  
58  
59  
60  
61  
62  
63  
64  
65



**Supplementary Figure 6 – Inhibition of the actomyosin contractility.** Representative top-view confocal images of the immunostained actin ring in a microwell of 65  $\mu\text{m}$  in radius (A) before and (B) after 1 hour of blebbistatin treatment. (C) Superimposed top-view confocal images of the actin ring in a microwell of 100  $\mu\text{m}$  in radius before (in green) and after (in red) 1 hour and 30 minutes of blebbistatin treatment during time-lapse acquisition. White arrow shows the collapse of the actin cable in blebbistatin-treated cells.

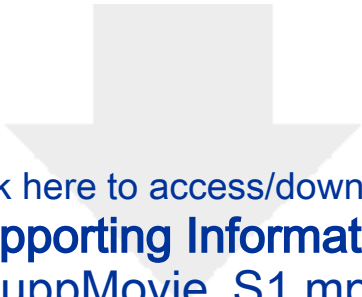
1  
2  
3  
4  
5  
6  
7  
8  
9  
10  
11  
12  
13  
14  
15  
16  
17  
18  
19  
20  
21  
22  
23  
24  
25  
26  
27  
28  
29  
30  
31  
32  
33  
34  
35  
36  
37  
38  
39  
40  
41  
42  
43  
44  
45  
46  
47  
48  
49  
50  
51  
52  
53  
54  
55  
56  
57  
58  
59  
60  
61  
62  
63  
64  
65

**Supplementary Movie S1** – 3D confocal view of a microwell of 30  $\mu\text{m}$  in radius covered by an epithelial monolayer stained for F-actin with phalloidin (in green) and DNA with Hoechst 33342 (in blue).


**Supplementary Movie S2** – 3D confocal view of a microwell of 65  $\mu\text{m}$  in radius covered by an epithelial monolayer stained for F-actin with phalloidin (in green) and DNA with Hoechst 33342 (in blue).

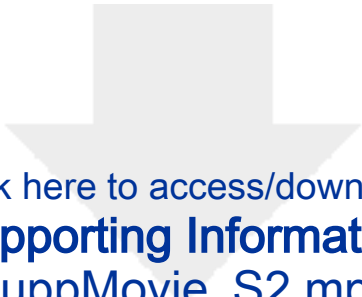
**Supplementary Movie S3** – 3D confocal view of a microwell of 100  $\mu\text{m}$  in radius covered by an epithelial monolayer stained for F-actin with phalloidin (in green) and DNA with Hoechst 33342 (in blue).

**Supplementary Movie S4** – Time-lapse movie (duration time = 10 hours) in confocal mode of the nuclear movements in an epithelial monolayer covering a 3D microwell of 100  $\mu\text{m}$  in radius. Nuclei are stained with Hoechst 33342. The scale bar is 50  $\mu\text{m}$ .

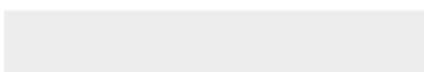
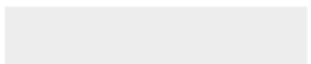


Click here to access/download  
**Supporting Information**  
SuppMovie\_S1.mp4

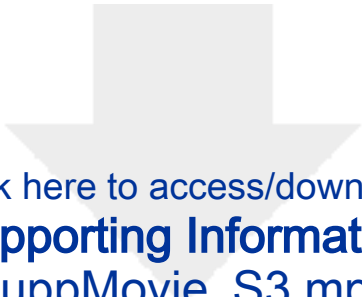





Click here to access/download  
**Supporting Information**  
SuppMovie\_S2.mp4

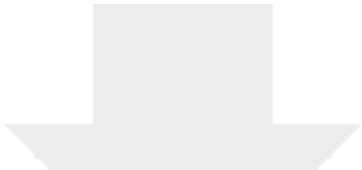




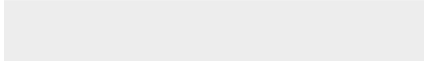
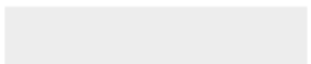


Click here to access/download  
**Supporting Information**  
SuppMovie\_S3.mp4





Click here to access/download  
**Supporting Information**  
SuppMovie\_S4.avi





Click here to access/download  
**Supporting Information**  
SI\_Microwell\_20230811.docx

